CHARACTERISTICS OF WIRE BICONICAL ANTENNAS

A Thesis Presented to

The Department of Electrical & Computer Engineering
The Faculty of Graduate Studies
The University of Manitoba

In Partial Fulfillment
of the Requirements for the Degree
Master of Science in Electrical Engineering

by

Wilson Wai Ho Cheung

Winnipeg, Manitoba, 1993

ISBN 0-315-92151-X

Canada

Name WILSON WAI HO CHEUNG

Dissertation Abstracts International is arranged by broad, general subject categories. Please select the one subject which most nearly describes the content of your dissertation. Enter the corresponding four-digit code in the spaces provided.

ENGINEERING - ELECTRONICS & ELECTRICAL 0547 U·M·I

SUBJECT TERM SUBJECT CODE

Subject Categories

THE HUMANITIES AND SOCIAL SCIENCES

COMMUNICATIONS AND THE ARTS
Architecture 0729
Art History 0377
Cinema 0900
Dance 0378
Fine Arts 0357
Information Science 0723
Journalism 0391
Library Science 0399
Mass Communications 0708
Music 0413
Speech Communication 0459
Theater 0465

EDUCATION
General 0515
Administration 0514
Adult and Continuing 0516
Agricultural 0517
Art 0273
Bilingual and Multicultural 0282
Business 0688
Community College 0275
Curriculum and Instruction 0727
Early Childhood 0518
Elementary 0524
Finance 0277
Guidance and Counseling 0519
Health 0680
Higher 0745
History of 0520
Home Economics 0278
Industrial 0521
Language and Literature 0279
Mathematics 0280
Music 0522
Philosophy of 0998
Physical 0523
Psychology 0525
Reading 0535
Religious 0527
Sciences 0714
Secondary 0533
Social Sciences 0534
Sociology of 0340
Special 0529
Teacher Training 0530
Technology 0710
Tests and Measurements 0288
Vocational 0747

LANGUAGE, LITERATURE AND LINGUISTICS
Language
- General 0679
- Ancient 0289
- Linguistics 0290
- Modern 0291

Literature
- General 0401
- Classical 0294
- Comparative 0295
- Medieval 0297
- Modern 0298
- African 0316
- American 0591
- Asian 0305
- Canadian (English) 0352
- Canadian (French) 0355
- English 0593
- Germanic 0311
- Latin American 0312
- Middle Eastern 0315
- Romance 0313
- Slavic and East European 0314

PHILOSOPHY, RELIGION AND THEOLOGY
Philosophy 0422
Religion
- General 0318
- Biblical Studies 0321
- Clergy 0319
- History of 0320
- Philosophy of 0322

Theology 0469

SOCIAL SCIENCES
American Studies 0323
Anthropology
- Archaeology 0324
- Cultural 0326
- Physical 0327

Business Administration
- General 0310
- Accounting 0272
- Banking 0770
- Management 0454
- Marketing 0338

Canadian Studies 0385
Economics
- General 0501
- Agricultural 0503
- Commerce-Business 0505
- Finance 0508
- History 0509
- Labor 0510
- Theory 0511

Folklore 0358
Geography 0366
Gerontology 0351
History
- General 0578
- Ancient 0579
- Medieval 0581
- Modern 0582
- Black 0328
- African 0331
- Asia, Australia and Oceania 0332
- Canadian 0334
- European 0335
- Latin American 0336
- Middle Eastern 0333
- United States 0337

History of Science 0585
Law 0398
Political Science
- General 0615
- International Law and Relations 0616
- Public Administration 0617

Recreation 0814
Social Work 0452
Sociology
- General 0626
- Criminology and Penology 0627
- Demography 0938
- Ethnic and Racial Studies 0631
- Individual and Family Studies 0628
- Industrial and Labor Relations 0629
- Public and Social Welfare 0630
- Social Structure and Development 0700
- Theory and Methods 0344

Transportation 0709
Urban and Regional Planning 0999
Women's Studies 0453

THE SCIENCES AND ENGINEERING

BIOLOGICAL SCIENCES
Agriculture
- General 0473
- Agronomy 0285
- Animal Culture and Nutrition 0475
- Animal Pathology 0476
- Food Science and Technology 0359
- Forestry and Wildlife 0478
- Plant Culture 0479
- Plant Pathology 0480
- Plant Physiology 0817
- Range Management 0777
- Wood Technology 0746

Biology
- General 0306
- Anatomy 0287
- Biostatistics 0308
- Botany 0309
- Cell 0379
- Ecology 0329
- Entomology 0353
- Genetics 0369
- Limnology 0793
- Microbiology 0410
- Molecular 0307
- Neuroscience 0317
- Oceanography 0416
- Physiology 0433
- Radiation 0821
- Veterinary Science 0778
- Zoology 0472

Biophysics
- General 0786
- Medical 0760

EARTH SCIENCES
Biogeochemistry 0425
Geochemistry 0996
Geodesy 0370
Geology 0372
Geophysics 0373
Hydrology 0388
Mineralogy 0411
Paleobotany 0345
Paleoecology 0426
Paleontology 0418
Paleozoology 0985
Palynology 0427
Physical Geography 0368
Physical Oceanography 0415

HEALTH AND ENVIRONMENTAL SCIENCES
Environmental Sciences 0768
Health Sciences
- General 0566
- Audiology 0300
- Chemotherapy 0992
- Dentistry 0567
- Education 0350
- Hospital Management 0769
- Human Development 0758
- Immunology 0982
- Medicine and Surgery 0564
- Mental Health 0347
- Nursing 0569
- Nutrition 0570
- Obstetrics and Gynecology 0380
- Occupational Health and Therapy 0354
- Ophthalmology 0381
- Pathology 0571
- Pharmacology 0419
- Pharmacy 0572
- Physical Therapy 0382
- Public Health 0573
- Radiology 0574
- Recreation 0575
- Speech Pathology 0460
- Toxicology 0383

Home Economics 0386

PHYSICAL SCIENCES
Pure Sciences
Chemistry
- General 0485
- Agricultural 0749
- Analytical 0486
- Biochemistry 0487
- Inorganic 0488
- Nuclear 0738
- Organic 0490
- Pharmaceutical 0491
- Physical 0494
- Polymer 0495
- Radiation 0754

Mathematics 0405
Physics
- General 0605
- Acoustics 0986
- Astronomy and Astrophysics 0606
- Atmospheric Science 0608
- Atomic 0748
- Electronics and Electricity 0607
- Elementary Particles and High Energy 0798
- Fluid and Plasma 0759
- Molecular 0609
- Nuclear 0610
- Optics 0752
- Radiation 0756
- Solid State 0611

Statistics 0463

Applied Sciences
Applied Mechanics 0346
Computer Science 0984
Engineering
- General 0537
- Aerospace 0538
- Agricultural 0539
- Automotive 0540
- Biomedical 0541
- Chemical 0542
- Civil 0543
- Electronics and Electrical 0544
- Heat and Thermodynamics 0348
- Hydraulic 0545
- Industrial 0546
- Marine 0547
- Materials Science 0794
- Mechanical 0548
- Metallurgy 0743
- Mining 0551
- Nuclear 0552
- Packaging 0549
- Petroleum 0765
- Sanitary and Municipal 0554
- System Science 0790

Geotechnology 0428
Operations Research 0796
Plastics Technology 0795
Textile Technology 0994

PSYCHOLOGY
General 0621
Behavioral 0384
Clinical 0622
Developmental 0620
Experimental 0623
Industrial 0624
Personality 0625
Physiological 0989
Psychobiology 0349
Psychometrics 0632
Social 0451

Nom _____

Dissertation Abstracts International est organisé en catégories de sujets. Veuillez s.v.p. choisir le sujet qui décrit le mieux votre thèse et inscrivez le code numérique approprié dans l'espace réservé ci-dessous.

_____ ☐☐☐ U·M·I

SUJET — CODE DE SUJET

Catégories par sujets

HUMANITÉS ET SCIENCES SOCIALES

COMMUNICATIONS ET LES ARTS
Architecture 0729
Beaux-arts 0357
Bibliothéconomie 0399
Cinéma 0900
Communication verbale 0459
Communications 0708
Danse 0378
Histoire de l'art 0377
Journalisme 0391
Musique 0413
Sciences de l'information 0723
Théâtre 0465

ÉDUCATION
Généralités 515
Administration 0514
Art 0273
Collèges communautaires 0275
Commerce 0688
Économie domestique 0278
Éducation permanente 0516
Éducation préscolaire 0518
Éducation sanitaire 0680
Enseignement agricole 0517
Enseignement bilingue et multiculturel 0282
Enseignement industriel 0521
Enseignement primaire. 0524
Enseignement professionnel 0747
Enseignement religieux 0527
Enseignement secondaire 0533
Enseignement spécial 0529
Enseignement supérieur 0745
Évaluation 0288
Finances 0277
Formation des enseignants 0530
Histoire de l'éducation 0520
Langues et littérature 0279
Lecture 0535
Mathématiques 0280
Musique 0522
Orientation et consultation 0519
Philosophie de l'éducation 0998
Physique 0523
Programmes d'études et enseignement 0727
Psychologie 0525
Sciences 0714
Sciences sociales 0534
Sociologie de l'éducation 0340
Technologie 0710

LANGUE, LITTÉRATURE ET LINGUISTIQUE
Langues
- Généralités 0679
- Anciennes 0289
- Linguistique 0290
- Modernes 0291

Littérature
- Généralités 0401
- Anciennes 0294
- Comparée 0295
- Médiévale 0297
- Moderne 0298
- Africaine 0316
- Américaine 0591
- Anglaise 0593
- Asiatique 0305
- Canadienne (Anglaise) 0352
- Canadienne (Française) 0355
- Germanique 0311
- Latino-américaine 0312
- Moyen-orientale 0315
- Romane 0313
- Slave et est-européenne 0314

PHILOSOPHIE, RELIGION ET THÉOLOGIE
Philosophie 0422
Religion
- Généralités 0318
- Clergé 0319
- Études bibliques 0321
- Histoire des religions 0320
- Philosophie de la religion 0322

Théologie 0469

SCIENCES SOCIALES
Anthropologie
- Archéologie 0324
- Culturelle 0326
- Physique 0327

Droit 0398
Économie
- Généralités 0501
- Commerce-Affaires 0505
- Économie agricole 0503
- Économie du travail 0510
- Finances 0508
- Histoire 0509
- Théorie 0511

Études américaines 0323
Études canadiennes 0385
Études féministes 0453
Folklore 0358
Géographie 0366
Gérontologie 0351
Gestion des affaires
- Généralités 0310
- Administration 0454
- Banques 0770
- Comptabilité 0272
- Marketing 0338

Histoire
- Histoire générale 0578
- Ancienne 0579
- Médiévale 0581
- Moderne 0582
- Histoire des noirs 0328
- Africaine 0331
- Canadienne 0334
- États-Unis 0337
- Européenne 0335
- Moyen-orientale 0333
- Latino-américaine 0336
- Asie, Australie et Océanie 0332

Histoire des sciences 0585
Loisirs 0814
Planification urbaine et régionale 0999
Science politique
- Généralités 0615
- Administration publique 0617
- Droit et relations internationales 0616

Sociologie
- Généralités 0626
- Aide et bien-être social 0630
- Criminologie et établissements pénitentiaires 0627
- Démographie 0938
- Études de l' individu et de la famille 0628
- Études des relations interethniques et des relations raciales 0631
- Structure et développement social 0700
- Théorie et méthodes. 0344
- Travail et relations industrielles 0629

Transports 0709
Travail social 0452

SCIENCES ET INGÉNIERIE

SCIENCES BIOLOGIQUES
Agriculture
- Généralités 0473
- Agronomie. 0285
- Alimentation et technologie alimentaire 0359
- Culture 0479
- Élevage et alimentation 0475
- Exploitation des pâturages 0777
- Pathologie animale 0476
- Pathologie végétale 0480
- Physiologie végétale 0817
- Sylviculture et faune 0478
- Technologie du bois 0746

Biologie
- Généralités 0306
- Anatomie 0287
- Biologie (Statistiques) 0308
- Biologie moléculaire 0307
- Botanique 0309
- Cellule 0379
- Écologie 0329
- Entomologie 0353
- Génétique 0369
- Limnologie 0793
- Microbiologie 0410
- Neurologie 0317
- Océanographie 0416
- Physiologie 0433
- Radiation 0821
- Science vétérinaire 0778
- Zoologie 0472

Biophysique
- Généralités 0786
- Medicale 0760

SCIENCES DE LA TERRE
Biogéochimie 0425
Géochimie 0996
Géodésie 0370
Géographie physique 0368
Géologie 0372
Géophysique 0373
Hydrologie 0388
Minéralogie 0411
Océanographie physique 0415
Paléobotanique 0345
Paléoécologie 0426
Paléontologie 0418
Paléozoologie 0985
Palynologie 0427

SCIENCES DE LA SANTÉ ET DE L'ENVIRONNEMENT
Économie domestique 0386
Sciences de l'environnement 0768
Sciences de la santé
- Généralités 0566
- Administration des hôpitaux 0769
- Alimentation et nutrition 0570
- Audiologie 0300
- Chimiothérapie 0992
- Dentisterie 0567
- Développement humain 0758
- Enseignement 0350
- Immunologie 0982
- Loisirs 0575
- Médecine du travail et thérapie 0354
- Médecine et chirurgie 0564
- Obstétrique et gynécologie 0380
- Ophtalmologie 0381
- Orthophonie 0460
- Pathologie 0571
- Pharmacie 0572
- Pharmacologie 0419
- Physiothérapie 0382
- Radiologie 0574
- Santé mentale 0347
- Santé publique 0573
- Soins infirmiers 0569
- Toxicologie 0383

SCIENCES PHYSIQUES
Sciences Pures
Chimie
- Généralités 0485
- Biochimie 487
- Chimie agricole 0749
- Chimie analytique 0486
- Chimie minérale 0488
- Chimie nucléaire 0738
- Chimie organique 0490
- Chimie pharmaceutique 0491
- Physique 0494
- PolymÈres 0495
- Radiation 0754

Mathématiques 0405
Physique
- Généralités 0605
- Acoustique 0986
- Astronomie et astrophysique 0606
- Électronique et électricité 0607
- Fluides et plasma 0759
- Météorologie 0608
- Optique 0752
- Particules (Physique nucléaire) 0798
- Physique atomique 0748
- Physique de l'état solide 0611
- Physique moléculaire 0609
- Physique nucléaire 0610
- Radiation 0756

Statistiques 0463

Sciences Appliqués Et Technologie
Informatique 0984
Ingénierie
- Généralités 0537
- Agricole 0539
- Automobile 0540
- Biomédicale 0541
- Chaleur et thermodynamique 0348
- Conditionnement (Emballage) 0549
- Génie aérospatial 0538
- Génie chimique 0542
- Génie civil 0543
- Génie électronique et électrique 0544
- Génie industriel 0546
- Génie mécanique 0548
- Génie nucléaire 0552
- Ingénierie des systèmes 0790
- Mécanique navale 0547
- Métallurgie 0743
- Science des matériaux 0794
- Technique du pétrole 0765
- Technique minière 0551
- Techniques sanitaires et municipales 0554
- Technologie hydraulique 0545

Mécanique appliquée 0346
Géotechnologie 0428
Matières plastiques (Technologie) 0795
Recherche opérationnelle 0796
Textiles et tissus (Technologie) 0794

PSYCHOLOGIE
Généralités 0621
Personnalité 0625
Psychobiologie 0349
Psychologie clinique 0622
Psychologie du comportement 0384
Psychologie du développement 0620
Psychologie expérimentale 0623
Psychologie industrielle 0624
Psychologie physiologique 0989
Psychologie sociale 0451
Psychométrie 0632

CHARACTERISTICS OF WIRE BICONICAL ANTENNAS

BY

WILSON WAI HO CHEUNG

A Thesis submitted to the Faculty of Graduate Studies of the University of Manitoba in partial fulfillment of the requirements of the degree of

MASTER OF SCIENCE

ABSTRACT

The performance and optimization of wire biconical antennas at low frequencies is examined using the NEC2. A planar and a body-of-revolution model of the biconical antenna is proposed and the validity of the models is established by making a comparison between the numerically and experimentally obtained results. The antenna factor of the wire biconical antennas in the study are used to evaluate their bandwidth performances. For various flare and hat angles, the characteristics of planar and body-of-revolution wire biconical antennas are obtained. Different optimization schemes for the planar wire biconical antennas are also investigated. The use of sleeve on the planar biconical antennas proves to be most useful in the optimization of the antenna factor bandwidth.

ACKNOWLEDGEMENTS

The author is indebted to his advisor Prof. L. Shafai for his supervision and enlightening discussions of the subject. The assistance of Dr. Y. Lin and other colleagues during the course of this dissertation is appreciated. Financial assistance provided by the Department of Electrical Engineering at the University of Manitoba is gratefully acknowledged.

CONTENTS

LIST OF FIGURES

LIST OF TABLE

CHAPTER I

INTRODUCTION

For many years, biconical antennas have been used in the VHF to UHF frequencies because of their broadband characteristics. Classically, the analysis of biconical structures has been centered around the biconical transmission line which is formed by placing two cones of infinite extend together. The biconical antenna would then be a finite biconical transmission line with spherical endcaps. However, for most frequencies of operation, this solid or shell biconical antenna is so massive that it is sometimes impractical. In order to reduce the massiness of the biconical antenna and yet retain as much of its desired electrical features as possible, the wire model of the biconical antenna is developed.

One of the earliest studies on wire biconical antennas was done by Prewitt et al [1]. The study addressed the need for a general solution for the planar wire model of the finite biconical antenna, which was referred to as the "Bow-Tie" antenna. In the study, the derivation of a set of equations necessary for the solution of the currents on the bowtie antenna was presented. The set of equation consists of two coupled integral equations derived from the magnetic vector potential and the boundary conditions on the surface of the wire. This set of Hallen-type coupled integral equations was then used to solve for the unknown currents using the method of moments. The technique was used to calculate the input impedance of a half-bowtie antenna with cone angle of 30° mounted over a

ground plane. A comparison between the computed and the measured results confirmed that the integral equation technique could be used to characterize the input impedance of wire biconical antennas and hence for the design of such structures. Subsequently, by using the same method, Smith and Butler [2] reported on the characteristics of planar wire biconical antennas with an upper conical angle of 180° and various lower conical, or flare angles. The study was more extensive in that not only the input impedance, but also the far electric field, of the wire structures were calculated. Unfortunately, their study revealed that while the planar wire model did provide a desirable alternative for the massive solid structures, it did not exhibit broadband impedance characteristics similar to those of the solid biconical antenna for the same conical angles. In addition, the resistance and reactance of the planar wire model fluctuated more for a given conical angle than for the very similar sheet triangular antenna investigated by Brown and Woodward [3]. They thus concluded that the planar wire biconical antenna is quite narrowband compared to the ideal surface of revolution structure and the triangle antenna.

The idea of using the wire construction technique for the fabrication of low-mass body-of-revolution structures was also examined by Smith and Butler. Multiple planar wire biconical antennas were employed to simulate the conical, body-of-revolution antenna. In the study, identical planar bowtie antennas were intersected with equal angular spacing. As the number of planar bowtie antennas increased, the radiating surface approached that of a solid biconical dipole with flat endcaps. Consequently, the characteristics of such a wire-segmented structure should approximate those of the equivalent body-of-revolution structure. The

input impedance of such a wire conical unipole antenna was computed as a function of the number of bowtie elements and the results indicated that as the number of planar elements employed was equal to or greater than eight, the low-mass structure could be used in confidence to replace the solid structure. Based on this idea, a study on the body-of-revolution model of the wire biconical antennas used for EMC measurements at low frequencies was conducted by Austin and Fourie [4]. The study examined the effects of the orientation or height of wire biconical antennas above the ground used in measurements of radiated emission from equipment under test (EUT), for frequencies from 20 to 300 MHz nominally. In the study, the problem of calculating the characteristics of wire biconical antennas was tackled by the Numerical Electromagnetics Code (NEC2 [5]). A fairly extensive validation exercise was conducted from which a suitable NEC2 model of the wire biconical structure was derived. From the results obtained from NEC2, Austin and Fourie calculated the antenna factor (AF) of a commercial antenna EMCO model 3108 biconical antenna under various orientation with respect to the ground. The good agreement existing between their computed results and Smith and Butler's [2] measured values demonstrated the usefulness of NEC2 in treating wire biconical problems.

This work investigates and attempts to optimize the performance of wire biconical antennas using NEC2. In chapter two, the theory behind the solution of the current distribution on a wire antenna as used by NEC2 is presented. The formulation of the electric field integral equation (EFIE) from the magnetic potential equation and boundary conditions on the wire surface is given. The general methodology behind the method of moments

as a numerical evaluation technique will also be discussed. Since the AF's of the antennas in this study are used to evaluated their performances, the calculation of the AF as a function of power gain and mismatch loss is presented in section 2.2.3. The input impedances and radiation patterns obtained from NEC2 for various wire biconical models are then compared to existing data for validation purposes.

Chapter III of the thesis evaluates the performance of wire biconical antennas in terms of their input impedances, power gains, mismatch losses, and AF's. The effect of flare angle and hat angle variation on antenna performances will be examined. The planar wire biconical antennas will first be discussed in section 3.2. The discussion will then be followed by the analysis of the body-of-revolution model in section 3.3. The antenna with corner reflector system is also studied using NEC2 and the results are presented in section 3.4. Unless otherwise stated, all the antennas in this chapter has a half length of A=250 mm and wire diameter of 1 mm.

Chapter IV deals mainly with the optimization of the wire biconical antennas. Preliminary optimization methods include the addition of a cross-like wire structure to the planar model, and the modification of the biconical antenna's shape. The adaptation of a pair of sleeve like elements on the sides of a antenna proves to be most effective in the optimization of the antenna's broadband characteristics and is discussed in section 4.4. Finally, a general conclusion is given in Chapter V.

CHAPTER II

ANALYSIS OF WIRE BICONICAL ANTENNAS

2.1 INTRODUCTION

Due to its skeletal configuration, the analysis of a typical wire biconical antenna is best tackled by the method of moments. Although one can go through the painstaking process of developing a computer program to obtain information that characterizes the frequency response of a wire biconical antenna, the utilization of a well established software is almost always preferred. The Numerical Electromagnetics Code (NEC2) is, therefore, used for the analysis of wire biconical antennas in this study. The NEC2 is a user-oriented computer code which builds around the numerical solution of integral equations for the current induced on a structure by sources or incident fields. The code used an electric-field integral equation (EFIE) to model the electromagnetic response of a wire structure. A form of the method of moments is then used to acquire the numerical solution of the integral equations.

The main purpose of this chapter is to present the basic principles associated with the analysis of wire biconical antenna. Section 2.2.1 and 2.2.2 are devoted to the theory and solution method behind the NEC2. In section 2.2.1, the formulation of the EFIE used in the NEC2 will be outlined. The numerical solution of the EFIE is then discussed in section

2.2.2. In section 2.2.3, the expression for a widely used antenna parameter, called the antenna factor (AF), will be developed. Before proceeding to the analysis of wire biconical antennas, a validation exercise is necessary. This is done in section 2.3 where the computed results from the NEC2 are compared with existent data.

2.2 BACKGROUND THEORY

2.2.1 Integral Equation Formulation

The derivation of the electrical-field integral equation (EFIE) used for modeling thin-wire structures of small or vanishing conductor volume in NEC2 is outlined in this section. A rigorous derivation of the equations is given by Poggio and Miller [6].

Let $(\mathbf{E},\mathbf{H})$ represent the field generated by a harmonic electric current in free space (μ_o,ε_o). Such a field will satisfy Maxwell's equations

$$\nabla \times \mathbf{E} = - j\omega\mu_o\mathbf{H} \tag{2.1}$$

$$\nabla \times \mathbf{H} = \mathbf{J} + j\omega\varepsilon_o\mathbf{E} \tag{2.2}$$

where $\mathbf{J}$ is the harmonic source current density. The wave equation to solve with $k = \omega\sqrt{\mu_o\varepsilon_o}$ is hence

$$\nabla \times \nabla \times \mathbf{E} - k^2\mathbf{E} = -j\omega\mu_o\mathbf{J} \tag{2.3}$$

Equation (2.3) can be solved in terms of the magnetic vector potential $\mathbf{A}$ and the solution is given by

$$\mathbf{E} = j\omega\left[1 + \frac{1}{k^2}\nabla\nabla\cdot\right]\mathbf{A} \tag{2.4}$$

with

$$\mathbf{A}(\mathbf{R}) = \mu_o \int_v G_o(\mathbf{R}|\mathbf{R}')\, \mathbf{J}(\mathbf{R}')\, dV \tag{2.5}$$

where the free-space Green's function $G_o(\mathbf{R}|\mathbf{R}')$ pertaining to a three-dimensional scalar wave equation is given by

$$G_o(\mathbf{R}|\mathbf{R}') = \frac{e^{jk\,|\mathbf{R}-\mathbf{R}'|}}{4\pi\,|\mathbf{R}-\mathbf{R}'|}, \quad |\mathbf{R}-\mathbf{R}'| = \sqrt{(x-x')^2 + (y-y')^2 + (z-z')^2} \tag{2.6}$$

The notation $\mathbf{R}$ denotes the position vector of a field point or that of an observer, while $\mathbf{R}'$ denotes the position vector of a source point.

It is obvious that the electric field $\mathbf{E}$ depends upon the distribution of the source current. Consider an infinitesimal source located at $\mathbf{R}'$ with a current moment of $1/j\omega\mu_o$ pointed in the $\hat{x}$ direction. The current density can then be written as [7]

$$\mathbf{J}(\mathbf{R}') = \frac{1}{j\omega\mu_o}\,\delta(\mathbf{R}-\mathbf{R}')\,\hat{x} \tag{2.7}$$

and

$$\int_v \mathbf{J}(\mathbf{R}')\, dV = \frac{1}{j\omega\mu_o}\,\hat{x} \tag{2.8}$$

Substitute equations (2.7) and (2.8) into (2.5), we obtain

$$\mathbf{A}(\mathbf{R}) = \frac{1}{j\omega}\, G_o(\mathbf{R}|\mathbf{R}')\,\hat{x} \tag{2.9}$$

If the electric field produced by this particularly oriented elementary source is denoted by $\overline{G}_o^{(x)}(\mathbf{R}|\mathbf{R}')$, then

$$\overline{G}_o^{(x)}(\mathbf{R}|\mathbf{R}') = (1 + \frac{1}{k^2} \nabla\nabla\cdot)\, G_o(\mathbf{R}|\mathbf{R}')\, \hat{x} \tag{2.10}$$

The above function is designated as a free-space Green's function with a source pointed in the x-direction. The associated wave equation is given by

$$\nabla \times \nabla \times \overline{G}_o^{(x)}(\mathbf{R}|\mathbf{R}') - k^2\overline{G}_o^{(x)}(\mathbf{R}|\mathbf{R}') = \delta(\mathbf{R} - \mathbf{R}')\, \hat{x} \tag{2.11}$$

Similarly, for vector sources pointing in the y and z-direction, we have two more vector Green's functions denoted, respectively, by $\overline{G}_o^{(y)}(\mathbf{R}|\mathbf{R}')$ and $\overline{G}_o^{(z)}(\mathbf{R}|\mathbf{R}')$. The equations for these two functions are

$$\overline{G}_o^{(y)}(\mathbf{R}|\mathbf{R}') = (1 + \frac{1}{k^2} \nabla\nabla\cdot)\, G_o(\mathbf{R}|\mathbf{R}')\, \hat{y} \tag{2.12}$$

$$\overline{G}_o^{(z)}(\mathbf{R}|\mathbf{R}') = (1 + \frac{1}{k^2} \nabla\nabla\cdot)\, G_o(\mathbf{R}|\mathbf{R}')\, \hat{z} \tag{2.13}$$

and with associated wave equations of

$$\nabla \times \nabla \times \overline{G}_o^{(y)}(\mathbf{R}|\mathbf{R}') - k^2\overline{G}_o^{(y)}(\mathbf{R}|\mathbf{R}') = \delta(\mathbf{R} - \mathbf{R}')\, \hat{y} \tag{2.14}$$

$$\nabla \times \nabla \times \overline{G}_o^{(z)}(\mathbf{R}|\mathbf{R}') - k^2\overline{G}_o^{(z)}(\mathbf{R}|\mathbf{R}') = \delta(\mathbf{R} - \mathbf{R}')\, \hat{z} \tag{2.15}$$

Equations (2.10), (2.11), and (2.13) can now be expressed in terms of a

free-space dyadic function defined by

$$\overline{\overline{G}}_o(\mathbf{R}|\mathbf{R}') = \overline{G}_o^{(x)}(\mathbf{R}|\mathbf{R}')\,\hat{x} + \overline{G}_o^{(y)}(\mathbf{R}|\mathbf{R}')\,\hat{y} + \overline{G}_o^{(z)}(\mathbf{R}|\mathbf{R}')\,\hat{z} \qquad (2.16)$$

with the associated dyadic differential equation given by

$$\nabla \times \nabla \times \overline{\overline{G}}_o(\mathbf{R}|\mathbf{R}') - k^2\overline{\overline{G}}_o(\mathbf{R}|\mathbf{R}') = \overline{\overline{I}}\,\delta(\mathbf{R} - \mathbf{R}') \qquad (2.17)$$

where $\overline{\overline{I}}$ denotes the idem factor (see Appendix A).

The EFIE can then be readily derived by an application of the vector Green's theorem (see Appendix B). If we substitute,

$$\mathbf{P}=\mathbf{E}(\mathbf{R}), \quad \mathbf{Q}=\overline{\overline{G}}_o(\mathbf{R}|\mathbf{R}')\mathbf{a} \qquad (2.18)$$

where $\mathbf{a}$ denotes a constant but arbitrary vector, into the vector Green's identity (B-5), we have

$$\int_v \left\{\mathbf{E}(\mathbf{R})\nabla\times\nabla\times\overline{\overline{G}}_o(\mathbf{R}|\mathbf{R}')\mathbf{a} - \left[\nabla\times\nabla\times\mathbf{E}(\mathbf{R})\right]\cdot\overline{\overline{G}}_o(\mathbf{R}|\mathbf{R}')\mathbf{a}\right\} dV$$

$$= -\int_s \left\{\left[\hat{n}\times\nabla\times\mathbf{E}(\mathbf{R})\right]\cdot\overline{\overline{G}}_o(\mathbf{R}|\mathbf{R}')\mathbf{a} + \left[\hat{n}\times\mathbf{E}(\mathbf{R})\right]\cdot\nabla\times\overline{\overline{G}}_o(\mathbf{R}|\mathbf{R}')\mathbf{a}\right\} dS \qquad (2.19)$$

where $\hat{n}$ denotes an outward unit vector normal to the surface S. The above equation can be simplified by replacing the terms $\nabla\times\nabla\times\mathbf{E}(\mathbf{R})$ and

$\nabla\times\nabla\times\overline{\overline{G}}_o(\mathbf{R}|\mathbf{R}')$ by the results of (2.3) and (2.17). Since

$$\int_V \mathbf{E}(\mathbf{R})\cdot\overline{\overline{I}}\,\delta(\mathbf{R}-\mathbf{R}')\,dV = \mathbf{E}(\mathbf{R}) \tag{2.20}$$

equation (2.19) can be written as

$$\mathbf{E}(\mathbf{R})\cdot\mathbf{a} = -j\omega\mu_o\int_V \mathbf{J}(\mathbf{R})\cdot\overline{\overline{G}}_o(\mathbf{R}|\mathbf{R}')\cdot\mathbf{a}\,dV$$

$$-\int_S \left\{[\hat{n}\times\nabla\times\mathbf{E}(\mathbf{R})]\cdot\overline{\overline{G}}_o(\mathbf{R}|\mathbf{R}')\cdot\mathbf{a} + [\hat{n}\times\mathbf{E}(\mathbf{R})]\cdot\nabla\times\overline{\overline{G}}_o(\mathbf{R}|\mathbf{R}')\cdot\mathbf{a}\right\} dS \tag{2.21}$$

Further reduction is done by replacing $\nabla\times\mathbf{E}$ by $-j\omega\mu_o\mathbf{H}$ and interchanging the primed and unprimed variables and deleting $(\cdot\mathbf{a})$ from the equation, hence yielding

$$\mathbf{E}(\mathbf{R}) = -j\omega\mu_o\int_V \mathbf{J}(\mathbf{R}')\cdot\overline{\overline{G}}_o(\mathbf{R}'|\mathbf{R})\,dV' - \int_S \{-j\omega\mu_o[\hat{n}\times\mathbf{H}(\mathbf{R}')]\cdot\overline{\overline{G}}_o(\mathbf{R}'|\mathbf{R})$$

$$+ [\hat{n}\times\mathbf{E}(\mathbf{R}')]\cdot\nabla'\times\overline{\overline{G}}_o(\mathbf{R}'|\mathbf{R})\}\,dS' \tag{2.22}$$

where $(\nabla'\times)$ means that the curl operation has to be performed in the primed coordinate system. If the volume is considered to be of infinite extent so that S recedes to infinity, then as a result of the radiation

condition for an electric field in free-space, the surface integral in equation (2.22) vanishes. Thus we have

$$\mathbf{E}(\mathbf{R}) = - j\omega\mu_o \int_V \mathbf{J}(\mathbf{R}')\cdot\overline{\overline{G}}_o(\mathbf{R}'|\mathbf{R})\, dV' = - j\omega\mu_o \int_V \overline{\overline{\tilde{G}}}_o(\mathbf{R}'|\mathbf{R})\cdot\mathbf{J}(\mathbf{R}')\, dV' \tag{2.23}$$

and since

$$\overline{\overline{\tilde{G}}}_o(\mathbf{R}'|\mathbf{R}) = \overline{\overline{G}}_o(\mathbf{R}|\mathbf{R}') \tag{2.24}$$

equation (2.23) becomes

$$\mathbf{E}(\mathbf{R}) = - j\omega\mu_o \int_V \overline{\overline{G}}_o(\mathbf{R}|\mathbf{R}')\cdot\mathbf{J}(\mathbf{R}')\, dV' \tag{2.25}$$

which is the EFIE of interest.

When the current distribution is limited to the surface of a perfectly conducting body, equation (2.25) becomes [5]

$$\mathbf{E}(\mathbf{R}) = - j\omega\mu_o \int_S \overline{\overline{G}}_o(\mathbf{R}|\mathbf{R}')\cdot\mathbf{J}_S(\mathbf{R}')\, dA' \tag{2.26}$$

with $\mathbf{J}_S$ the surface current density. The observation point $\mathbf{R}$ is restricted to be off the surface S so that $\mathbf{R}\neq\mathbf{R}'$. If $\mathbf{R}$ approaches S as a limit, equation

(2.26) becomes

$$\mathbb{E}(\mathbb{R}) = - j\omega\mu_o \int\!\!\!\!\!\!-_s \overline{\overline{G}}_o(\mathbb{R}|\mathbb{R}') \cdot \mathbb{J}_S(\mathbb{R}')\, dA' \tag{2.27}$$

where the principal value integral, $\int\!\!\!\!\!\!-$, is indicated since $G_o(\mathbb{R}|\mathbb{R}')$ is now unbounded.

2.2.2 Numerical Solution Methods

In this section, the numerical solution method used to solve the EFIE in NEC2 is outlined. A detail description of the numerical solution can be found in part I of the NEC2 manual.

The EFIE in the previous section is solved numerically in NEC2 by a form of the method of moments. The integral equation can be expressed as a general linear-operator equation of the form [5]

$$Lf = e \tag{2.28}$$

where f is an unknown response, e is a known excitation, and L is a linear operator (an integral operator in the present case). The unknown function f may be expanded in a sum of basis functions as

$$f = \sum_{j=1}^{N} \alpha_j f_j \tag{2.29}$$

where the α_j are constants to be determined and the functions f_j are dependent and in the domain of the operator. In order to solve for the coefficients α_j , a set of equations are formed by utilizing the inner product. The inner product over S of two tangential vectors P and Q is defined as

$$\langle P, Q \rangle = \int_s P \cdot Q \, ds \tag{2.30}$$

By taking the inner product of equation (2.28) with a set of weighting functions $\{w_i\}$, we have

$$\langle w_i, Lf \rangle = \langle w_i, e \rangle , \qquad i=1, 2, ..., N \tag{2.31}$$

Due to the linearity of L, equation (2.29) and (2.31) can be combined to yield

$$\sum_{j=1}^{N} \alpha_j \langle w_i, Lf_j \rangle = \langle w_i, e \rangle , \qquad i=1, 2, ..., N \tag{2.32}$$

The above equation can be written in matrix notation as

$$[G]\,[A] = [E] \tag{2.33}$$

where $G_{ij} = \langle w_i, Lf_j \rangle$, $A_j = \alpha_j$, $E_i = \langle w_i, e \rangle$. The solution can then be found by a matrix inversion scheme give by

$$[A] = [G]^{-1}\,[E] \tag{2.34}$$

Various choices exist for the weighting and basis functions. In NEC2 the basis and weighting functions are different with $\{w_i\}$ being chosen as a set of delta functions

$$w_i(\mathbf{r}) = \delta(\mathbf{r} - \mathbf{r}_i) \tag{2.35}$$

with $\{\mathbf{r}_i\}$ a set of pointers on the conductor surface. The result is a point sampling of the integral equation known as the collocation method of solution. The choice of basis functions depends on many factors such as convenience in computation, stability of the resulting matrix, speed of convergence, etc. In NEC2, wires are modeled by short straight segments

with the current on each segments represented by three terms - a constant, a sine, and a cosine. This basis function, which makes use of a sinusoidal interpolation procedure, is first used by Yeh and Mei [8]. The sinusoidal interpolation converges much faster than the trapezoidal method and has the added advantage that the fields of the sinusoidal currents are easily evaluated in closed form. The amplitudes of the constant, sine, and cosine terms are related such that their sum satisfies physical conditions on the local behavior of current and charge at the segment ends. The total current on segment j in NEC2 has the form

$$I_j(s) = A_j + B_j \sin k(s-s_j) + C_j \cos k(s-s_j), \qquad |s-s_j| < \frac{\Delta_j}{2} \tag{2.36}$$

where s_j is the value of s at the center of segment j and Δ_j is the length of segment j. Among the three unknown constants A_j, B_j, and C_j, two are eliminated by local conditions on the current leaving one constant, related to the current amplitude to be determined by the matrix equation.

The local condition which relates the current on a wire segment to the linear charge density, q, is the equation of continuity defined by

$$\frac{\delta I}{\delta s} = -j\omega q \tag{2.37}$$

At a junction of two segments with uniform radius, the obvious conditions are that the current and charge are continuous at the junction. While at a junction of two or more segments with unequal radii, the continuity of current is generalized to Kirchoff's current law which states that the sum of currents into the junction is assumed to distribute itself on individual

wires according to the wire radii, neglecting local coupling effects. T.T. Wu and R.W.P. King [9] have derived a condition that the linear charge density on a wire at a junction, and hence $\delta I/\delta s$, is determined by

$$\left.\frac{\delta I(s)}{\delta s}\right|_{s \text{ at junction}} = \frac{Q}{\ln\left(\frac{2}{ka}\right) - \gamma} \tag{2.38}$$

where a = wire radius, $k = 2\pi/\lambda$, $\gamma = 0.5772$ (Euler's constant), and Q is a constant for all wires at the junction that relates the total charge in the vicinity of the junction.

At a free wire end, the current may be assumed to go to zero. On a wire of finite radius, however, the current can flow onto the end cap and hence be nonzero at the wire end. Poggio [10] derived a condition which relates the current at the wire end to the current derivative, and for a wire of radius a, this condition is

$$\left.I(s)\right|_{s \text{ at end}} = \frac{-(\hat{s}\cdot\hat{n}_c)}{k}\frac{J_1(ka)}{J_0(ka)}\left.\frac{\delta I(s)}{\delta s}\right|_{s \text{ at end}} \tag{2.39}$$

where J_0 and J_1 are Bessel functions of order 0 and 1. The unit vector $\hat{n}_c$ is normal to the end cap. Hence, $\hat{s}\cdot\hat{n}_c$ is +1 if the reference direction, $\hat{s}$, is toward the end, and -1 if $\hat{s}$ is away from the end.

At this stage, two local conditions are obtained for both segments junctions:

$$\left.\frac{\delta I_j(s)}{\delta s}\right|_{s=s\pm\frac{\Delta_j}{2}} = \frac{Q_j^{\pm}}{\ln(\frac{2}{ka_j}) - \gamma} \qquad (2.40)$$

and for free ends:

$$I_j(s_j\pm\frac{\Delta_j}{2}) = \frac{\pm 1}{k}\frac{J_1(ka)}{J_0(ka)}\left.\frac{\delta I_j(s)}{\delta s}\right|_{s=s\pm\frac{\Delta_j}{2}} \qquad (2.41)$$

The two additional unknowns Q_j^+ and Q_j^- are associated with the junctions but can be eliminated by Kirchoff's current equation at each junction.

To apply these conditions, the current is expanded in a sum of basis functions chosen so that they satisfy the local conditions on current and charge in any linear combination. Referring to Figure 2.1, the portion of the i^{th} basis function on segment i is

$$f_i^o(s) = A_i^o + B_i^o \sin k(s-s_i) + C_i^o \cos k(s-s_i), \qquad |s-s_i| < \frac{\Delta_i}{2} \qquad (2.42)$$

Over segments connected to left end of segment i, the i^{th} basis function is

$$f_j^-(s) = A_j^- + B_j^- \sin k(s-s_j) + C_j^- \cos k(s-s_j),$$
$$|s-s_j| < \frac{\Delta_j}{2} \qquad j = 1, 2, \ldots, N^- \qquad (2.43)$$

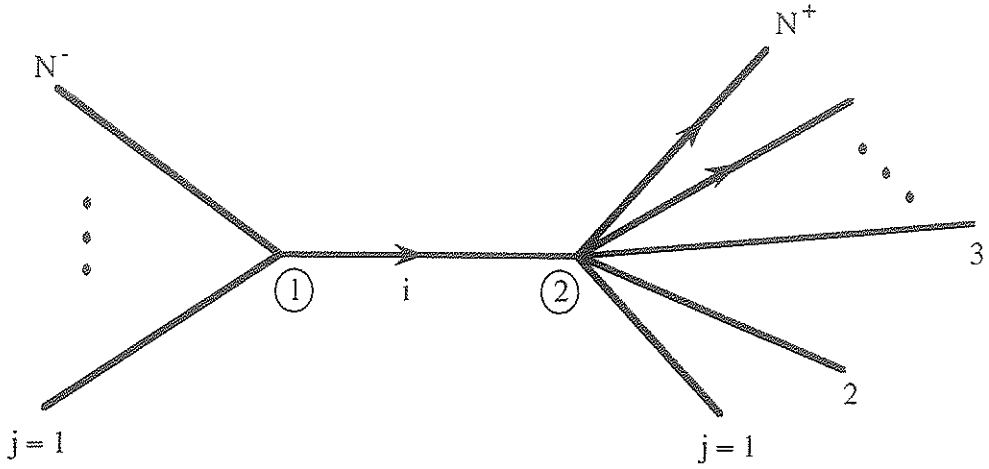

Figure 2.1 Segments Covered by the i^{th} Basis Function.

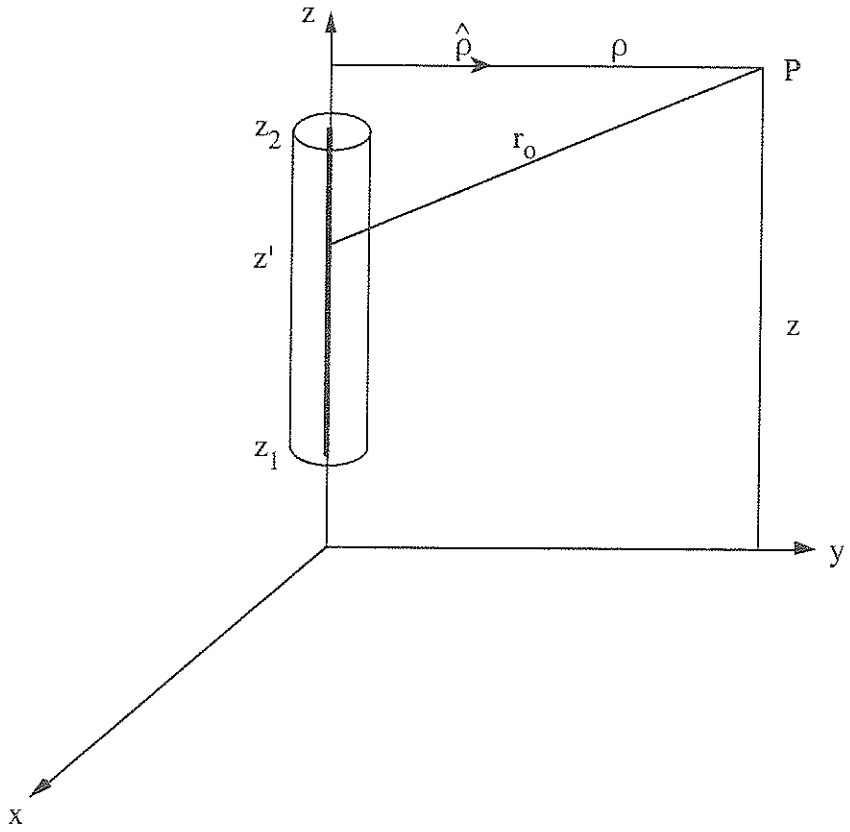

Figure 2.2 Current Filament Geometry for the Thin-Wire Kernel.

Over segments connected to right end of segment i, the i^{th} basis function is

$$f_j^+(s) = A_j^+ + B_j^+ \sin k(s-s_j) + C_j^+ \cos k(s-s_j),$$
$$|s-s_j| < \frac{\Delta_j}{2} \qquad j = 1, 2, ..., N^+ \tag{2.44}$$

With the help of the local conditions defined in (2.40) and (2.41), together with the two Kirchoff's current equations given by

$$\sum_{j=1}^{N^-} f_j^-(s_j+\frac{\Delta_j}{2}) = f_i^o(s_i-\frac{\Delta_i}{2})$$

$$\sum_{j=1}^{N^+} f_j^+(s_j+\frac{\Delta_j}{2}) = f_i^o(s_i-\frac{\Delta_i}{2}) \tag{2.45}$$

the complete basis function is then defined in terms of one unknown constant. In this case A_i^o is set to -1 since the function amplitude is arbitrary, being determined by the boundary condition equations. The resulted coefficients can be found in Part I of [5] and hence will not be repeated here. A condition worth mentioning is that when a segment end is connected to a ground plane, the end condition on both the total current and the last basis function is

$$\frac{\delta}{\delta s} I_j(s) \Big|_{s = s_j \pm \frac{\Delta_j}{2} = 0} = 0 \tag{2.46}$$

replacing the zero current condition at a free end. This condition does not require a separate treatment, however, but is obtained by computing the last basis function as if the last segment is connected to its image segment on the other side of the surface.

With the current on each wire segment at hand, the solution then requires the evaluation of the electric field at each segment due to this current. For most cases, the thin-wire approximation of the integral equation kernel is used. The accuracy of the thin-wire approximation for a wire of radius a and length Δ depends on the value of ka and Δ/a. Studies have shown that the thin-wire approximation leads to errors of less than 1% for Δ/a greater than 8 [11].

For the thin-wire kernel, the source current is approximated by a filament on the segment axis while the observation point is on the surface of the observation segment. The fields are evaluated with the source segment on the axis of a local cylindrical-coordinate system as illustrated in Figure 2.2.

The ρ and z components of the electric field at P due to the sine and cosine currents are:

For

$$I = I_o \begin{pmatrix} \sin kz' \\ \cos kz' \end{pmatrix}, \tag{2.47}$$

$$E_\rho^f(\rho,z) = \frac{-I_o}{\lambda} \frac{j\eta}{2k^2\rho} G_o \left\{ k(z-z') \begin{pmatrix} \cos kz' \\ -\sin kz' \end{pmatrix} + \left[1-(z-z')^2(1+jkr_o)\frac{1}{r_0^2} \right] \begin{pmatrix} \sin kz' \\ \cos kz' \end{pmatrix} \right\} \Big|_{z_1}^{z_2}, \tag{2.48}$$

$$E_z^f(\rho,z) = \frac{I_o}{\lambda} \frac{j\eta}{2k^2} G_o \left\{ k \begin{pmatrix} \cos kz' \\ -\sin kz' \end{pmatrix} - (1+jkr_o)(z-z')\frac{1}{r_0^2} \begin{pmatrix} \sin kz' \\ \cos kz' \end{pmatrix} \right\} \Big|_{z_1}^{z_2}. \tag{2.49}$$

For a constant current of strength I_o ,

$$E_\rho^f(\rho,z) = -\frac{I_o}{\lambda}\frac{j\eta\rho}{2k^2}\left[(1 + jkr_o)\frac{G_o}{r_o}\right]_{z_1}^{z_2}, \tag{2.50}$$

$$E_z^f(\rho,z) = -\frac{I_o}{\lambda}\frac{j\eta}{2k^2}\left\{\left[(1 + jkr_o)(z-z')\frac{G_0}{r_o}\right]_{z_1}^{z_2} + k^2\int_{z_1}^{z_2} G_o\, dz'\right\} \tag{2.51}$$

where

$$G_o = \frac{\exp(-jkr_o)}{r_o}$$

$$r_o = \sqrt{\rho^2 + (z-z')^2} \tag{2.52}$$

The matrix equation (2.33) is then solved in NEC2 by Gauss elimination method.

2.2.3 Calculation of Antenna Factor

With the knowledge of the unknown currents on a wire biconical antenna, the usual parameters, such as input impedance, gain, and radiation pattern can be obtained. Another very useful parameter, the antenna factor (AF), is introduced as an index to the performance of the antennas being examined in this study. An antenna factor is [12] "that factor that, when properly applied to the reading of the measuring instrument, yields the electric field strength in volts per meter or the magnetic field strength in amperes per meter... This factor include the effects of antenna effective length and mismatch and transmission line losses." Antenna factors are widely used and are useful, for example, in situations where the magnitude of the electric field strength |E| at a particular location in space is desired. If an antenna placed at that location is connected to a measuring receiver the input voltage of which is V_r, then the desired antenna factor is equal to $|E/V_r|$. The measurement of |E| can then be effected by forming the product of the antenna factor and $|V_r|$.

Measurement wise, the options available for establishing accurate antenna factors are somewhat limited. One recourse is to take advantage of the antenna calibration services offered by the National Bureau of Standards (NBS) [13]. The two calibration methods used by NBS are [14]: the standard-antenna method (SAM) and the standard-field method (SFM). The SAM uses a standard receiving antenna consisting of a self-resonant half-wave dipole with a high-impedance balanced voltmeter build into the center. The antenna is placed at a fixed height above ground in the far-

field of a transmitting dipole. The transmitting power is set to a convenient level and held constant while the magnitude of the field is measured. The antenna being calibrated is substituted in place of the standard antenna, and the antenna factor is calculated as the ratio of the field to the received voltage. In the SFM, a predetermined value of field strength is established at a given point in space by transmitting a known amount of power with an antenna having a known gain at a specified distance. The uncertainty of antenna factors calibrated by NBS is estimated to be 1dB. A third method of calibration, called the standard-site method (SSM), which requires neither the availability of a standard antenna nor the generation of a standard field, was suggested by Smith [13]. The method is based on site attenuation measurements made on a near-ideal, open-field site. The implementation of the SSM requires only a spectrum analyzer and tracking generator (or field-strength meter and signal generator) and its accuracy depends on the quality of the measuring site.

Mathematically, the AF of a receiving antenna is defined as [4]

$$AF = \frac{E}{V_r} \tag{2.53}$$

where E is the incident field strength at the antenna (assuming that the polarization of the antenna is the same as that of the incoming wave), and V_r is the voltage at the input of the measuring receiver. By considering the transmission losses as negligible or at least easily accountable for

separately, the AF can be expressed by the power at the receiver

$$P_r = \frac{V_r^2}{R_r} \tag{2.54}$$

and the power at the receiving antenna

$$P_r = A_e S_{av} \tag{2.55}$$

where R_r is the input resistance of the receiver, A_e is the effective aperture of the receiving antenna, and S_{av} is the time-average power density of the incoming wave.

Since

$$A_e = \frac{M G_r(\theta,\phi) \lambda^2}{4\pi} \tag{2.56}$$

and

$$S_{av} = \frac{E^2}{Z_o} \tag{2.57}$$

we obtain from (2.55)

$$P_r = \frac{M G_r(\theta,\phi) \lambda^2 E^2}{4\pi Z_o} \tag{2.58}$$

where from transmission line theory

$$M = 1 - \frac{P_{ref}}{P_{inc}} = 1 - |\rho|^2 \leq 1 \tag{2.59}$$

is the impedance mismatch factor, indicating the fraction of received power transmitted across the antenna-transmission line junction defined by its voltage reflection coefficient ρ. And $G_r(\theta,\phi)$ is the power gain of the antenna as a function of the angle of arrival of the energy, and $Z_o = 120\pi$ Ω is the intrinsic impedance of free space.

From equations (2.54), (2.55), and (2.58), we get

$$AF = \frac{2}{\lambda}\sqrt{\frac{\pi Z_o}{G_r(\theta,\phi)\, R_r\, M}} \qquad (2.60)$$

In decibels, with $R_r = 50\ \Omega$, equation (2.60) becomes

$$AF(dBm^{-1}) = 19.7657 - 20\log\lambda - M(dB) - G_r(dBi) \qquad (2.61)$$

where G_r is taken at $\theta = 90°$, and $\phi = 0$ in this study. Once the power gain and mismatch factor are known, (2.61) can be used to obtain the antenna factor.

2.3 MODELING WIRE BICONICAL ANTENNAS

A planar wire model of a finite biconical antenna is shown in Figure 2.3. Some characteristic parameters of the antenna include the flare angle (θ_f), the hat angle (θ_h), and the antenna half-length (A). By following the structural modeling guideline of NEC2 and utilizing the image theory, the antenna can be modeled as shown in Figure 2.4. Two source segments are inserted between the antenna and ground, since sources are represented as wire segments in NEC2. Obviously, the model is not unique as many other source configurations are possible. Some of the parameters used in the wire model are quite arbitrary, an example of this being the wire radius (a). In [2], Smith and Butler used the wire diameter of 0.695 electrical degrees at 600 MHz which means a approximately equals 0.5 mm. Figure 2.5 shows good agreement between the calculated input impedance obtained from NEC2 and the measured ones from [2] for a wire biconical antenna with a=0.5 mm, θ_f=60°, θ_h=180°.

In order to investigate the effects of changing wire radius on the impedance characteristics of a wire biconical antenna, the input impedance of an antenna with θ_f=60°, θ_h=180°, and different values of a is plotted in Figure 2.6. From the figure, it can be seen that changing the wire radius has significant effect on the antenna's input impedance at antiresonant frequencies.

A body-of-revolution (or 3D) model of a finite biconical antenna is

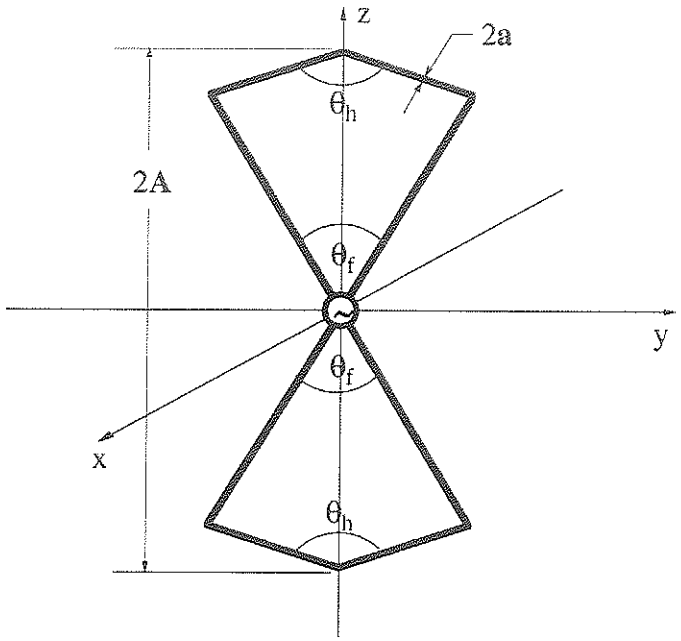

Figure 2.3 Typical Configuration of a Finite Wire Biconical Antenna (Antenna is in the y-z Plane).

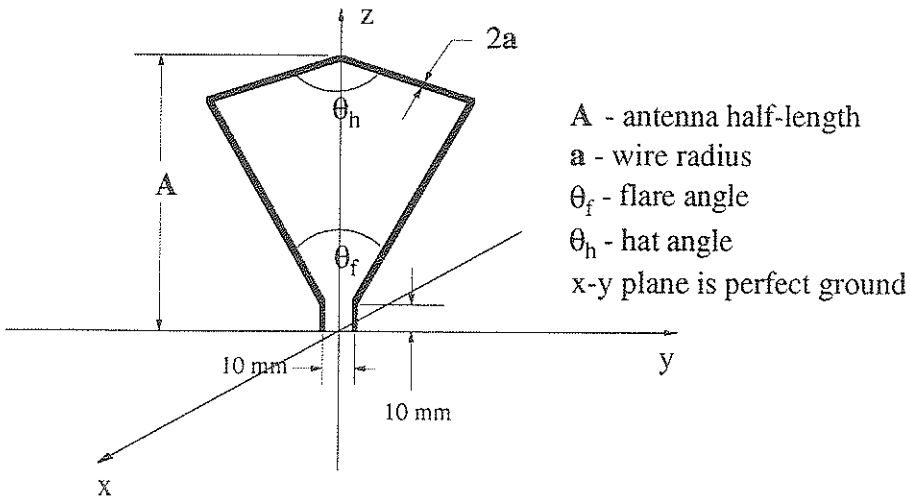

Figure 2.4 Planar Wire Model of the Finite Biconical Antenna.

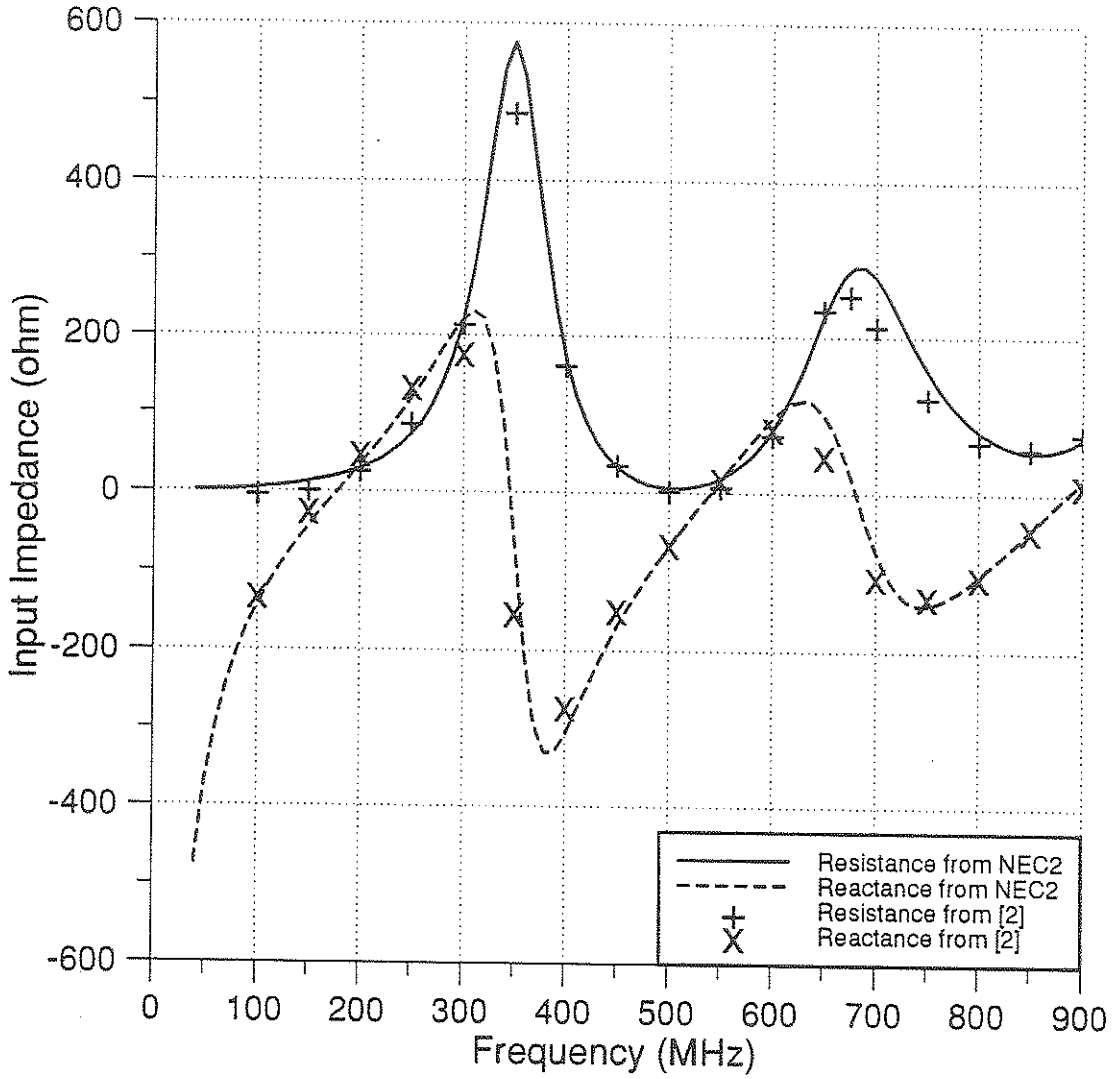

Figure 2.5 Computed and Measured Input Impedance of a Bowtie Antenna with θ_f=60°.

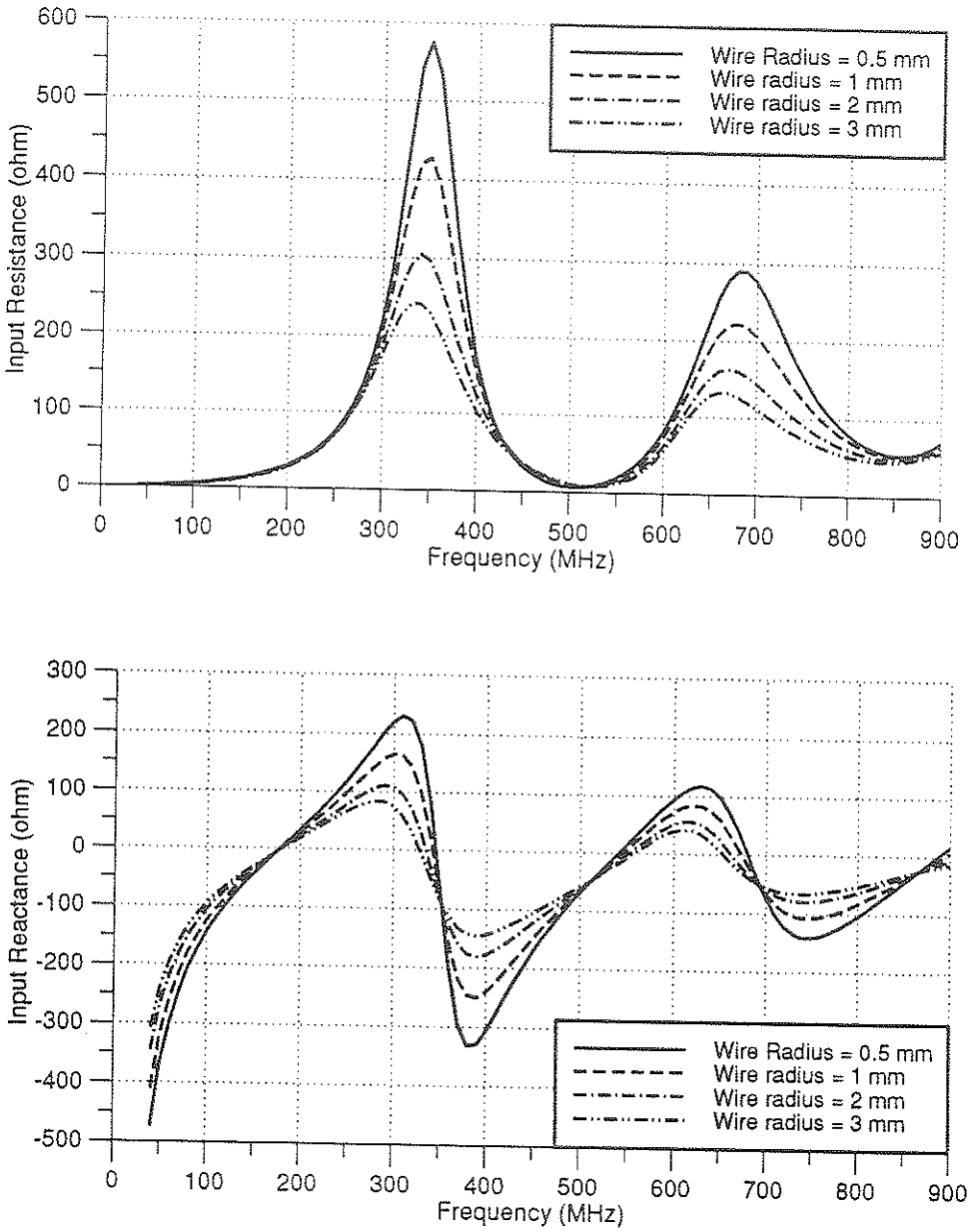

Figure 2.6 Computed Input Impedance of a Bowtie Antenna with θ_f=60° and Half Length of 25 cm for Various Wire Radii.

shown in Figure 2.7. The structure is formed by intersecting N planar wire antenna with equal angular spacing. As the number of wire elements (N) becomes very large, the radiating surface approaches that of a solid biconical antenna. Hence, the characteristics of such a wire-segmented structure should approximate those of the equivalent body-of-revolution structure. By means of calculation, Smith and Butler [2] found that if $N \geq 8$, then such low-mass structure can be employed, with confidence, to predict the broadband performance of the solid antenna. Following this rule of thumb, the input impedance of a 3D wire biconical antenna with N=8, $\theta_f=30^\circ$, $\theta_h=180^\circ$, and **a**=0.5 mm is obtained from NEC2. The computed results are then compared to the measured ones from [3] for a solid antenna (Figure 2.8). Undoubtedly, good agreement between the two results is observed. The characteristics of the biconical models are, however, sensitive to wire radius changes. As an example, Figure 2.9 shows good agreement between the input impedances calculated by the NEC2 and those measured from [3] for a wire model with $\theta_f=60^\circ$, $\theta_h=180^\circ$, and a wire radius of 3 mm.

Besides its ability to predict the input impedance of a wire biconical antenna, the NEC2 can also be used to obtain the antenna's radiation pattern. In fact, the radiation pattern is usually the more accurate characteristic to compute compared with the input impedance, since accurate impedance calculation requires that careful attention be paid to the model in the immediate vicinity of the source, whereas the radiation pattern can be obtained with a much coarser geometry. Figures 2.10 and

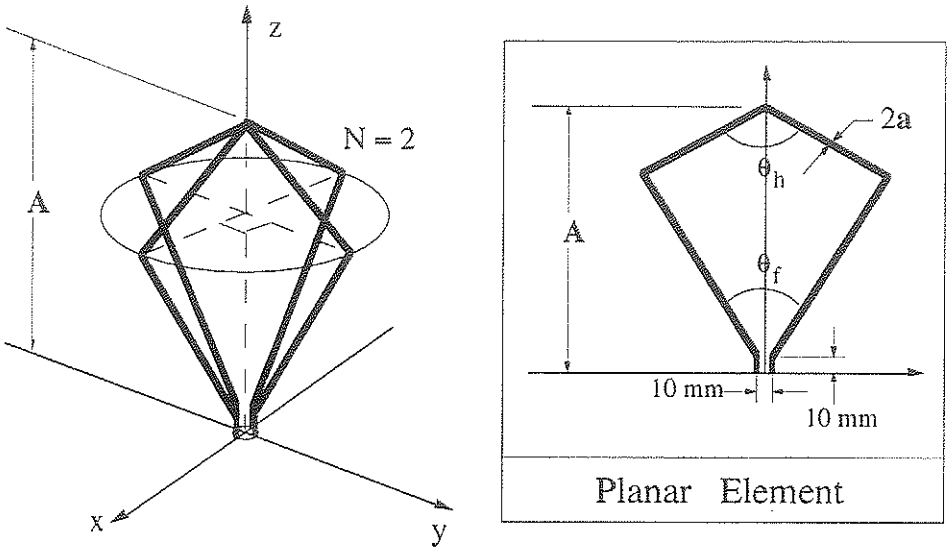

Figure 2.7 Body of Revolution Model of the Finite Wire Biconical Antenna.

2.11 depict the computed electric field (normalized E_θ component) patterns, for antenna half-lengths (A) from 60 to 270 electrical degrees, of 3D (N=8) wire biconical antennas with θ_f=30° and 60° respectively. Similar curves corresponding to a solid antenna have been obtained by means of measurement in [3]. When the computed results are compared with the measured ones, it is found that the agreement between the two is good for half-lengths of up to 180°. Above A=180°, the computed results are distinctly different from the measured ones. This is due to the increasing distance between adjacent wires of the diverging wire model in comparison to wavelengths.

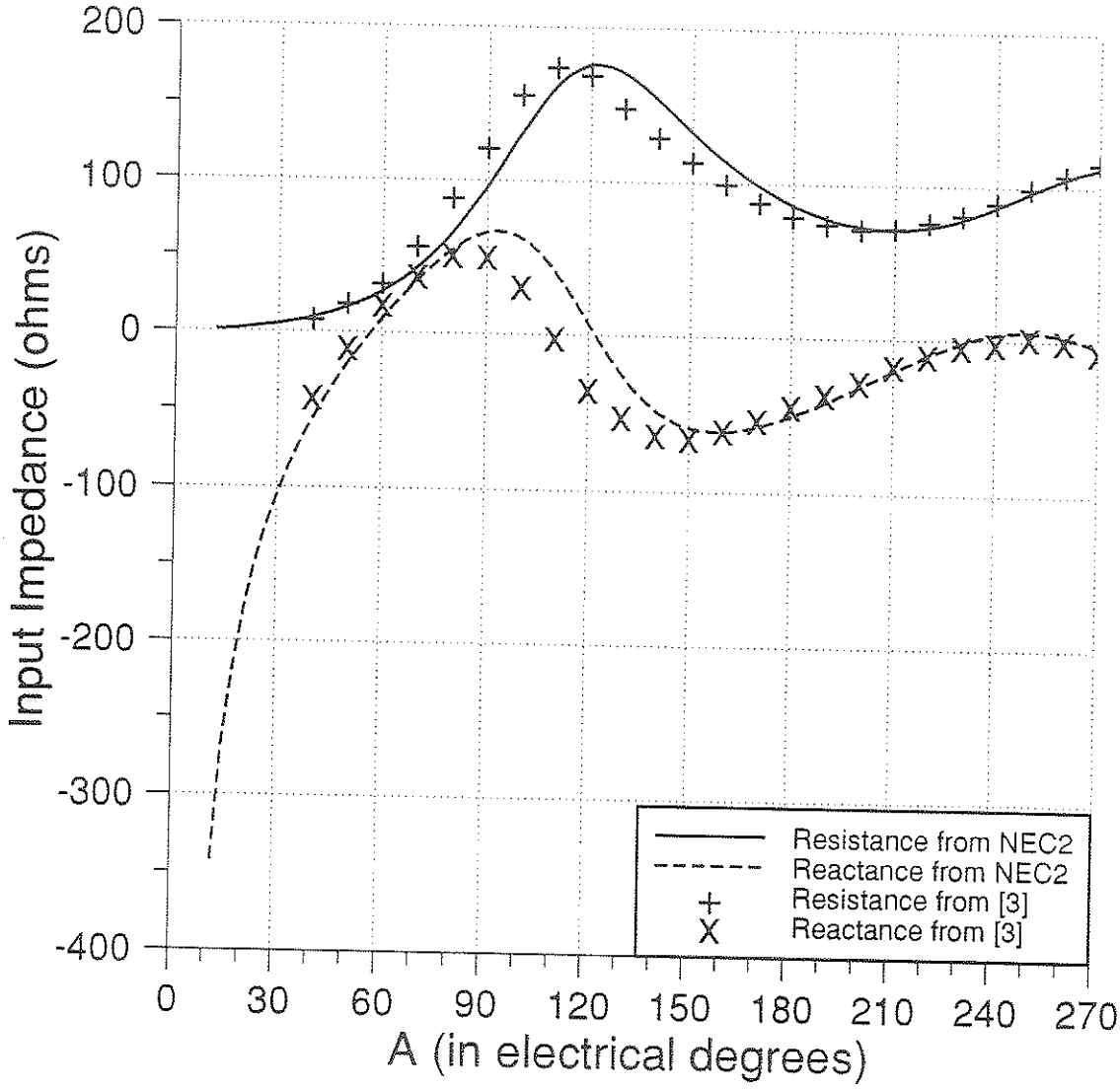

Figure 2.8 Computed and Measured Values of the Input Impedance of an Eight-Element Conical Monopole with $\theta_f = 30°$ and **a** = 0.5 mm.

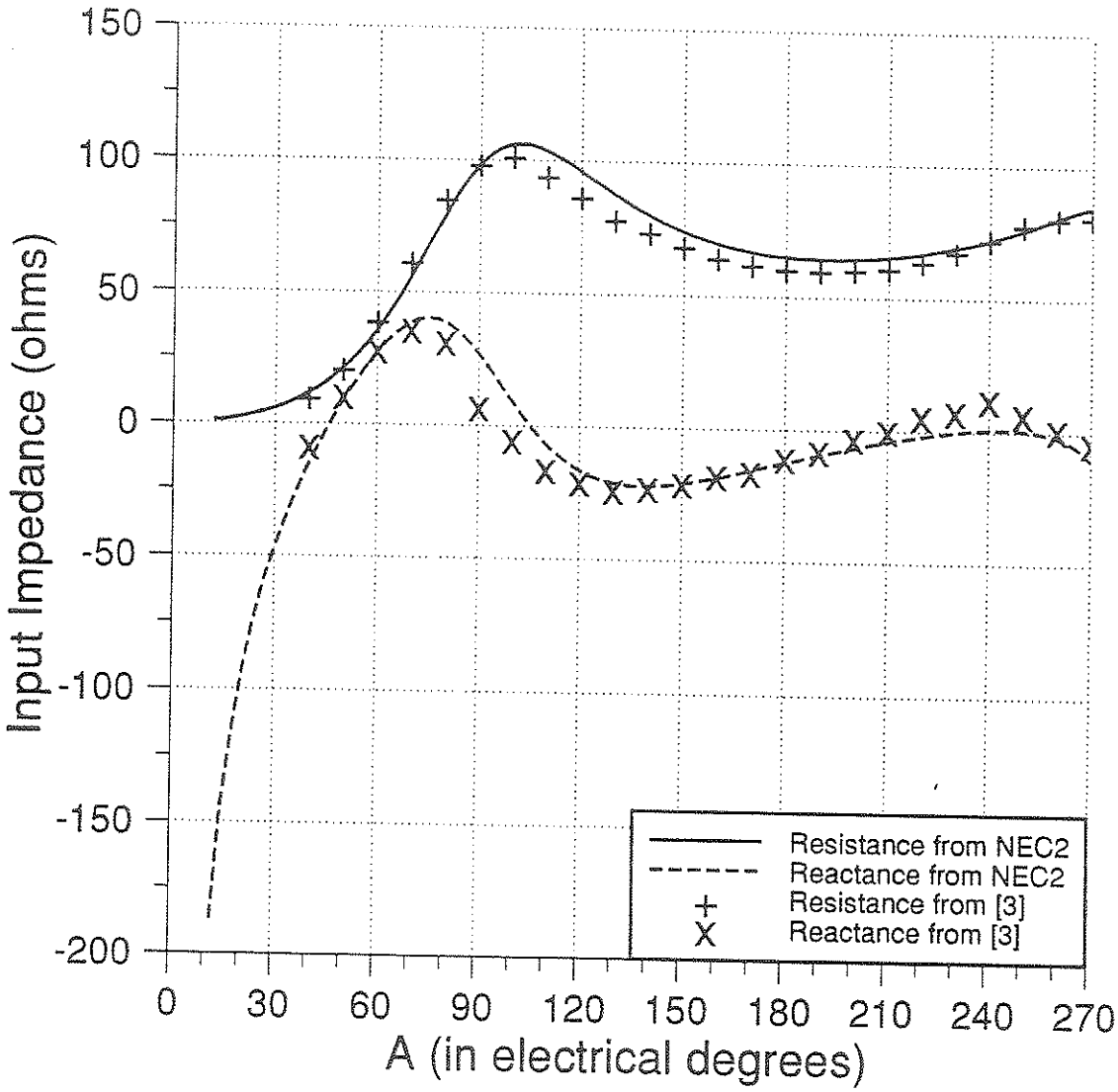

Figure 2.9 Computed and Measured Values of the Input Impedance of an Eight-Element Conical Monopole with $\theta_f = 60^\circ$ and $\mathbf{a} = 3$ mm.

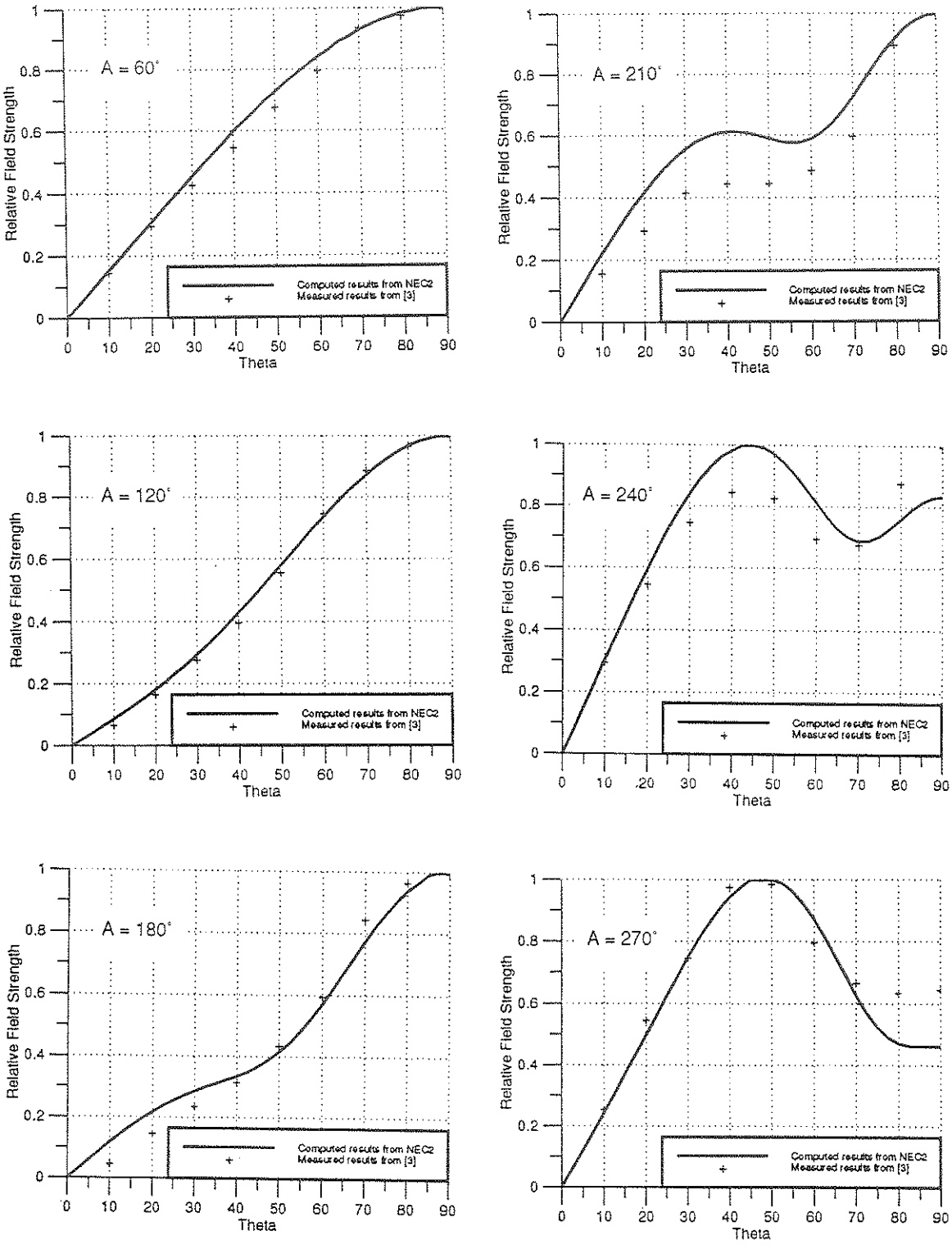

Figure 2.10 Comparison Between Computed and Measured Field Patterns (normalized E_θ Component) of a Biconical Antenna with Flare Angle of 30° and Antenna Half Lengths from 60° to 270°.

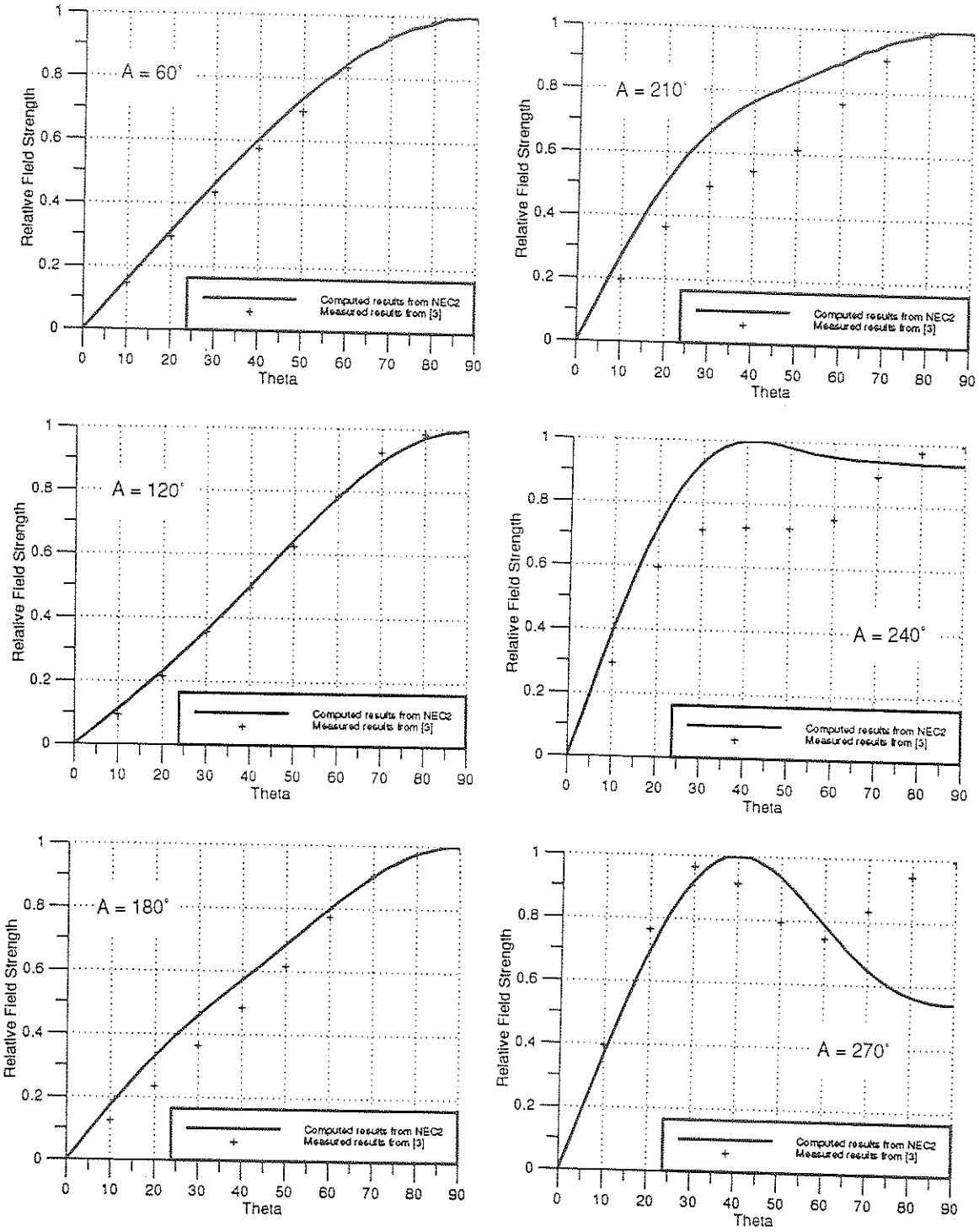

Figure 2.11 Comparison Between Computed and Measured Field Patterns (normalized E_θ Component) of a Biconical Antenna with Flare Angle of 60° and Antenna Half Lengths from 60° to 270°.

CHAPTER III

PERFORMANCE OF WIRE BICONICAL ANTENNAS

3.1 INTRODUCTION

The characteristics of wire biconical antennas have been investigated by a number of authors in various publications. This chapter attempts to compliment those existing studies by analyzing wire biconical antennas in a systematic approach. The effects of hat and flare angle changes on the antenna characteristics will first be studied for both the planar and the body-of-revolution cases. This is achieved by computing and comparing the radiation patterns and input impedances of the wire biconical antennas with various flare and hat angles. Besides these usual parameters, the antenna factor described in section 2.2.3 is also used to evaluate the antennas being examined. The antenna factors of the various antennas are computed and the results are used to compare the performances of the antennas. Finally, the antenna with corner reflector system will be examined. Namely, all the aforementioned characteristics of a wire biconical antenna with θ_f=60°, θ_h=120°, and A=25 cm is compared with the characteristics of the same antenna put in front of a corner reflector with a height of 75 cm and an apex angle of 45°.

3.2 PLANAR MODEL

The far field E_θ component of bowtie antennas with $\theta_f = 30°$ and $60°$ as a function of the zenith angle θ at $\phi = 90°$ for various frequencies are computed using the NEC2 and the results are plotted in Figures 3.1 and 3.2. For the $\phi = 0°$ plane, the patterns are essentially the same at low frequencies as shown in Figures 3.3 and 3.4. However, at high frequencies, differences in side lobe structures for the two planes appear due to the structural differences evident in the two planes. To illustrate the effects of flare angle (θ_f) variation on the radiation pattern, the far field patterns of bowtie antennas with $\theta_f = 15°$ to $75°$ in $15°$ increment at frequencies of 200 MHz and 700 MHz for the $\phi = 90°$ and $0°$ planes are plotted in Figures 3.5 and 3.6 respectively. It is noted that despite a change in absolute field strength, the structure of the radiation patterns appears similar for all flare angles. Similar observations are concluded for a change in hat angle as shown in Figure 3.7 and 3.8 where the far field patterns of bowtie antennas with $\theta_f = 45°$ and hat angles of $\theta_h = 180°$ to $120°$ in $15°$ decrements at frequencies of 200 MHz and 700 MHz for the $\phi = 90°$ and $0°$ planes are plotted, respectively. It should be noted that for all angle variations, the antenna half length (A) and the wire radius (a) of the antennas remain the same.

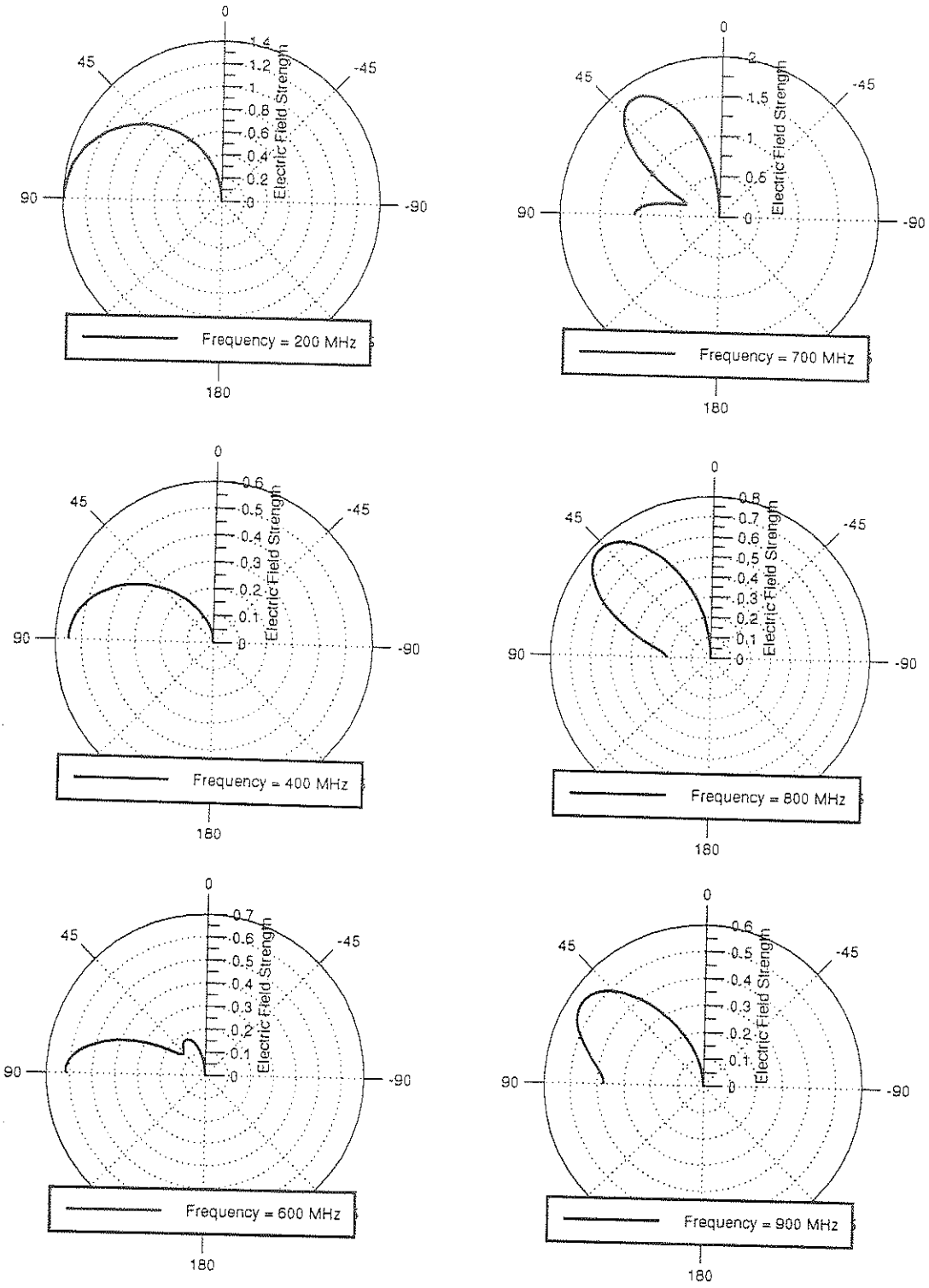

Figure 3.1 Far Electric Field (E_θ) Patterns of a Bowtie Antenna with θ_f=30° as a Function of Zenith Angle θ for Various Frequencies and ϕ= 90°.

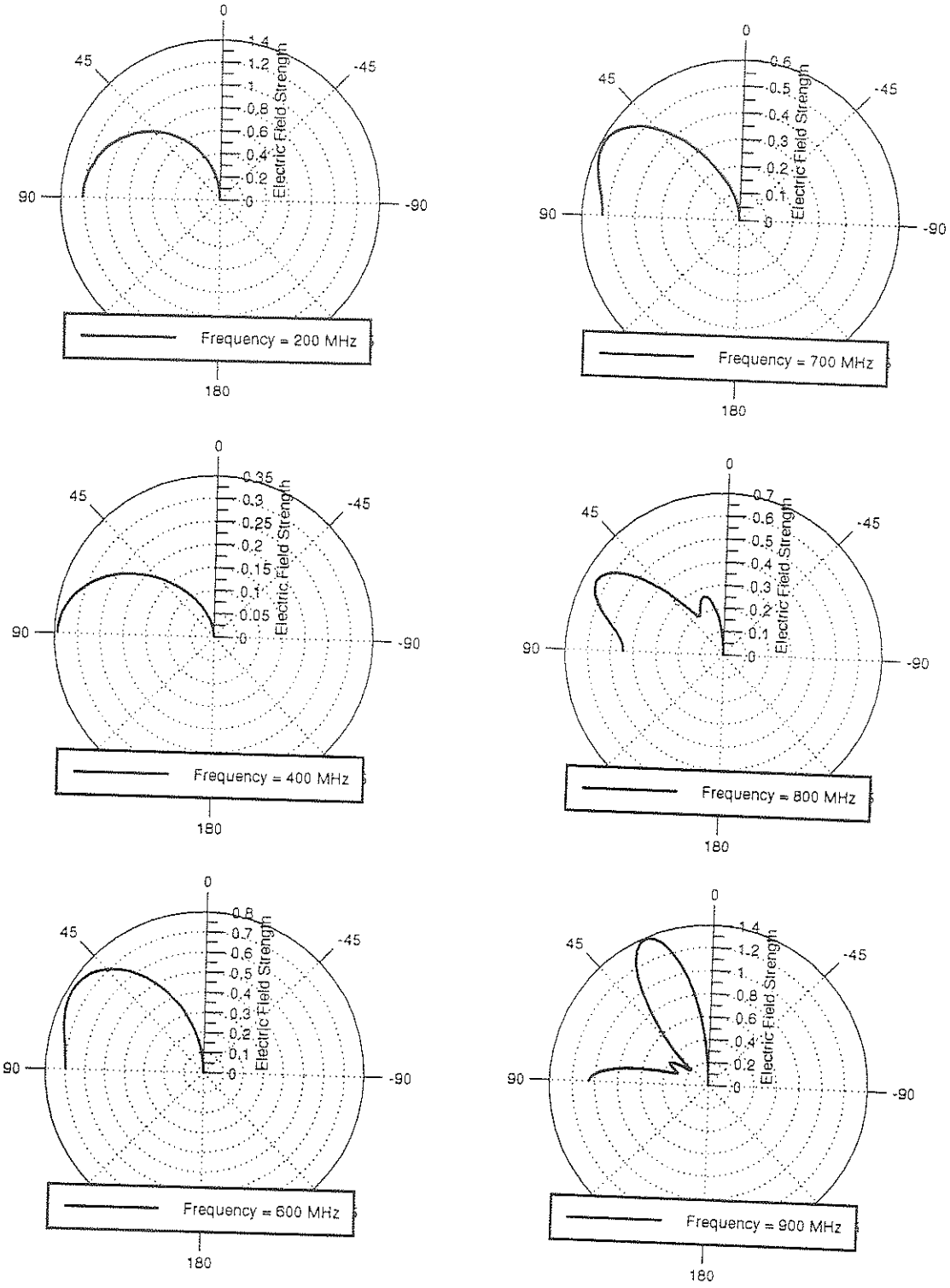

Figure 3.2 Far Electric Field (E_θ) Patterns of a Bowtie Antenna with θ_f=60°as a Function of Zenith Angle θ for Various Frequencies and ϕ= 90°.

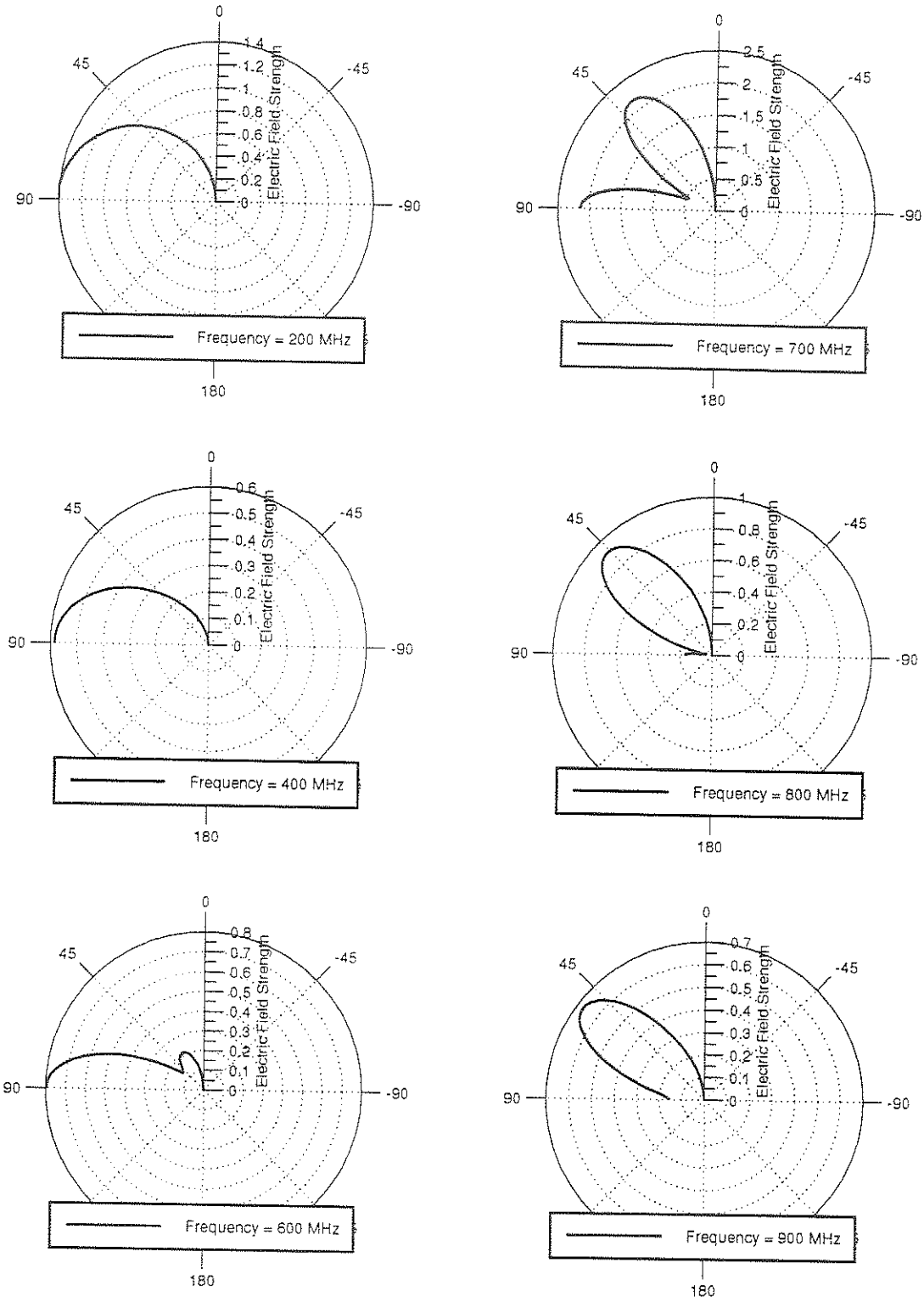

Figure 3.3 Far Electric Field (E_θ) Patterns of a Bowtie Antenna with θ_f=30° as a Function of Zenith Angle θ for Various Frequencies and ϕ= 0°.

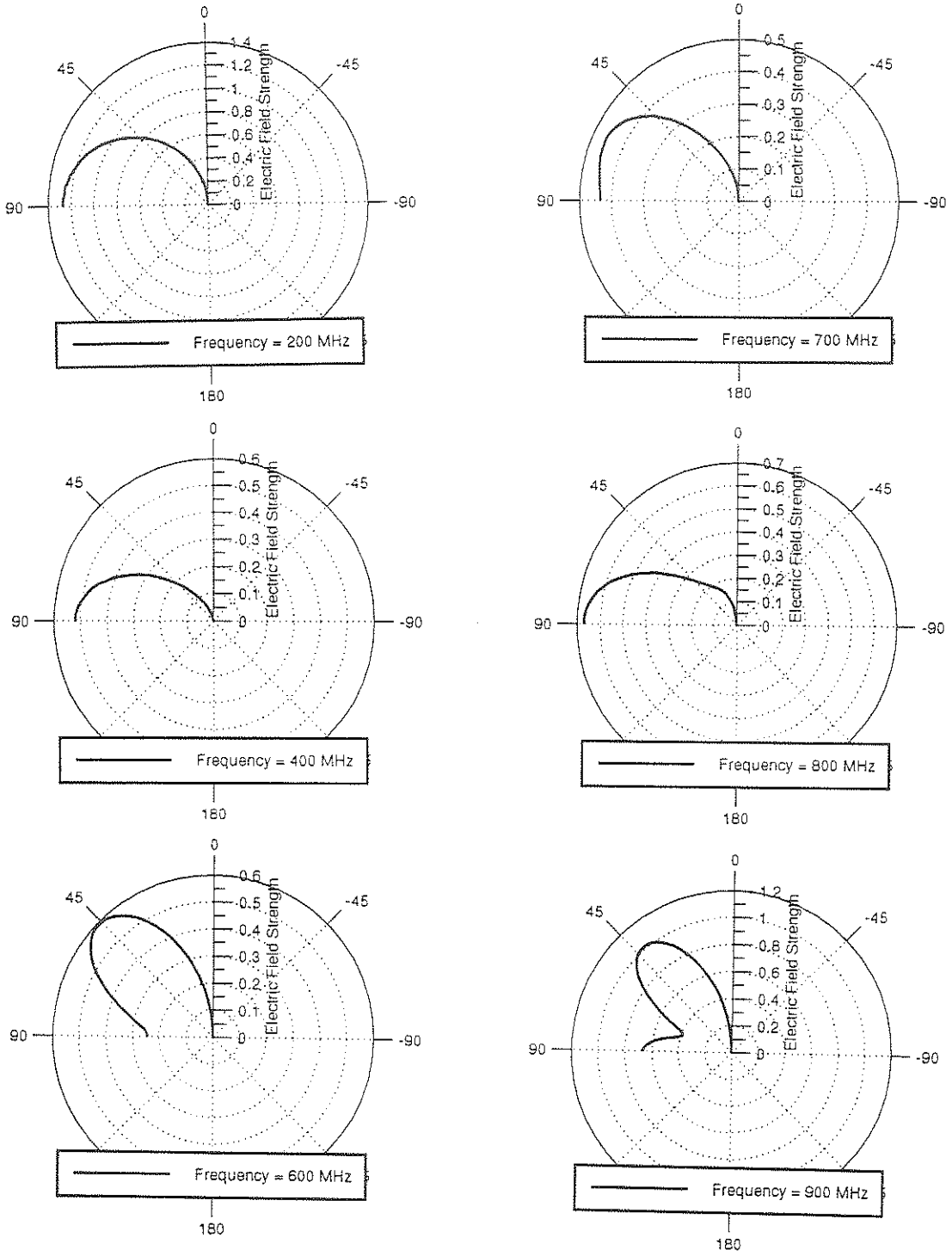

Figure 3.4 Far Electric Field (E_θ) Patterns of a Bowtie Antenna with θ_f=60° as a Function of Zenith Angle θ for Various Frequencies and ϕ= 0°.

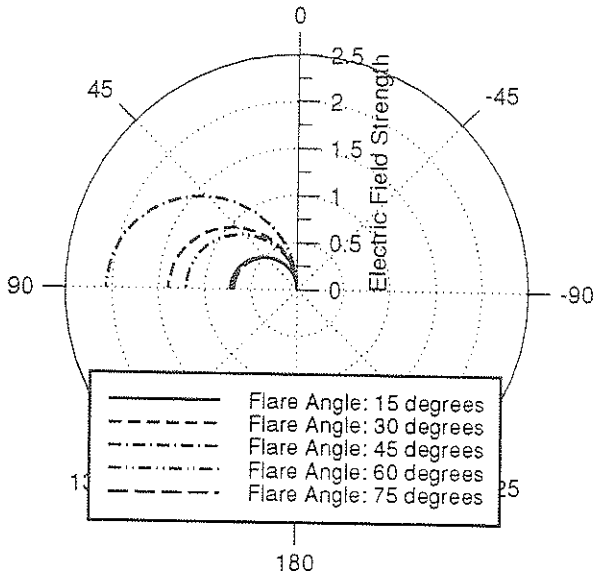

(a)

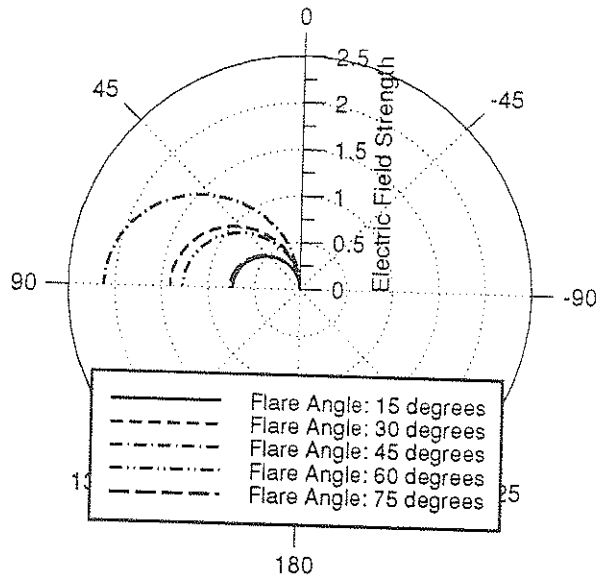

(b)

Figure 3.5 Far Electric Field (E_θ) Patterns of Bowtie Antennas with Various θ_f as a Function of Zenith Angle θ at 200 MHz for: (a) the ϕ=90° Plane; and (b) the ϕ=0° Plane.

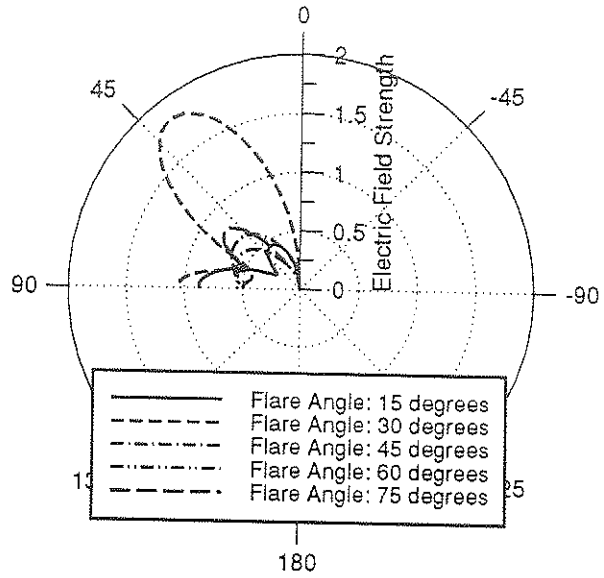

(a)

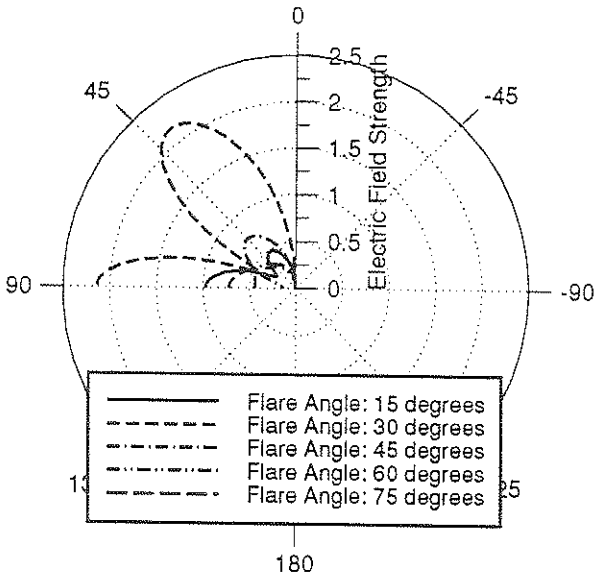

(b)

Figure 3.6 Far Electric Field (E_θ) Patterns of Bowtie Antennas with Various θ_f as a Function of Zenith Angle θ at 700 MHz for: (a) the ϕ=90° Plane; and (b) the ϕ=0° Plane.

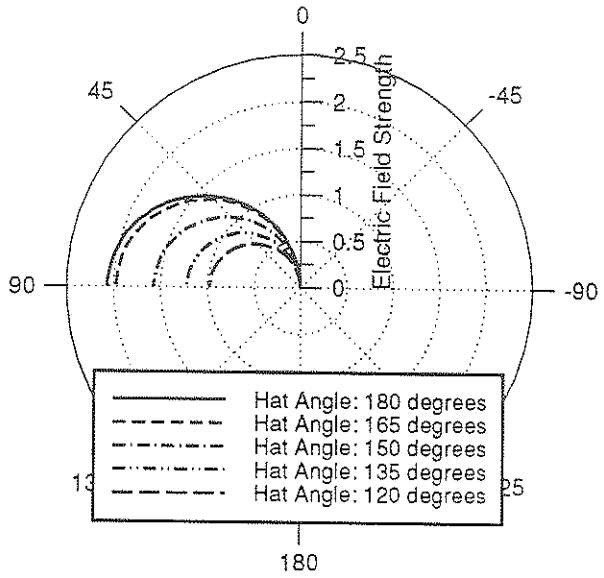

(a)

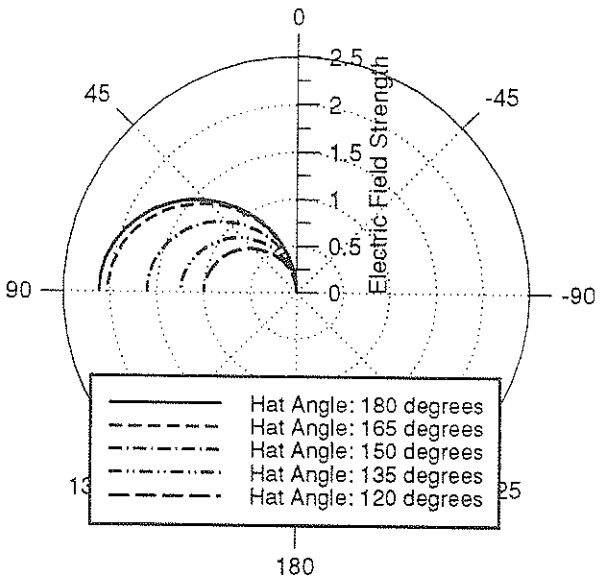

(b)

Figure 3.7 Far Electric Field (E_θ) Patterns of Planar Wire Biconical Antennas with θ_f=45° and Various Hat Angle as a Function of Zenith Angle θ at 200 MHz for: (a) the ϕ=90° Plane; and (b) the ϕ=0° Plane.

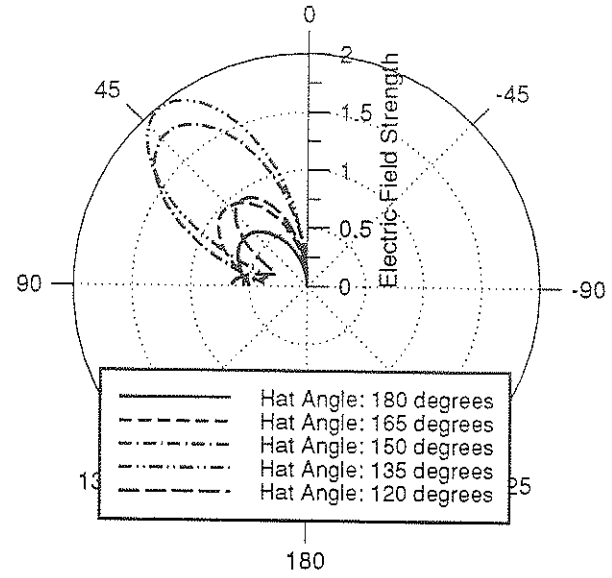

(a)

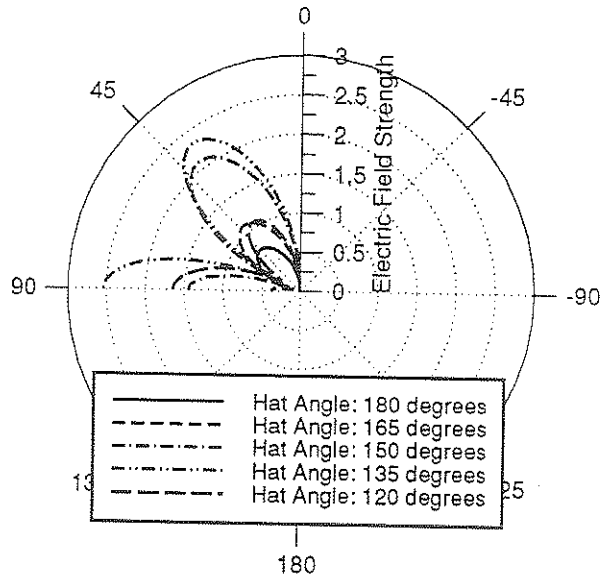

(b)

Figure 3.8 Far Electric Field (E_θ) Patterns of Planar Wire Biconical Antennas with θ_f=45° and Various Hat Angle as a Function of Zenith Angle θ at 700 MHz for: (a) the ϕ=90° Plane; and (b) the ϕ=0° Plane.

The effect of flare angle variation on the impedance characteristics of a bowtie antenna above ground is studied using the NEC2. For frequencies varying from 40 MHz to 900 MHz and flare angles ranging from 15° to 75° in 15° increments, the input impedance of a bowtie antenna is shown in Figure 3.9. As expected, the results obtained are similar to those in [2] with corresponding flare angles. The effects of hat angle variation can be seen in Figures 3.10 where a bowtie antenna with $\theta_f = 45°$ is subjected to hat angle change of $\theta_h = 180°$ to 120° in 15° decrements. Apparently, decreasing the hat angle while keeping the flare angle unchanged has similar effects on the input impedance as increasing the flare angle while keeping the hat angle unchanged.

From the power gain and the mismatch factor (as specified in section 2.2.3) of the antenna, the antenna factor of wire antennas with different flare and hat angles are computed. Figure 3.11 shows all three values for a bowtie antenna with flare angle of 30° at frequencies from 40 MHz to 900 MHz. As shown in the figure, the increase in antenna factor is caused by the drop in power gain. To compare their performances, the antenna factors of bowtie antennas with flare angles of 15° to 75° in 15° increments are plotted in Figure 3.12, while the antenna factors of bowtie antennas with flare angle of 45° and hat angles of 180° to 120° in 15° decrements are shown in Figure 3.13. As discussed in section 2.2.3., for a receiving antenna, the lower the antenna factor means the better the receptive power. With that in mind, it is not hard to recognize that some flare and hat angle combinations perform better than others at selected frequencies.

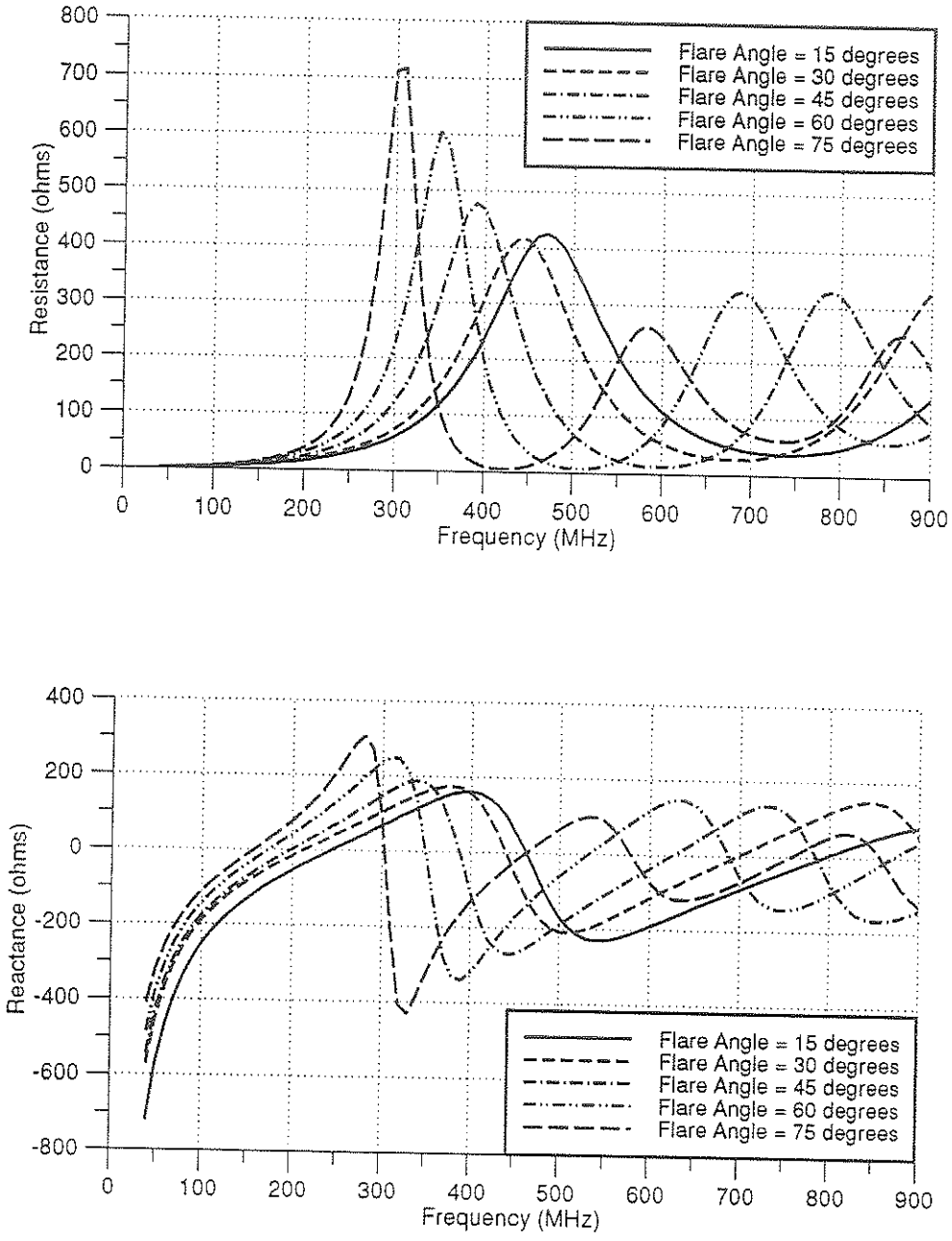

Figure 3.9 Input Impedance Curves of Bowtie Antennas with Various θ_f.

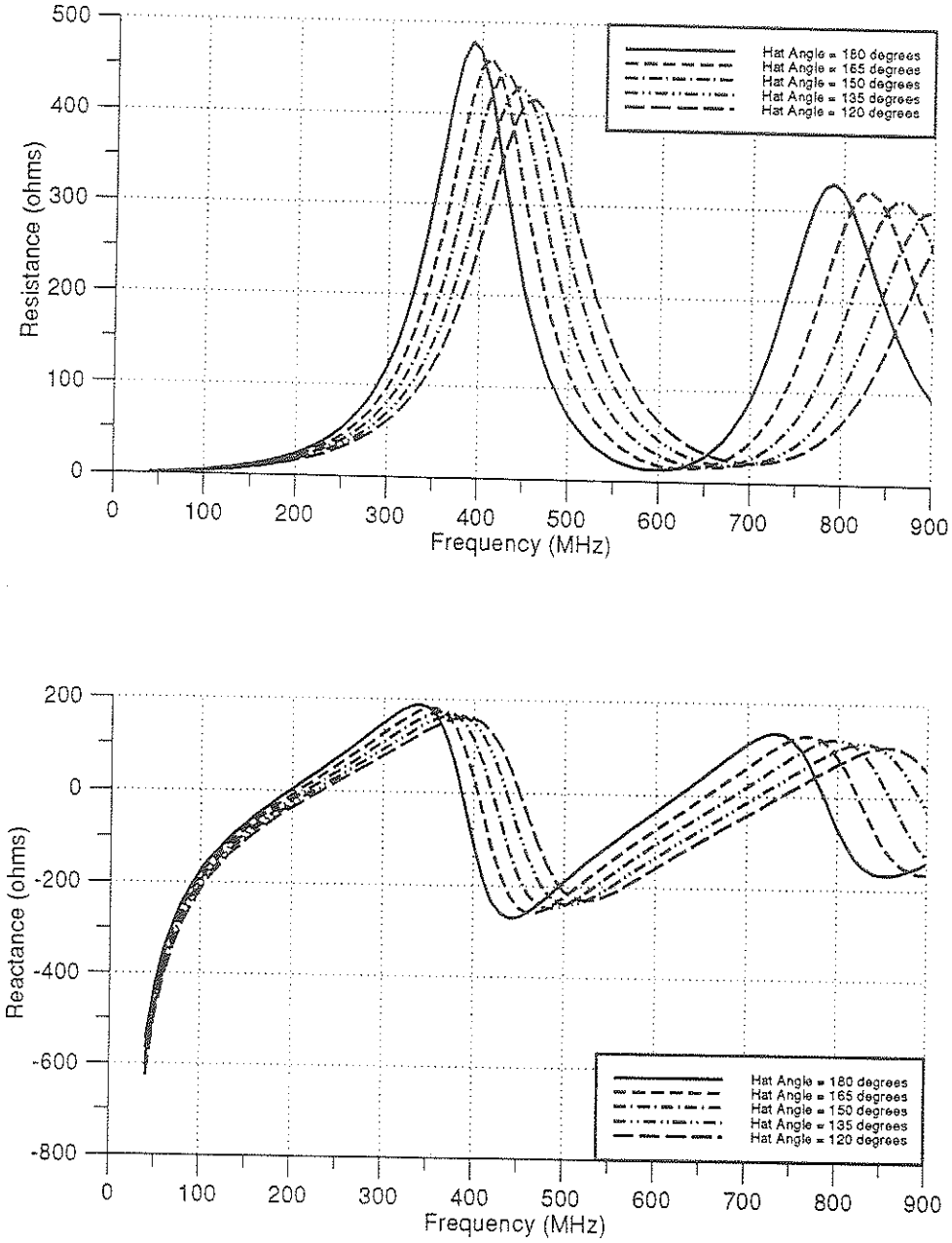

Figure 3.10 Input Impedance Curves of Planar Wire Biconical Antennas with θ_f=45° and Various Hat Angles.

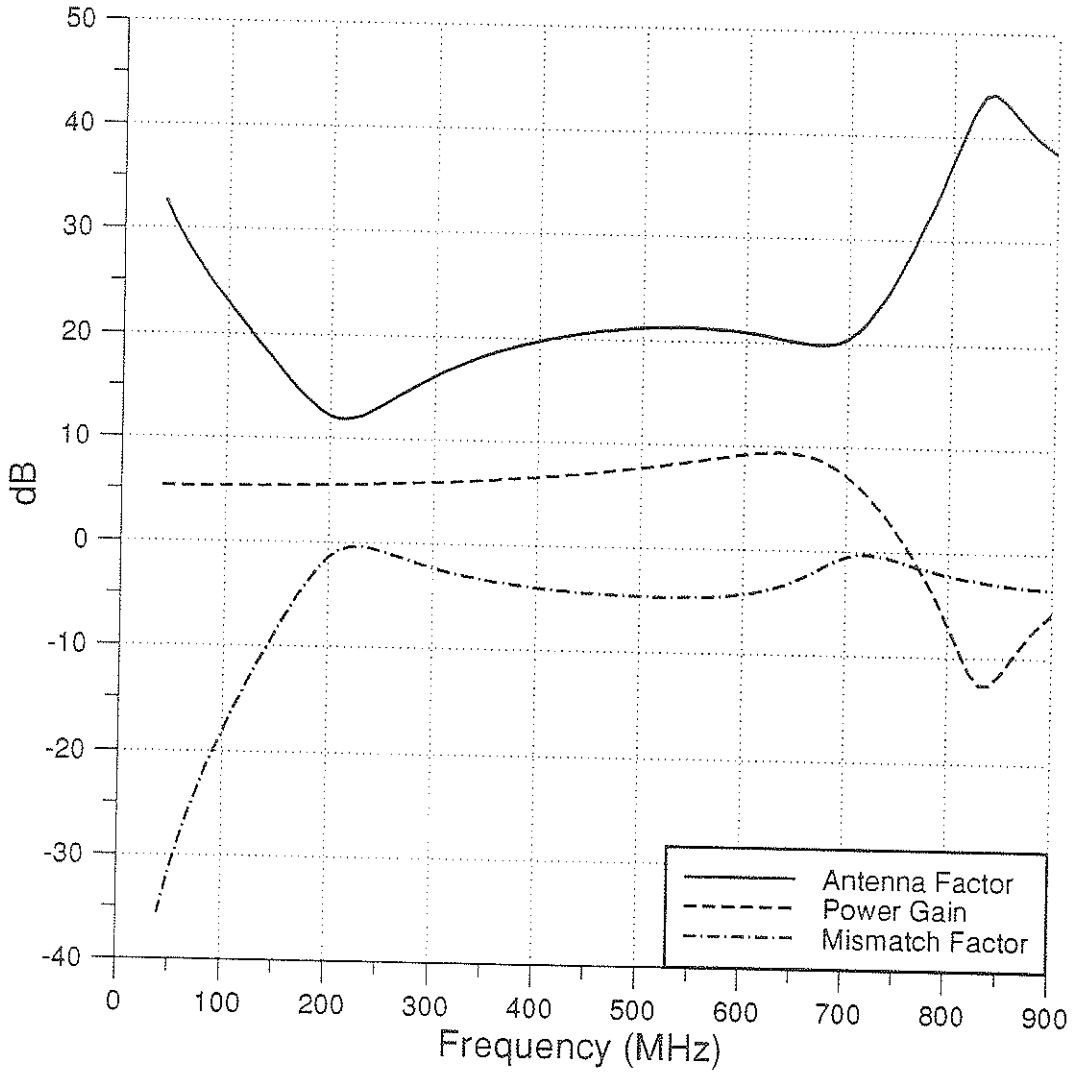

Figure 3.11 Antenna Factor, Power Gain (at θ=90° and ϕ=0°), and Mismatch Factor (for 50Ω) Curves of a Bowtie Antenna with θ_f=30°.

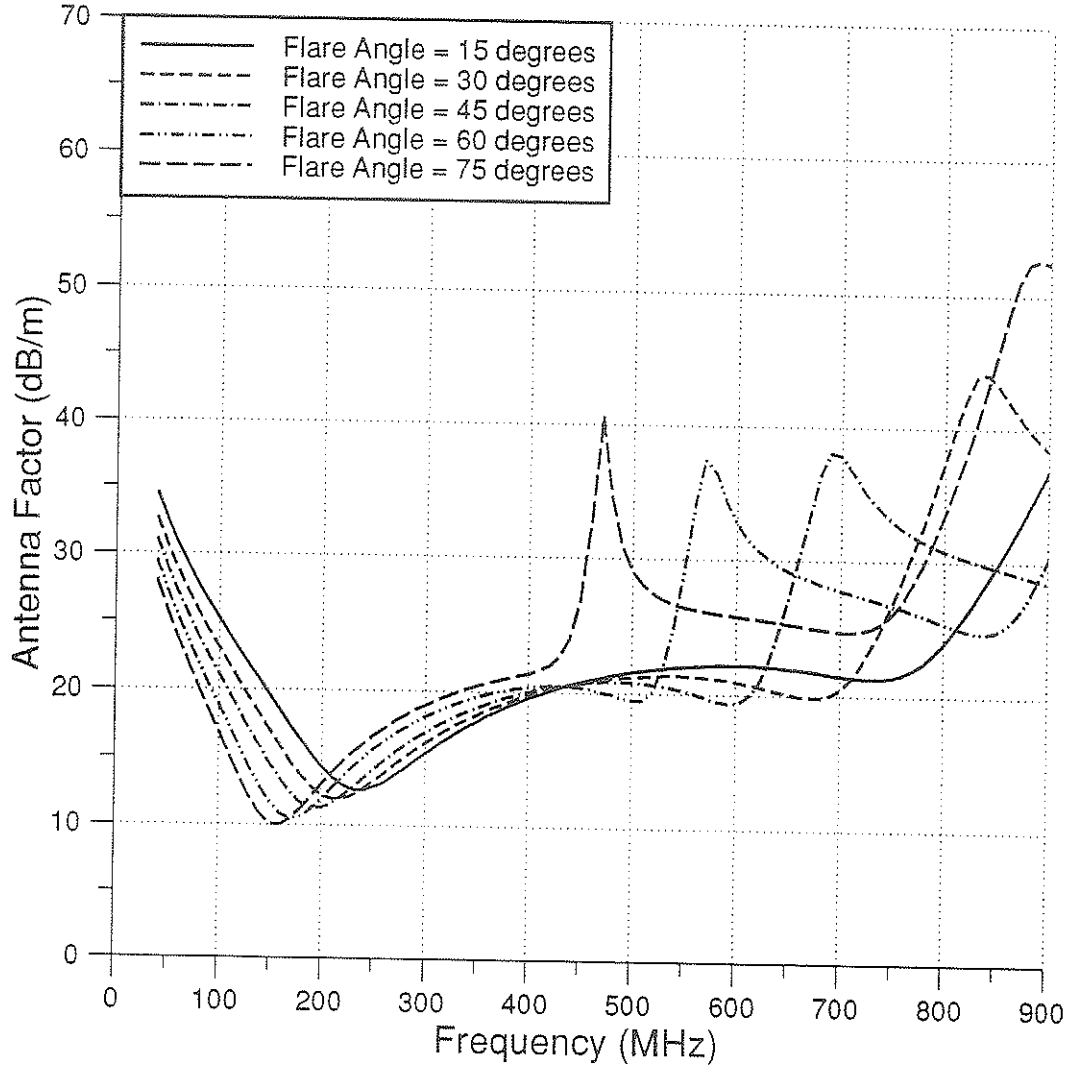

Figure 3.12 Antenna Factor Curves of Bowtie Antennas with Various θ_f.

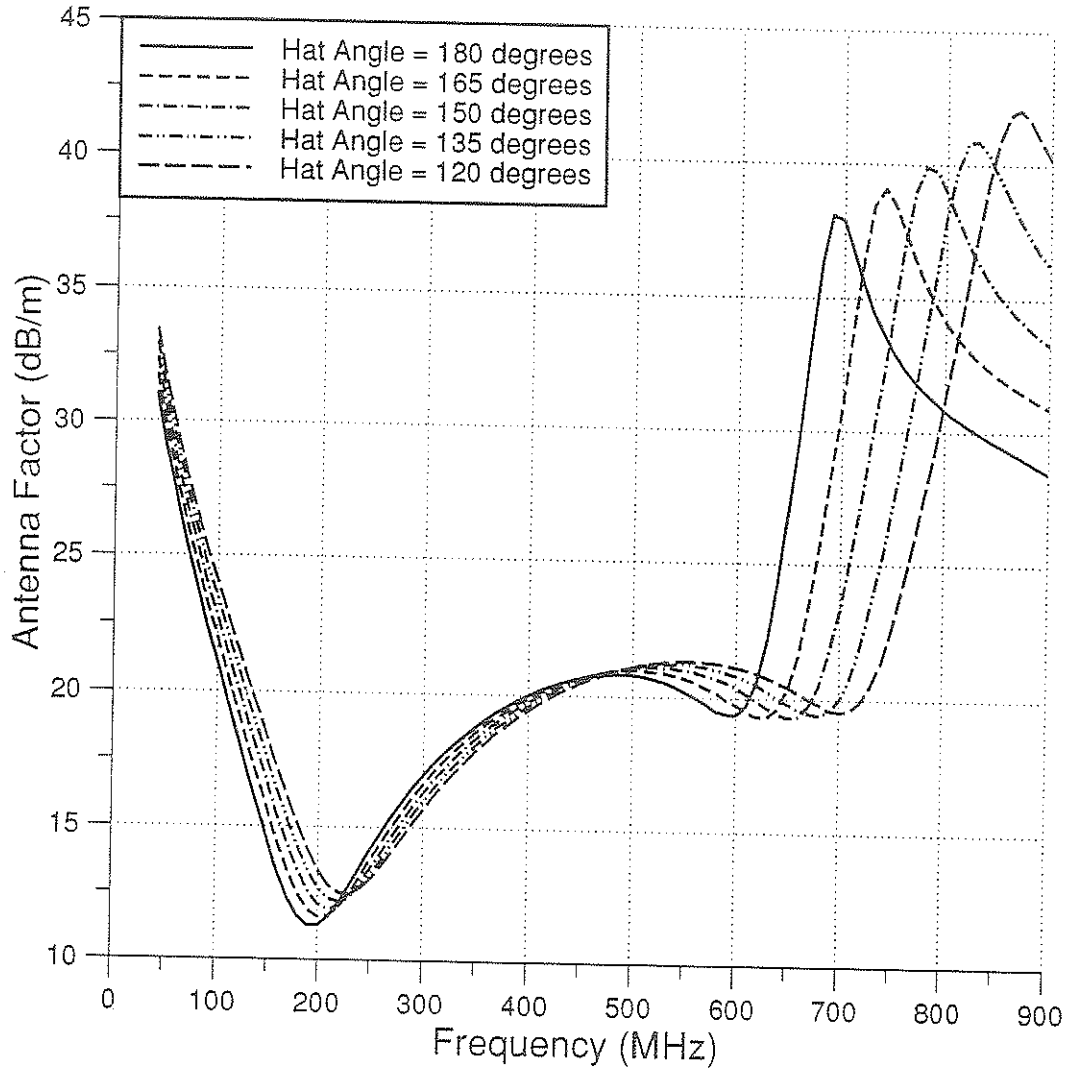

Figure 3.13 Antenna Factor Curves of Planar Wire Biconical Antennas with θ_f=45° and Various Hat Angles.

3.3 BODY-OF-REVOLUTION MODEL

The body-of-revolution model of the wire biconical antenna, or the phantom antenna as it is sometimes referred to, is widely used in commercial applications. Figures 3.14 and 3.15 shows, respectively, the far field (E_θ) radiation patterns of such an antenna with conical angles (θ_f) of 30° and 60° and hat angle (θ_h) of 180° as a function of zenith angle θ for various frequencies. When the flare angle is changed from 30° to 60° in 10° steps, the change in radiation pattern is shown in Figure 3.16 for frequencies of 200 and 700 MHz. Since the antenna is symmetrical about the z-axis, the patterns are the same for the $\phi = 90°$ and $\phi = 0°$ planes. The far field patterns of biconical antennas with conical angle of 60° and hat angle of 180° to 120° in 20° decrements for 200 and 700 MHz are plotted in Figure 3.17.

The broadband characteristics of biconical antennas are demonstrated in Figure 3.18 where the input impedances of biconical antennas with conical angles of 30° to 60° in 10° steps and hat angle of 180° are plotted for 40 to 900 MHz. When the hat angle is changed from 180° to 120° in 20° decrements, the input impedances change as shown in Figure 3.19.

For frequencies ranging from 40 MHz to 900 MHz, the antenna factors of biconical antennas with θ_f = 30 to 60° in 10° increments and θ_h=180° are calculated and the results shown in Figure 3.20. As seen in the figure, a change in conical angle has very little effect on the antenna factor curve. For conical angle of θ_f=60°, antenna factor curves are plotted for

hat angles of 180° to 120° in 20° decrements in Figure 3.21. Again, minimal change in antenna factor is observed when the hat angle is changed, especially at high frequencies.

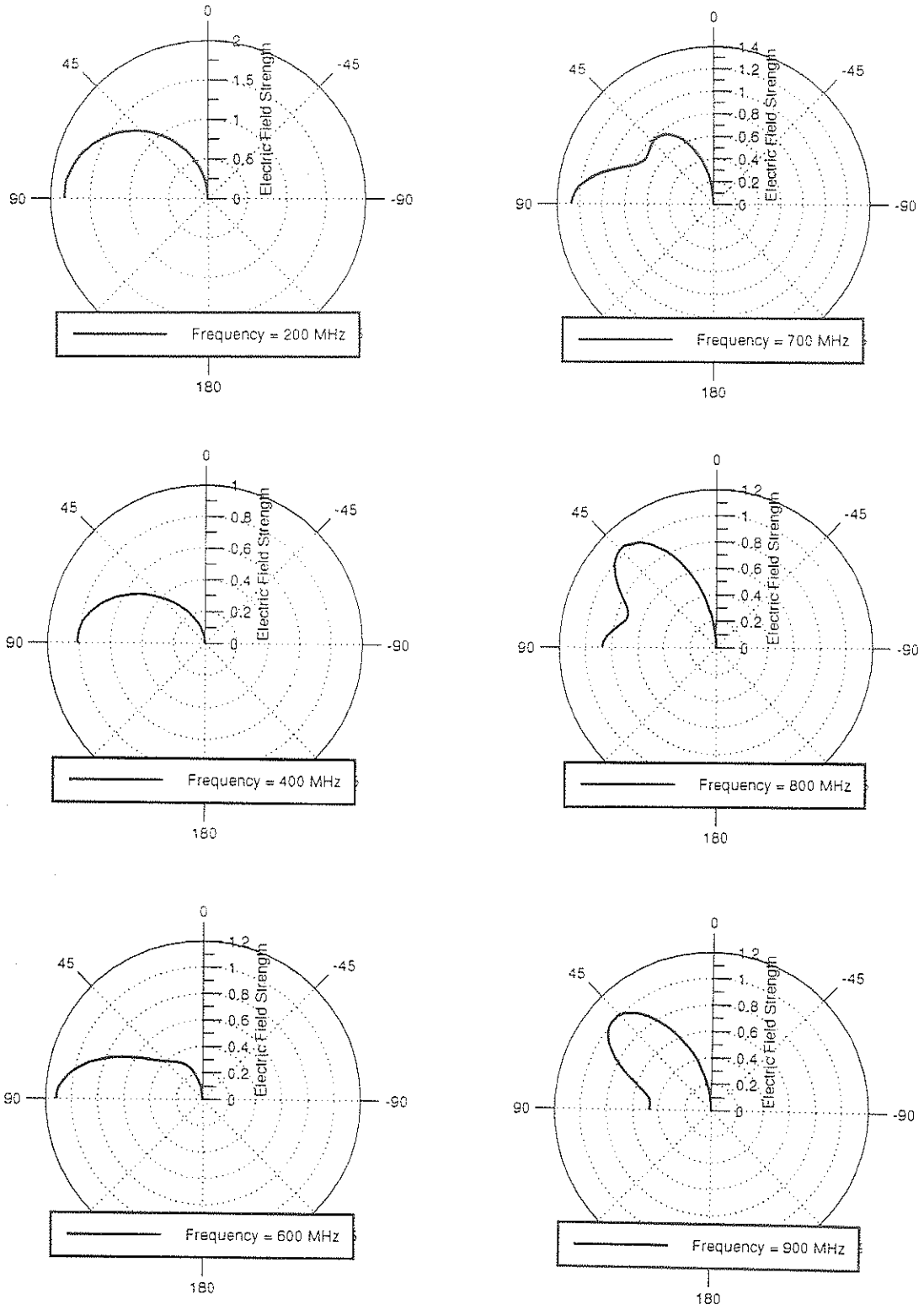

Figure 3.14 Far Electric Field (E_θ) Patterns of a Body-of-Revolution Wire Biconical Antenna with θ_f=30° and θ_h=180° as a Function of Zenith Angle θ for Various Frequencies.

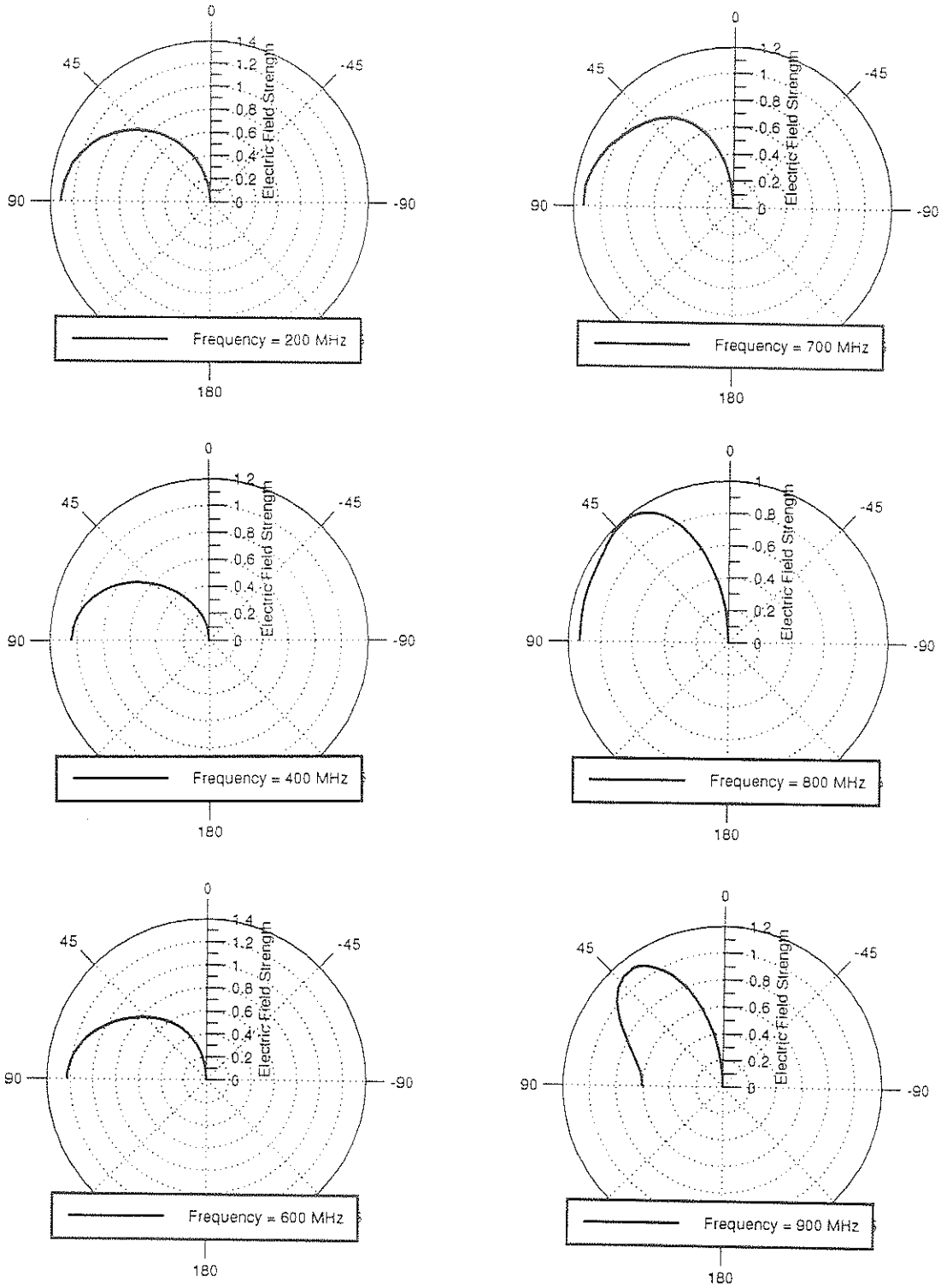

Figure 3.15 Far Electric Field (E_θ) Patterns of a Body-of-Revolution Wire Biconical Antenna with θ_f=60° and θ_h=180° as a Function of Zenith Angle θ for Various Frequencies.

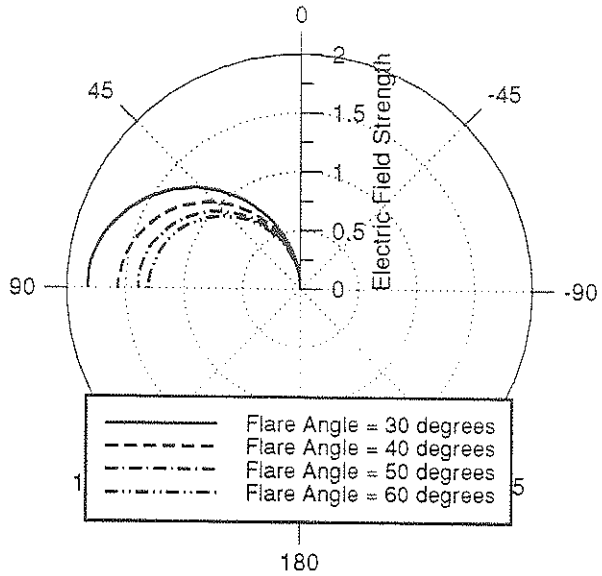

(a)

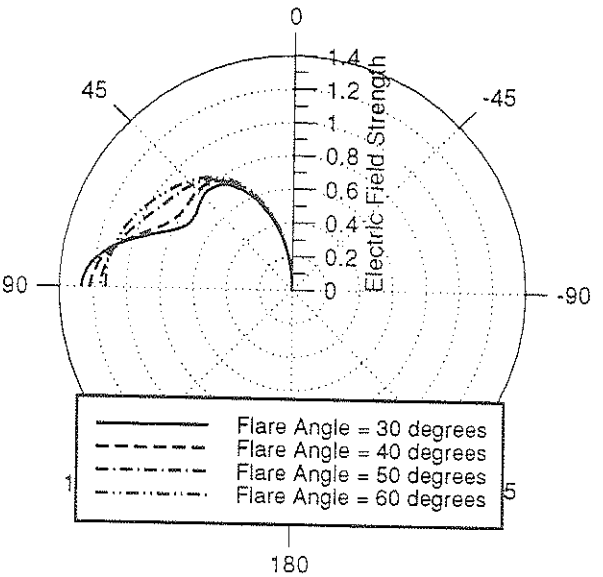

(b)

Figure 3.16 Far Electric Field (E_θ) Patterns of a Body-of-Revolution Wire Biconical Antenna with θ_h=180° and Various θ_f as a Function of Zenith Angle θ for: (a) 200 MHz; and (b) 700 MHz.

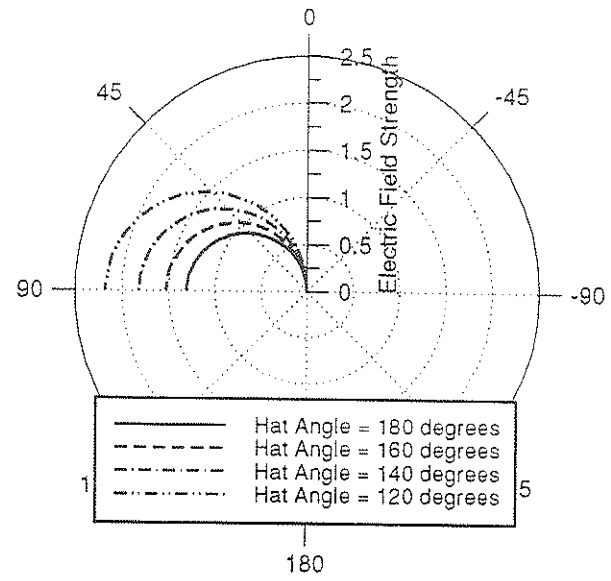

(a)

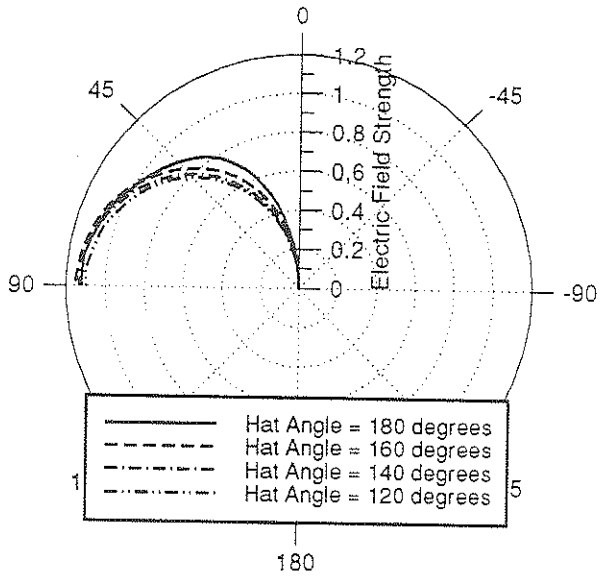

(b)

Figure 3.17 Far Electric Field (E_θ) Patterns of a Body-of-Revolution Wire Biconical Antenna with θ_f=60° and Various θ_h as a Function of Zenith Angle θ for: (a) 200 MHz; and (b) 700 MHz.

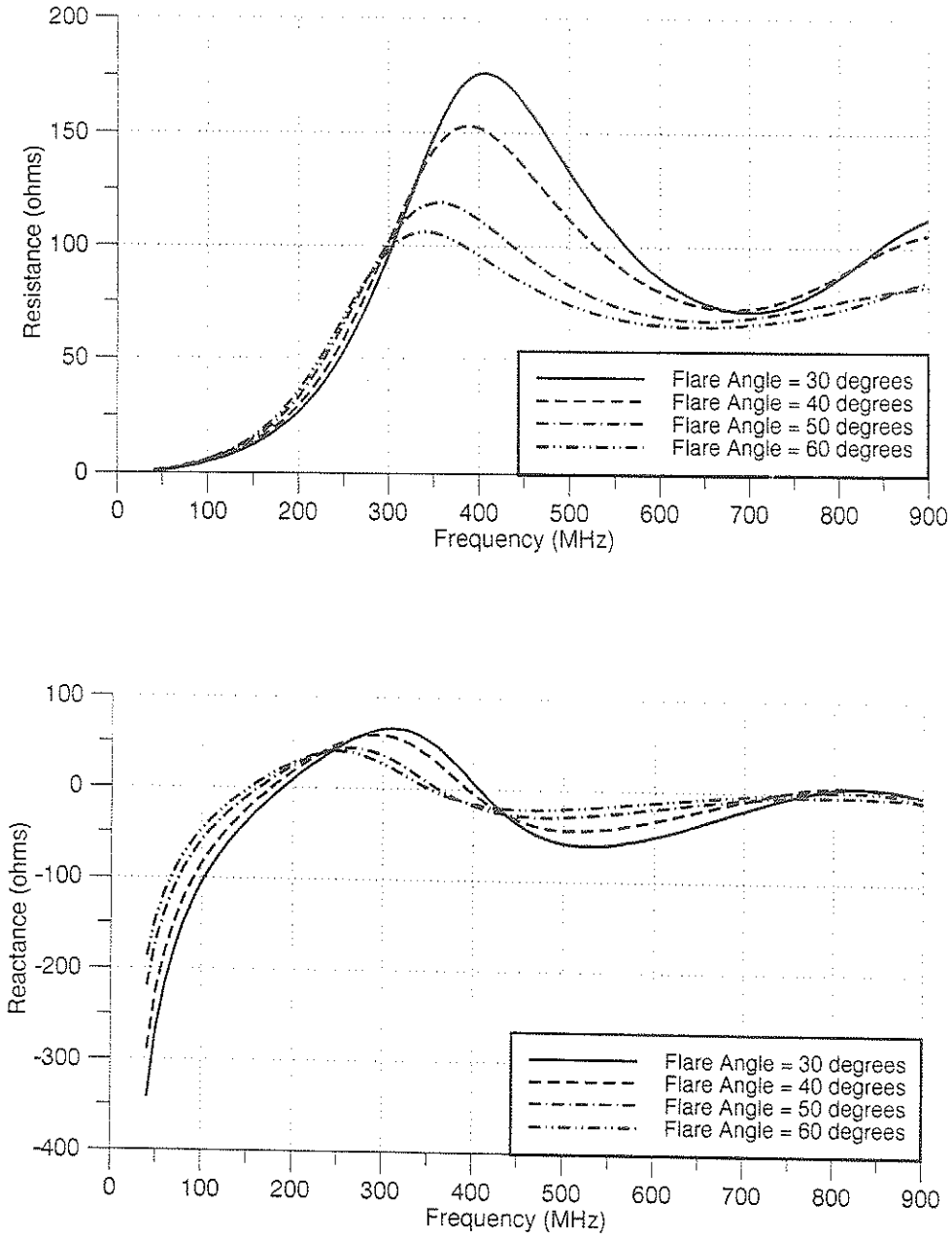

Figure 3.18 Input Impedance Curves of Body-of-Revolution Wire Biconical Antennas with θ_h=180° and Various θ_f.

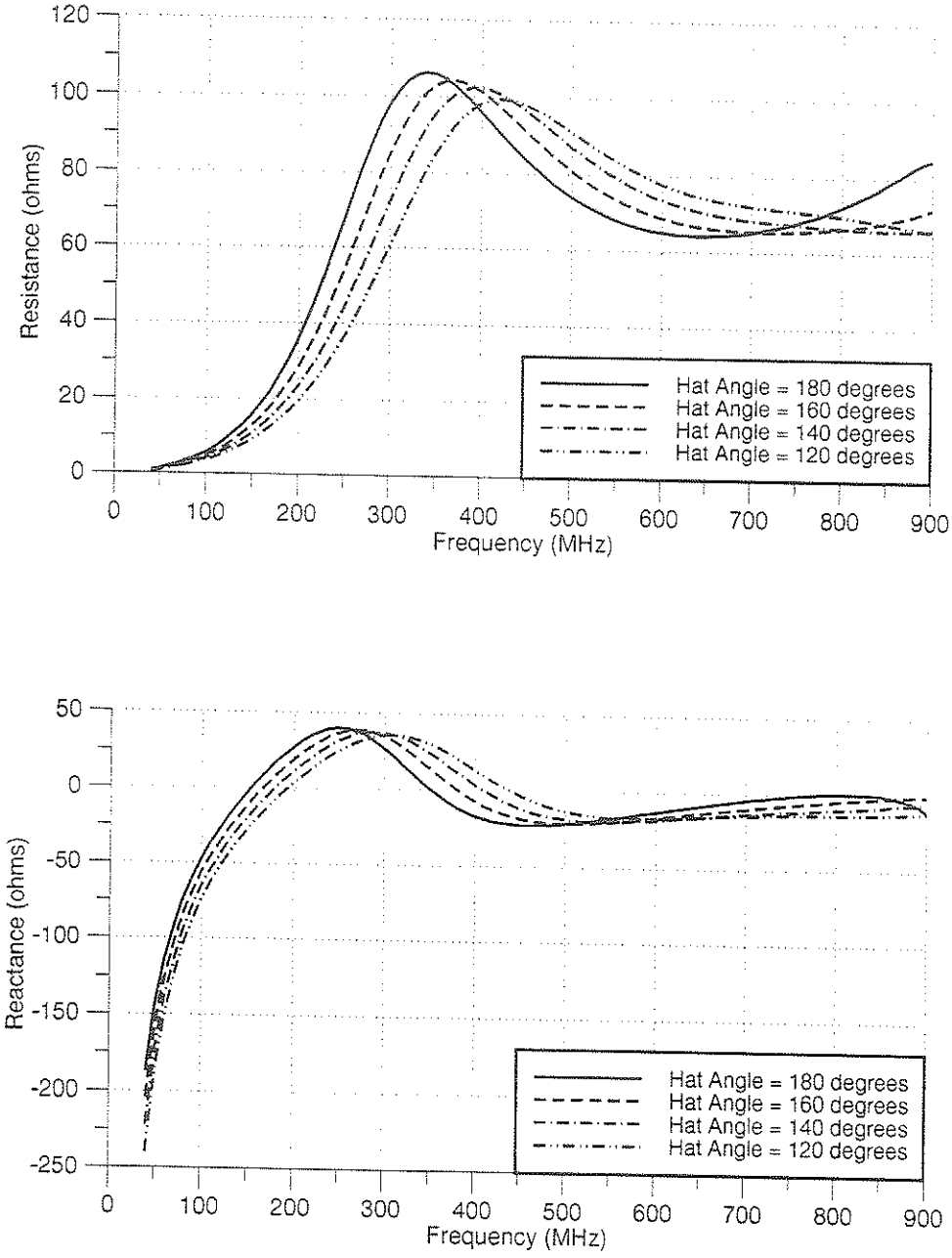

Figure 3.19 Input Impedance Curves of Body-of-Revolution Wire Biconical Antennas with θ_f=60° and Various θ_h.

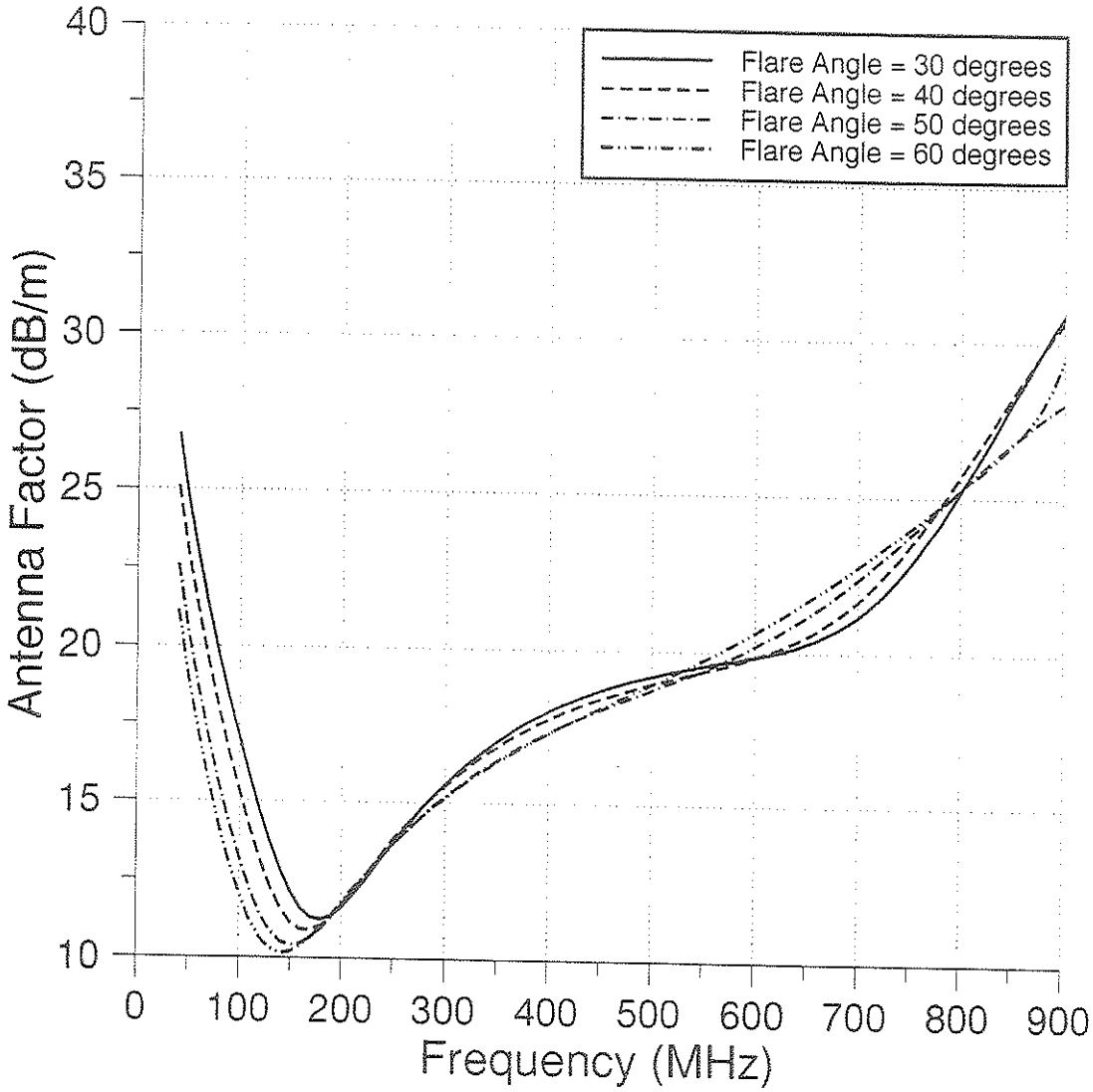

Figure 3.20 Antenna Factor Curves of Body-of-Revolution Wire Biconical Antennas with θ_h=180° and Various θ_f.

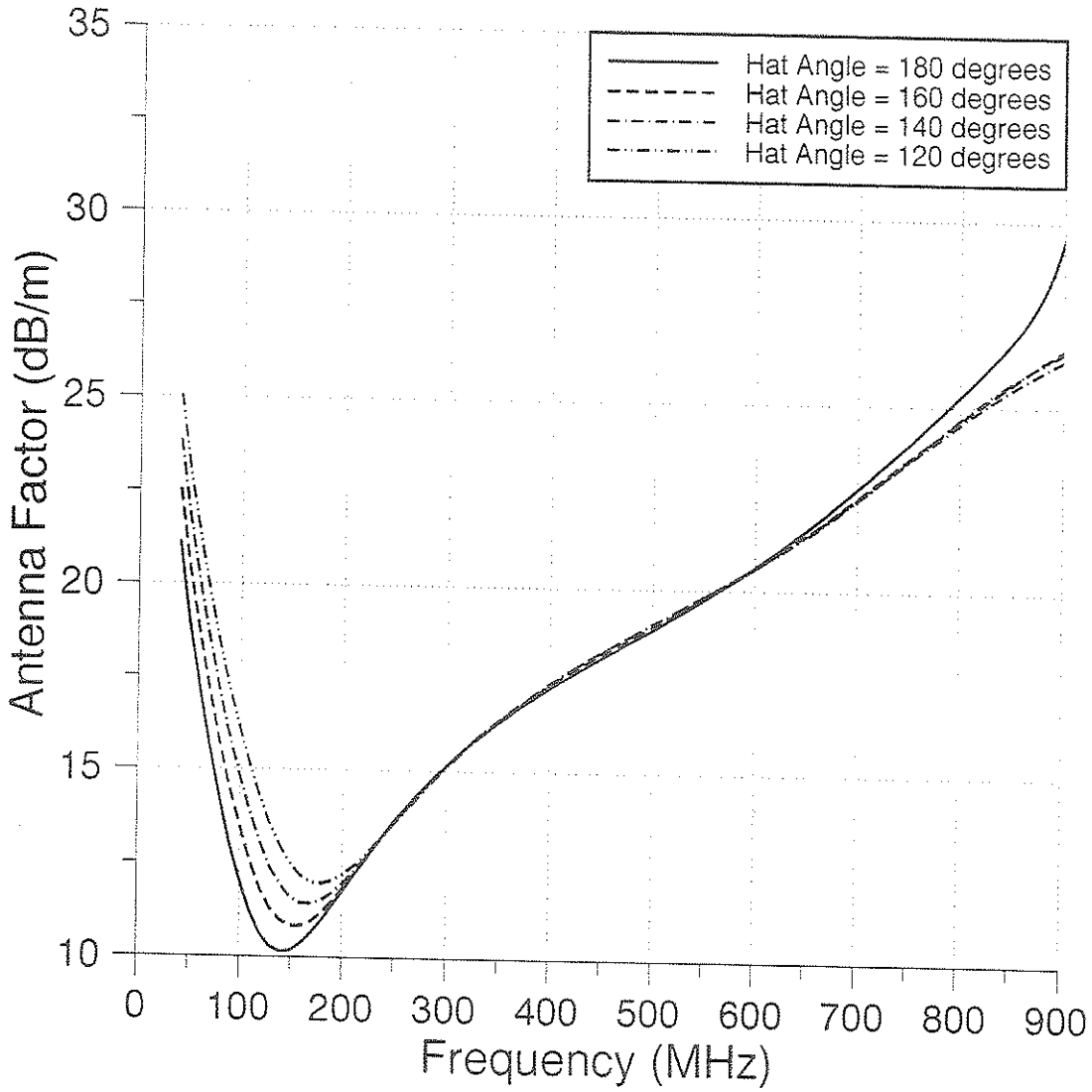

Figure 3.21 Antenna Factor Curves of Body-of-Revolution Wire Biconical Antennas with θ_f=60° and Various θ_h.

3.4 ANTENNA AND CORNER REFLECTOR SYSTEM

Biconical antennas are sometimes used as feed elements for corner reflectors to form broadband reflector antennas. The corner reflector collimates the energy of a biconical antenna in the forward direction where it is sometimes needed most. Because of its light-weight and low wind-resistant construction, the surfaces of the corner reflector are frequently made of grid-wires rather than solid sheet metal. For wires that are parallel to the length of the feed element, as in the case shown in Figure 3.22, the reflectivity of the grid-wire surface is as good as that of a solid surface. In this study, the height of the reflector is taken as 75 cm and the included angle as 45°. A side length of 35 cm is used and the antenna-to-corner spacing is taken as about 32 cm.

The far field (E_θ) patterns of the planar bowtie and corner reflector system shown in Figure 3.22 is compared with the pattern of the bowtie alone for both the $\phi = 90°$ and $\phi = 0°$ planes. In Figures 3.23 and 3.24, respectively, the collimation of energy in the forward direction is clearly shown.(see Figures C-1 and C-2 in Appendix C). The effect of the coupling between the corner reflector and the biconical feed is evident in Figure 3.25 where the input impedance of the reflector antenna is shown. The input impedance of the reflector antenna peaks to almost four times the value of the biconical antenna at around 400 MHz. The antenna factor is also computed for the reflector antenna and the result is shown in Figure 3.26 along with the antenna factor of the biconical antenna. From the figure, we can see that the change in antenna factor is very moderate,

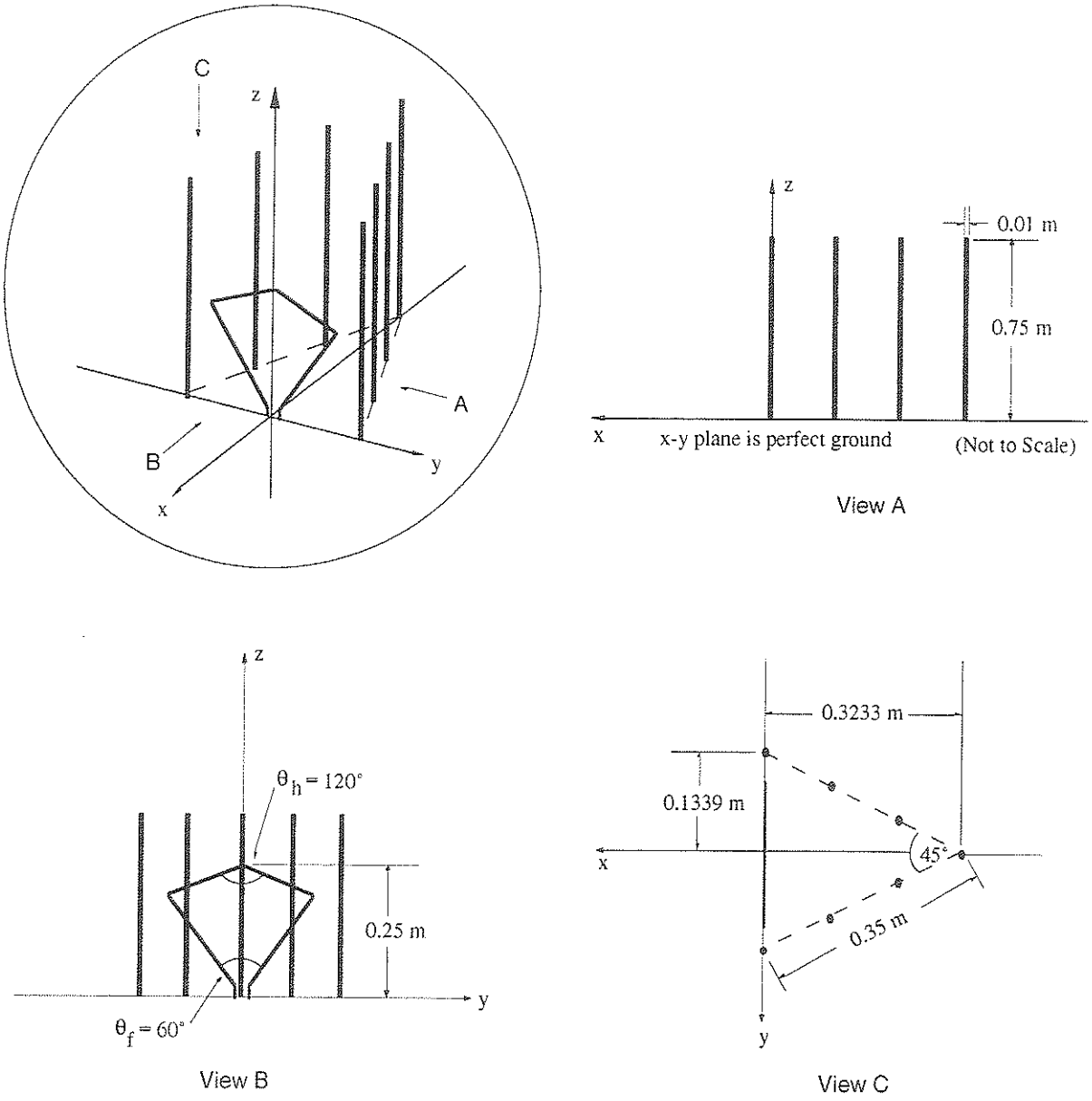

Figure 3.22 Planar Wire Biconical Antenna and Corner Reflector Configuration.

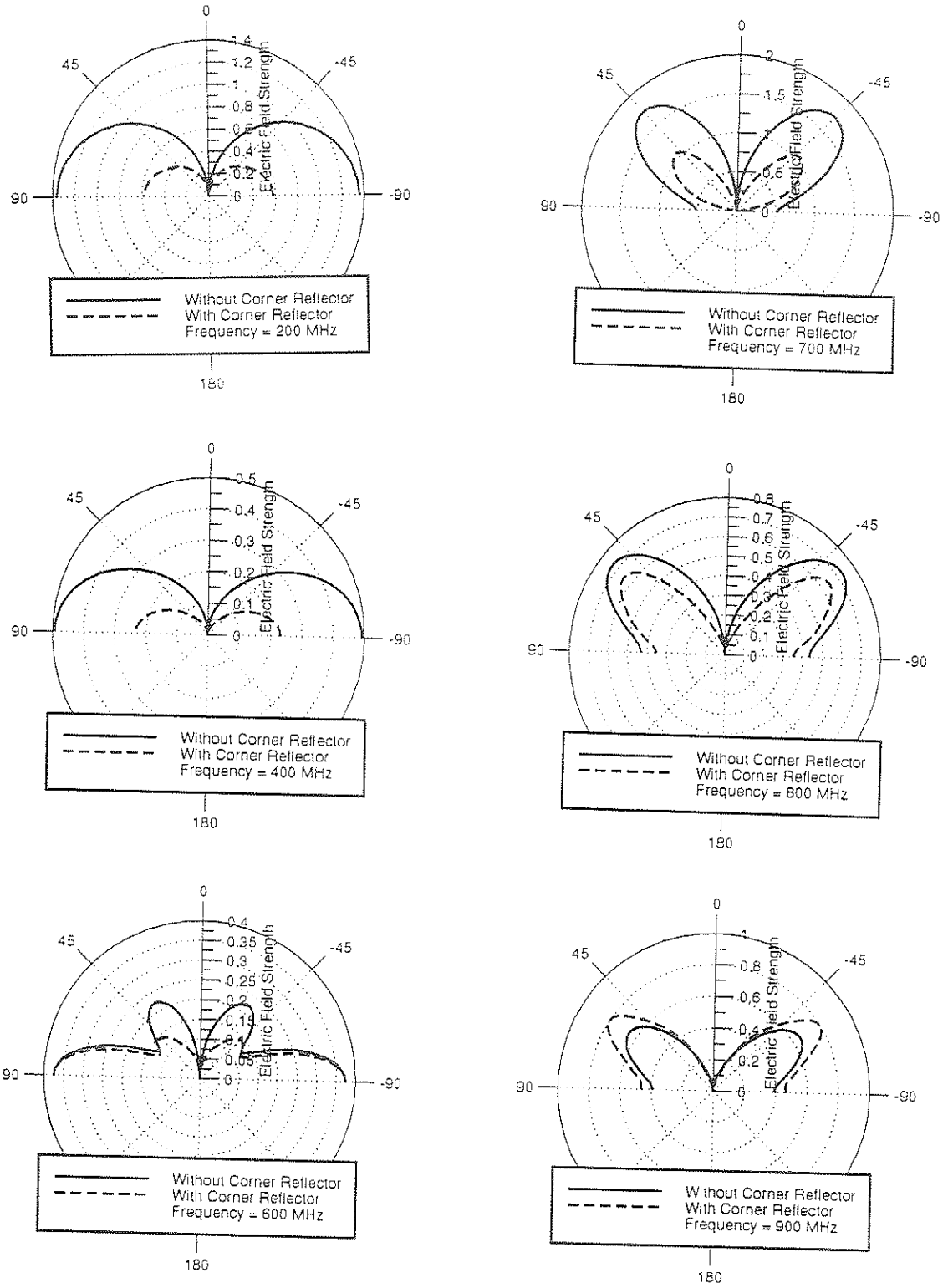

Figure 3.23 Far Electric Field (E_θ) Pattern of a Planar Wire Biconical Antenna with θ_f=60° and θ_h=120° With and Without Corner Reflector as a Function of Zenith Angle θ for the ϕ=90° Plane.

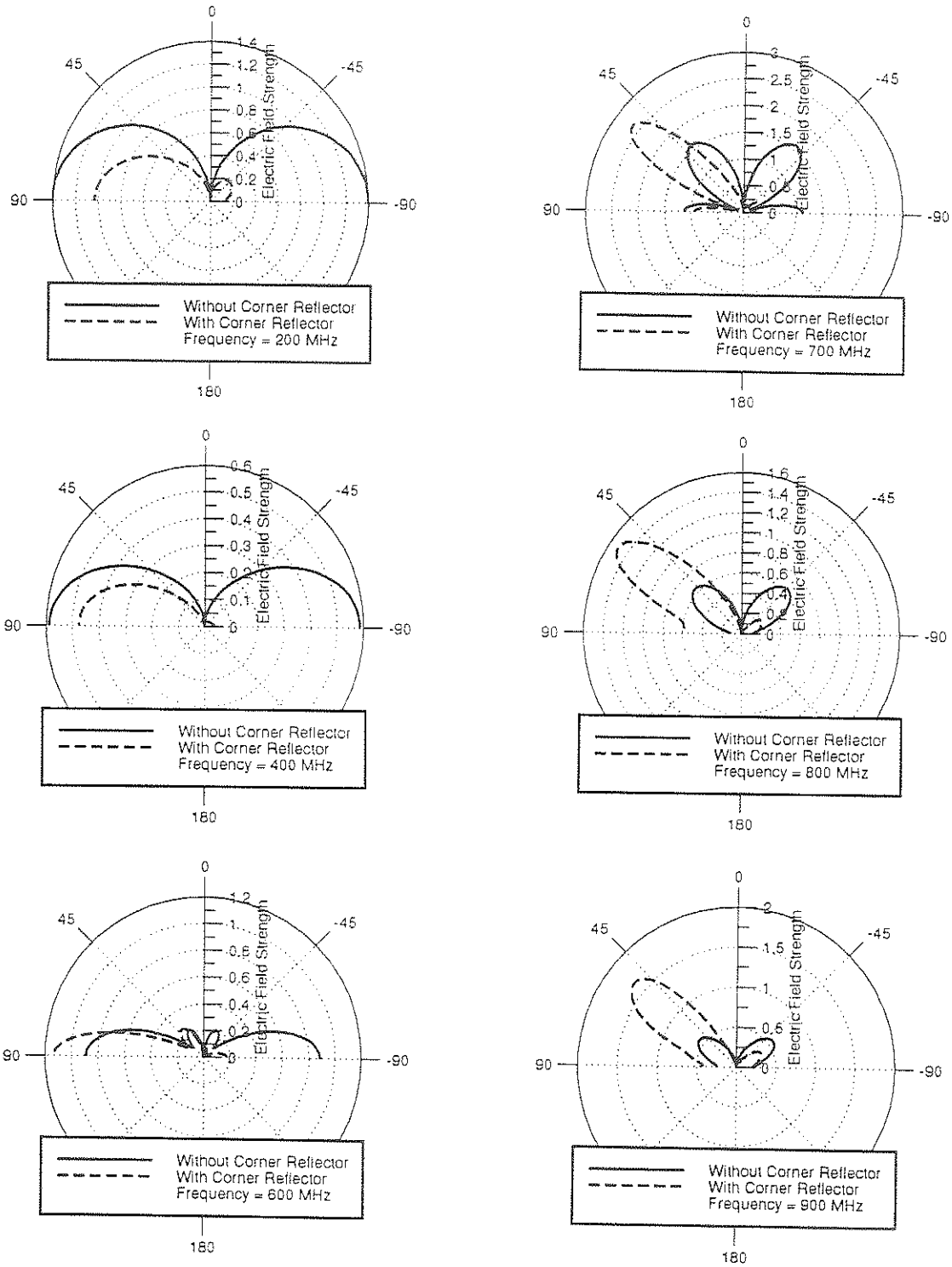

Figure 3.24 Far Electric Field (E_θ) Pattern of a Planar Wire Biconical Antenna with θ_f=60° and θ_h=120° With and Without Corner Reflector as a Function of Zenith Angle θ for the ϕ=0° Plane.

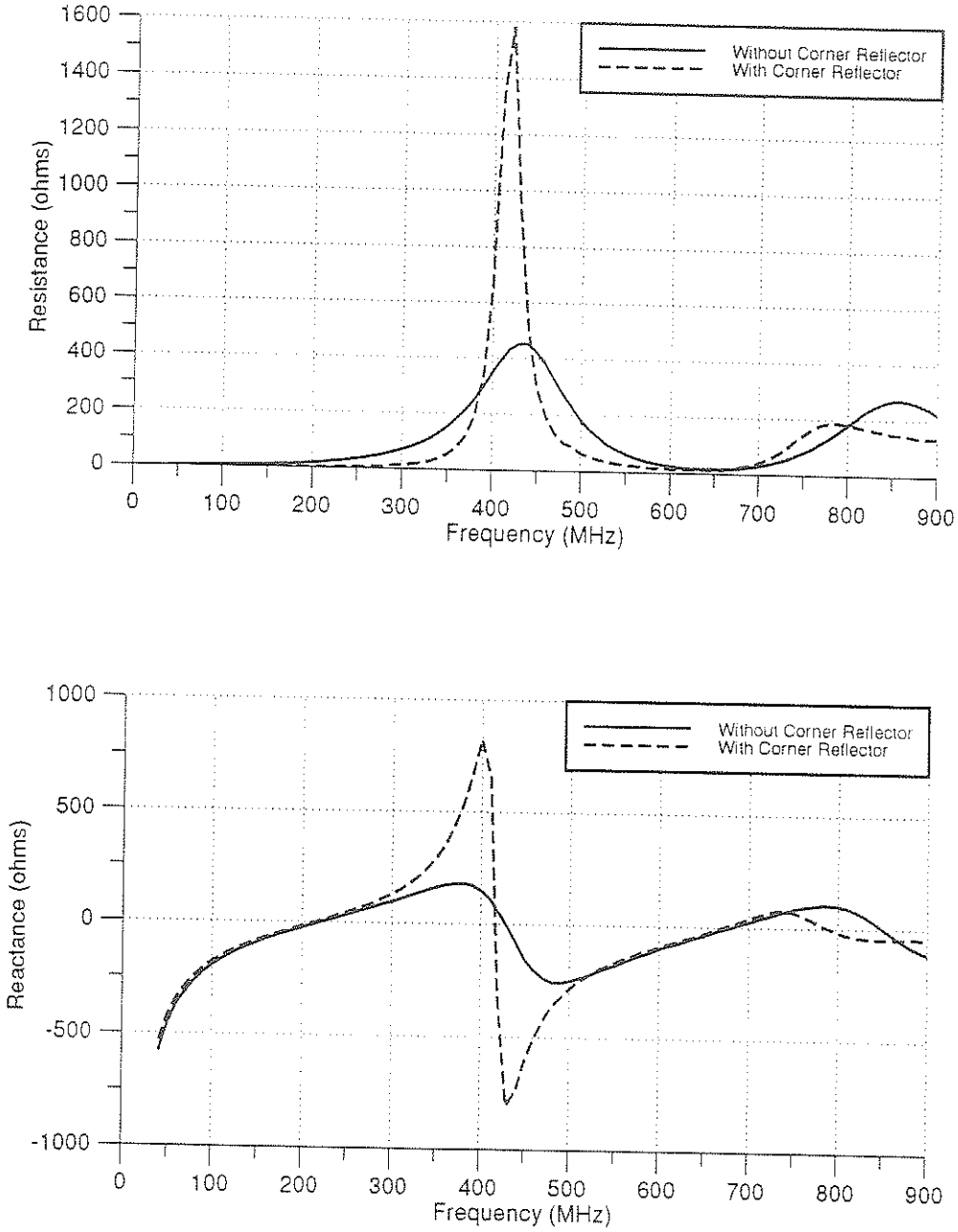

Figure 3.25 Input Impedance Curves of a Planar Wire Biconical Antenna with θ_f=60° and θ_h=120° With and Without Corner Reflector.

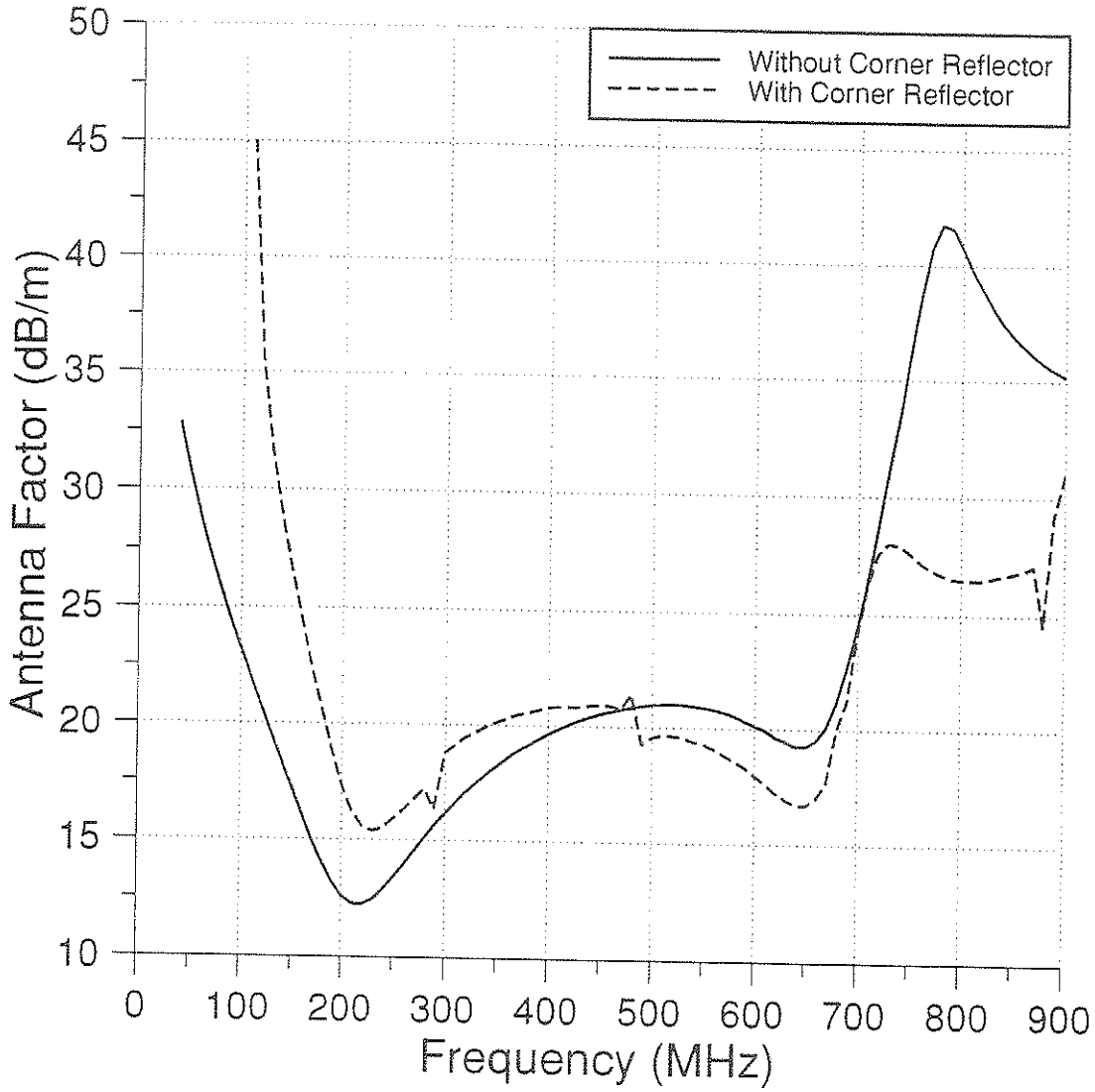

Figure 3.26 Antenna Factor Curves of a Planar Wire Biconical Antenna with θ_f=60° and θ_h=120° With and Without Corner Reflector.

indicating that the antenna factor is insensitive to input impedance changes.

When the planar bowtie is replaced by a body-of-revolution biconical antenna with the same flare and hat angle, the system shown in Figures 3.27 is formed. The far field pattern of this reflector antenna is again computed and the results are shown in Figure 3.28 and 3.29 for the ϕ=90° and ϕ=0° planes respectively (see Figures C-3 and C-4 in Appendix C). The input impedance and antenna factor of the reflector antenna are also obtained. Figure 3.30 shows the input impedance of the reflector antenna as compared with the biconical antenna. The input impedance of the reflector antenna follows very closely to that of the biconical antenna except at around 400 MHz where a "jump" occurs. The antenna factor of the reflector antenna is shown in Figure 3.31. From the figure, it can be seen that, antenna factor wise, the reflector antenna is frequency independent from 200 to 600 MHz. In order to further investigate this broadband phenomena, two modifications of the corner reflector as shown in Figure 3.32 have been adopted. The antenna factor curves of the modified reflector antennas are shown in Figure 3.33. It is noticed that by changing the side length of the corner reflector, still better antenna factor characteristics can be achieved. This suggests that an optimal corner reflector side length exists for our model and is between 23 and 35 cm.

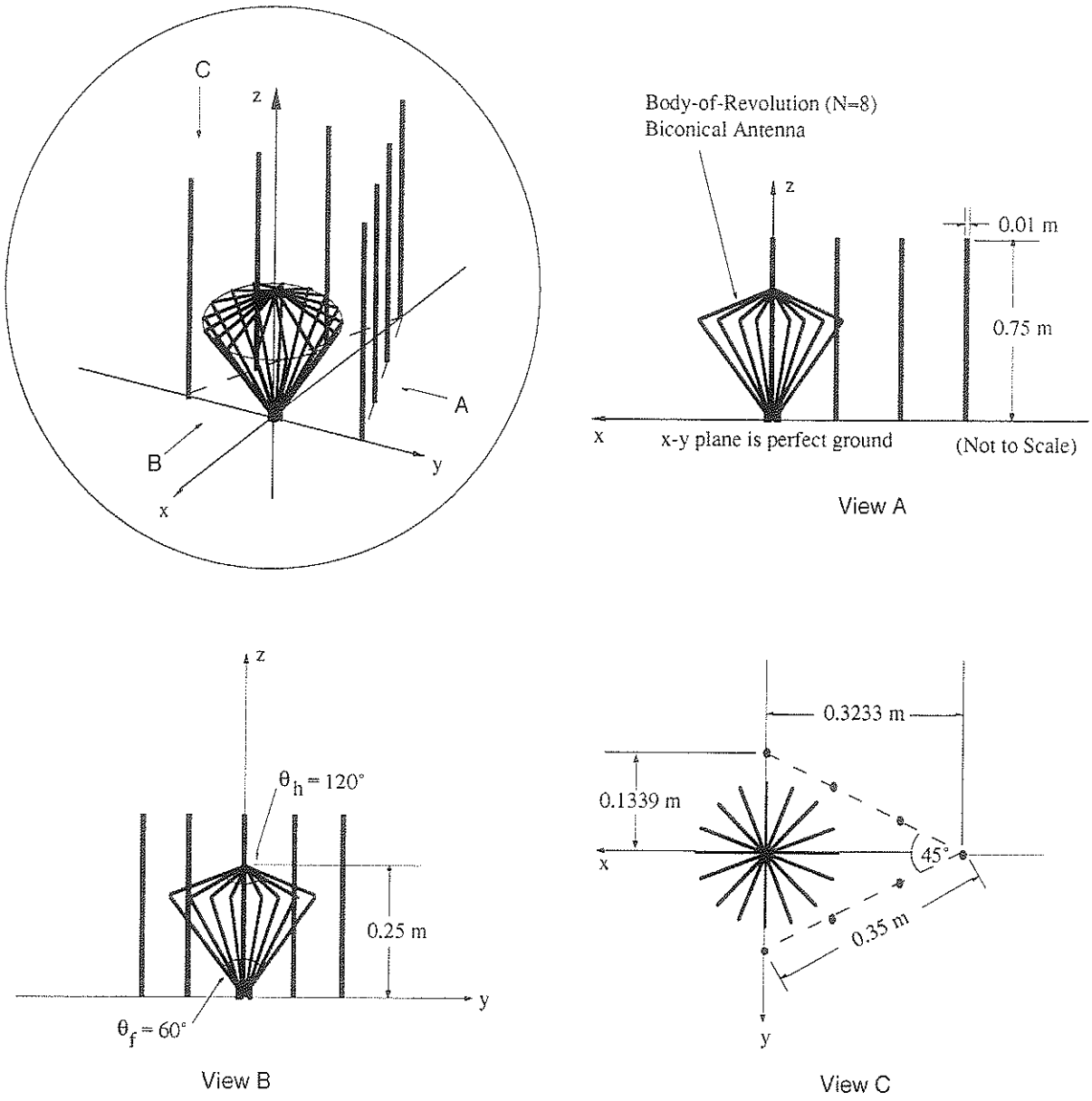

Figure 3.27 Body-of-Revolution Wire Biconical Antenna and Corner Reflector Configuration.

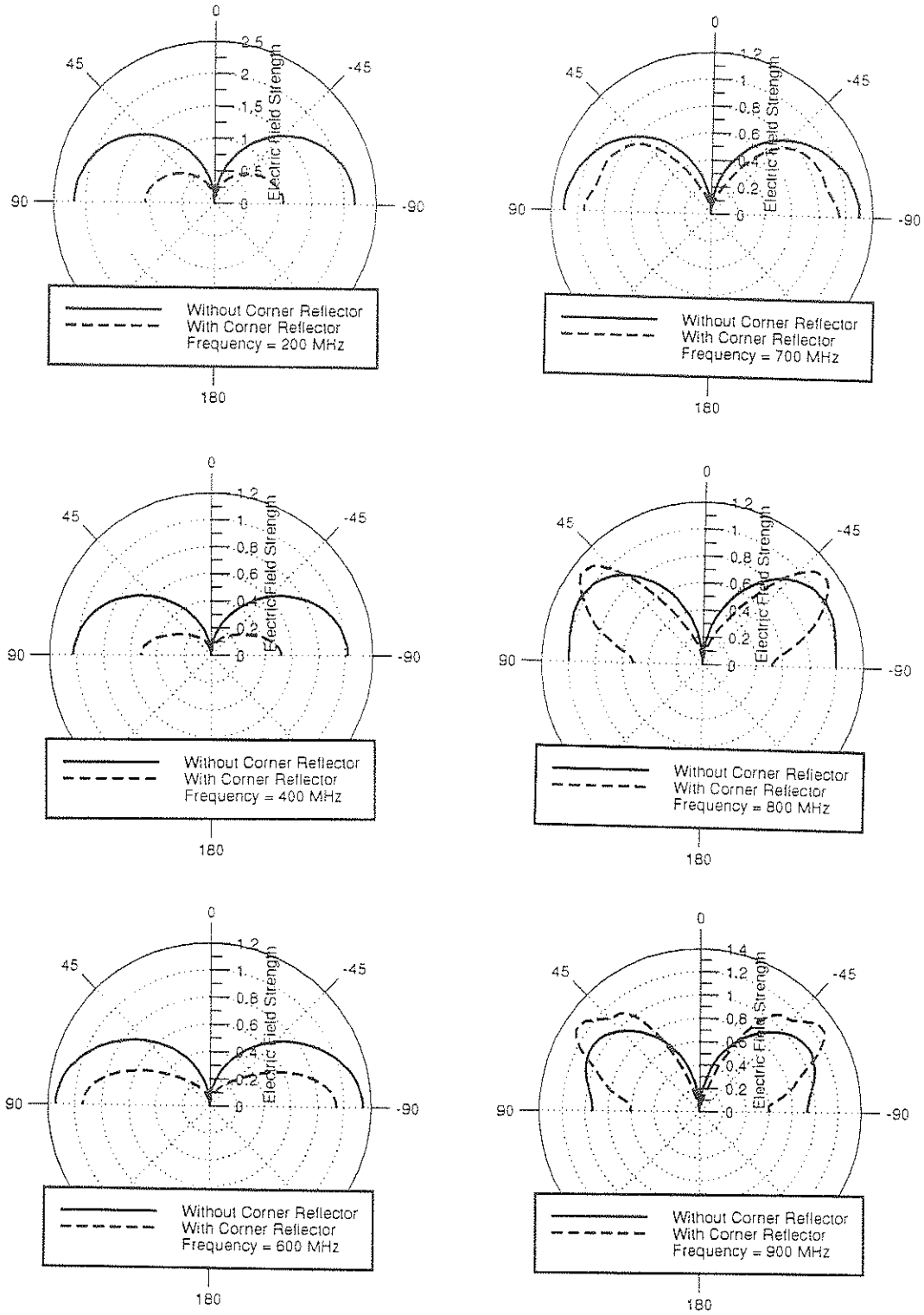

Figure 3.28 Far Electric Field (E_θ) Patterns of a Body-of-Revolution Wire Biconical Antenna with θ_f=60° and θ_h=120° With and Without Corner Reflector as a Function of Zenith Angle θ for the ϕ=90° Plane.

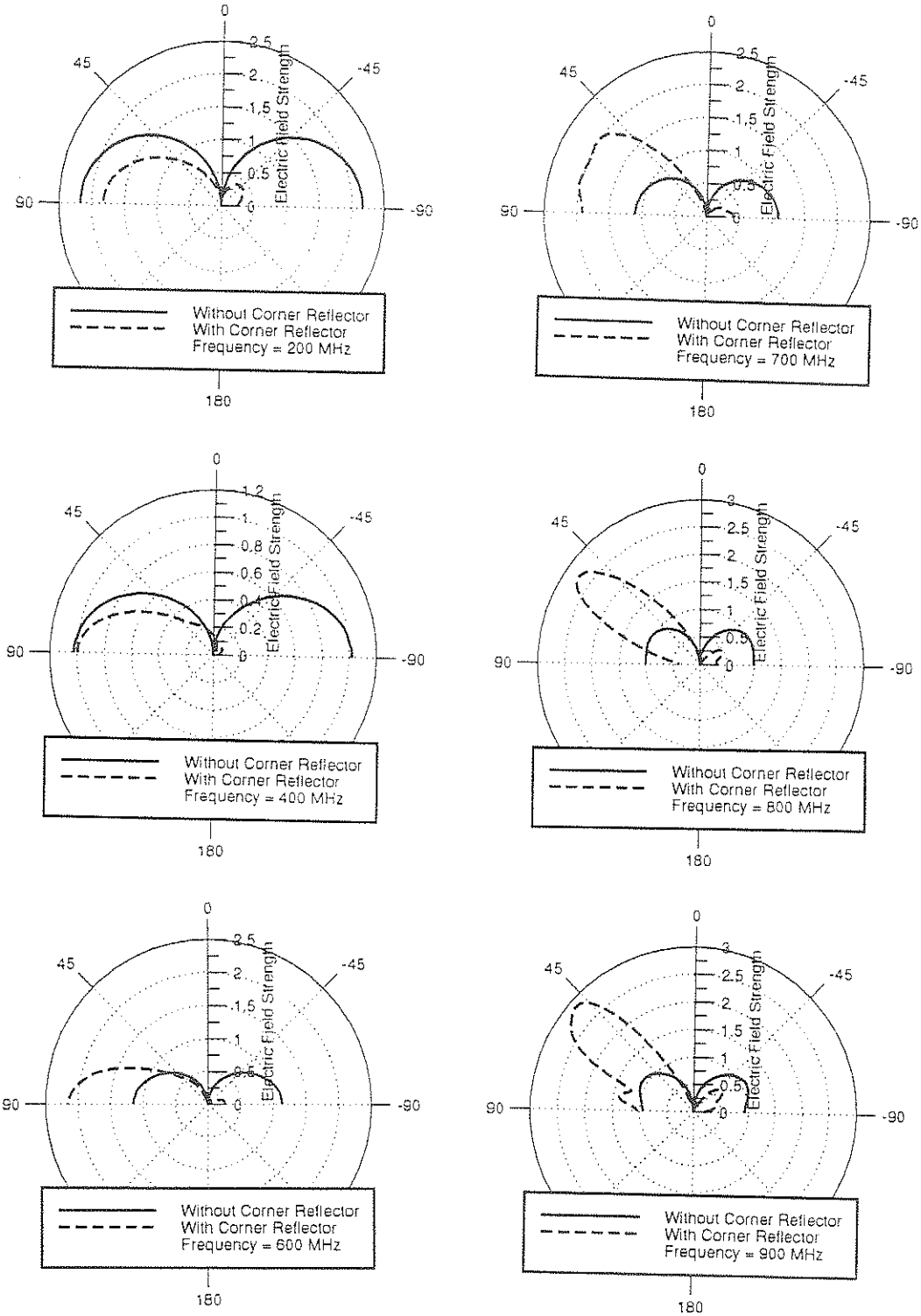

Figure 3.29 Far Electric Field (E_θ) Patterns of a Body-of-Revolution Wire Biconical Antenna with θ_f=60° and θ_h=120° With and Without Corner Reflector as a Function of Zenith Angle θ for the ϕ=0° Plane.

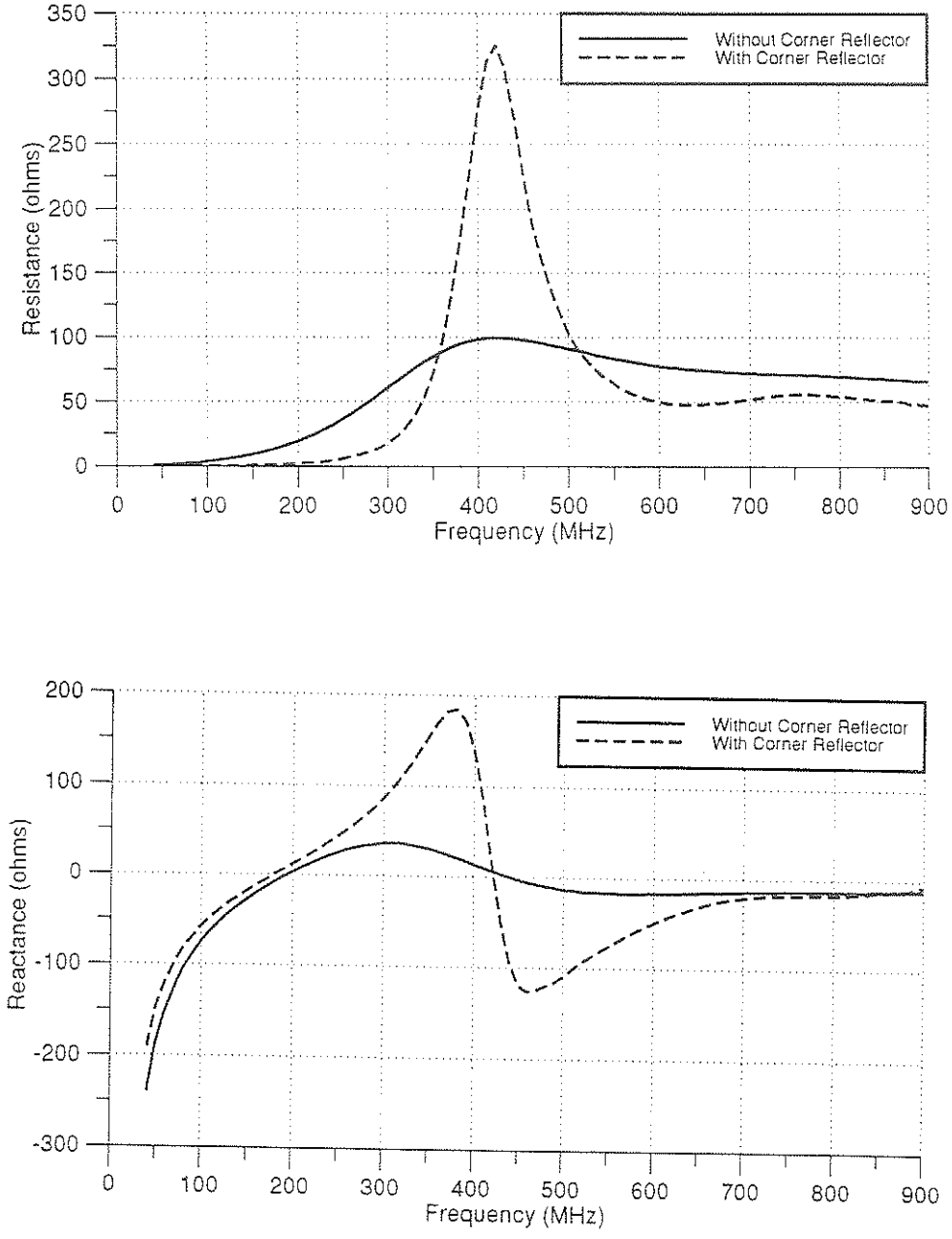

Figure 3.30 Input Impedance Curves of a Body-of-Revolution Wire Biconical Antenna with θ_f=60° and θ_h=120° With and Without Corner Reflector.

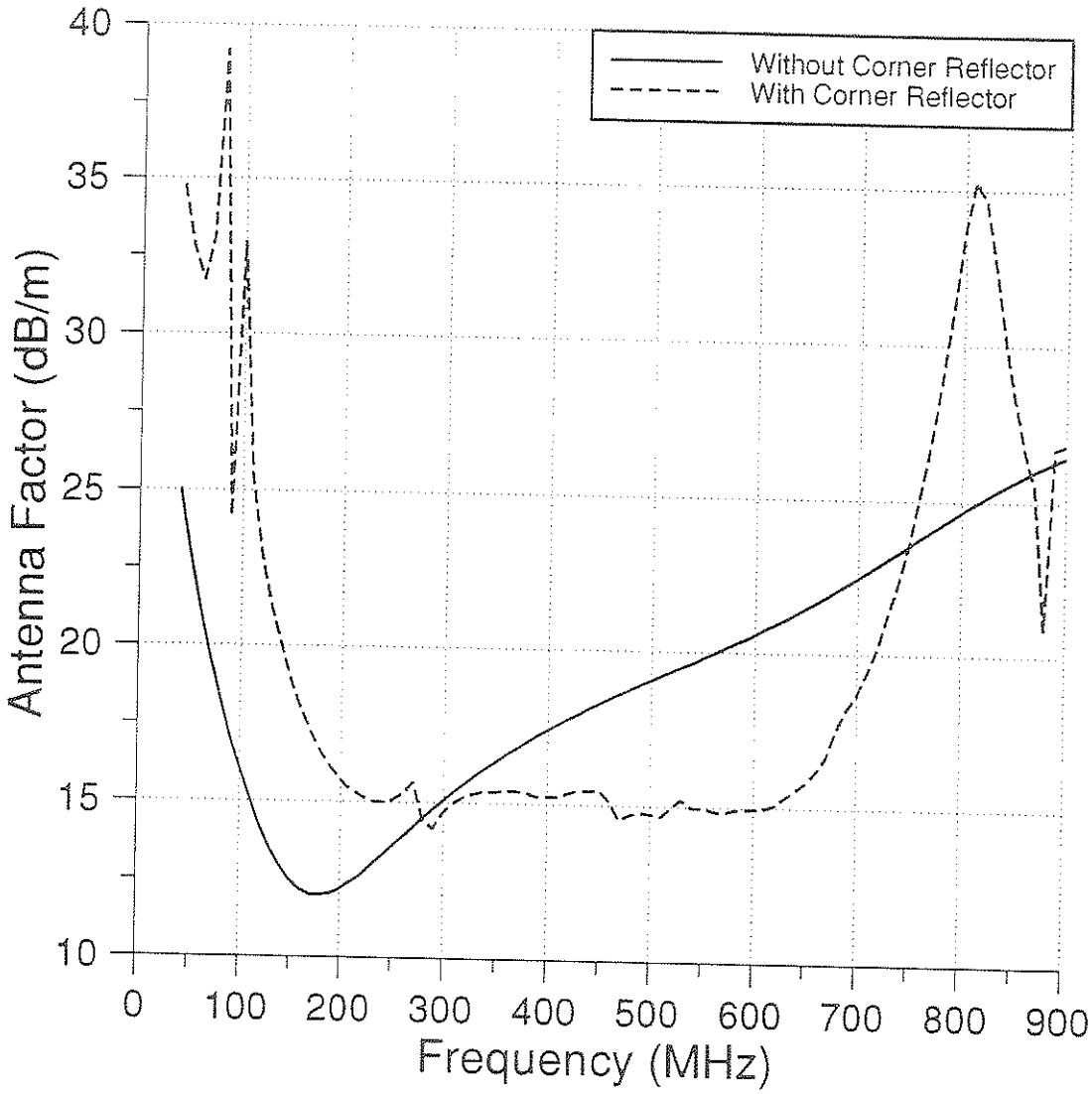

Figure 3.31 Antenna Factor Curves of a Body-of-Revolution Wire Biconical Antenna with θ_f=60° and θ_h=120° With and Without Corner Reflector.

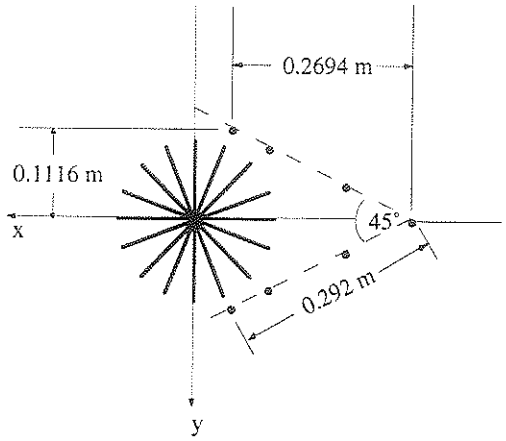

(a)

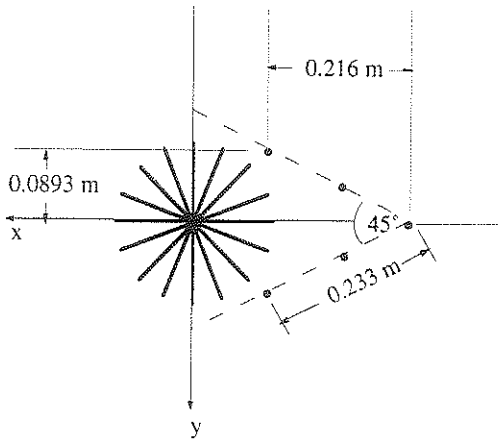

(b)

Figure 3.32 Configuration of Body-of-Revolution Wire Biconical Antenna with Corner Reflector of: (a) Side Length = 29.2 cm; and (b) Side Length = 23.3 cm.

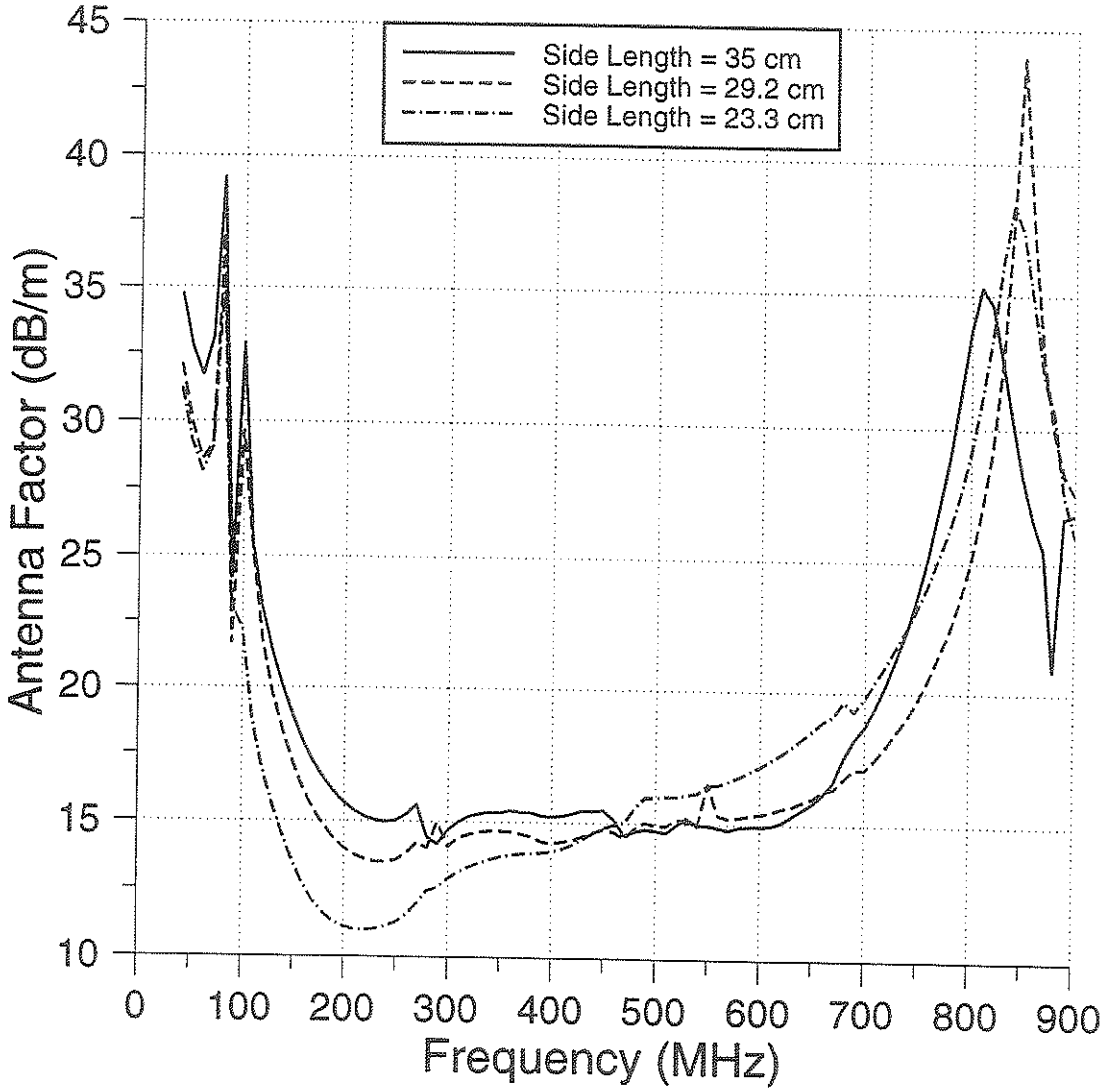

Figure 3.33 Antenna Factor Curves of a Body-of-Revolution Wire Biconical Antenna with θ_f=60°, θ_h=120°, and Corner Reflectors of Different Side Lengths.

CHAPTER IV

OPTIMIZATION OF WIRE BICONICAL ANTENNAS

4.1 INTRODUCTION

The main idea behind the development of wire biconical antennas is to construct a mechanically realistic antenna which retains as much of the desired electrical features of a solid or shell biconical structure as possible. So far, from the results presented in the previous chapter, we can see that the body-of-revolution model of the wire biconical antenna is quite satisfactory in such domain. However, the planar model of the biconical antenna, while possessing all the mechanical advantages, lacks the desired electrical features of a broadband antenna. It is, consequently, the purpose of this chapter to attempt to enhance the electrical characteristics of a planar wire biconical antenna without sacrificing its mechanical supremacy. Section 4.2 discusses some of the preliminary optimization efforts. Since biconical antennas made out of sheet metals performs better than the wire frame ones, the idea behind section 4.2.1 is to simulate a sheet metal with the addition of a few wire fragments inside the wire frame. Another improvement in the optimized model in section 4.2.1 is the addition of resistive loads to the junction of the wire fragments in the middle of the antenna. This option is explored in section 4.2.2 where various resistive loads are imposed onto the antenna. Optimization is also

sought by a change in antenna shape. In section 4.3, the original wire biconical antenna is changed into a "double-bicone" by offsetting the source segments. The change in feed position change the antenna's characteristics and moderate improvement is achieved at selected frequencies. The use of parasitic elements also changes the performance of a wire antenna and this is shown in section 4.3.2. Finally, in section 4.4, the biconical antenna with sleeve set-up is examined and is found to be most useful in the optimization of the wire antenna.

4.2 PRELIMINARY OPTIMIZATION METHODS

4.2.1 Biconical Antenna with Cross

Planar wire biconical antennas are quite narrow-band when compared with sheet biconical antennas. However, in applications where both low wind resistance and light-weight is required, wire biconical antennas are still preferred. It is, therefore, feasible to simulate a sheet biconical antenna with wire segments. Although wire grid modeling methods can be used for the purpose, this study will not deal with specific grid size or wire spacing that revolves around grid modeling but instead uses a more intuitive approach. The modified antenna is basically a planar wire biconical antenna with five extra wire fragments forming a "cross" inside. Since two source segments have been used in the modeling, it takes five wire elements to interconnect the inner portion of the antenna. The additional wires has the same radius (i.e., 0.5 mm) as the original antenna structure which has the same source arrangement as before. This modified antenna is shown in Figure 4.1. In this study, the electrical properties of a planar wire bicone with cross (BWC) antenna identified by, respectively, flare and hat angle of 60° and 120° is compared to that of the original antenna.

Figure 4.2 and 4.3 depict the far field patterns of the antenna as a function of zenith angle θ for the $\phi = 90°$ and $\phi = 0°$ planes at different

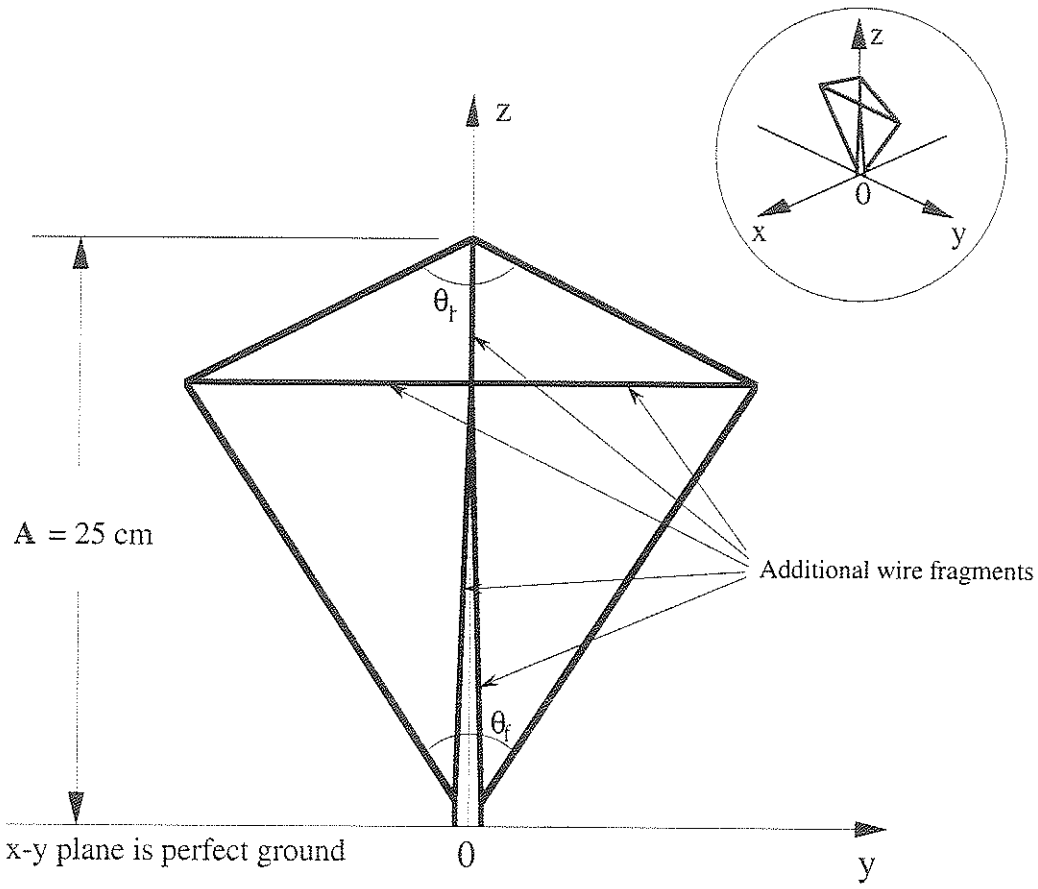

Figure 4.1 Planar Wire Biconical Antenna with Cross.

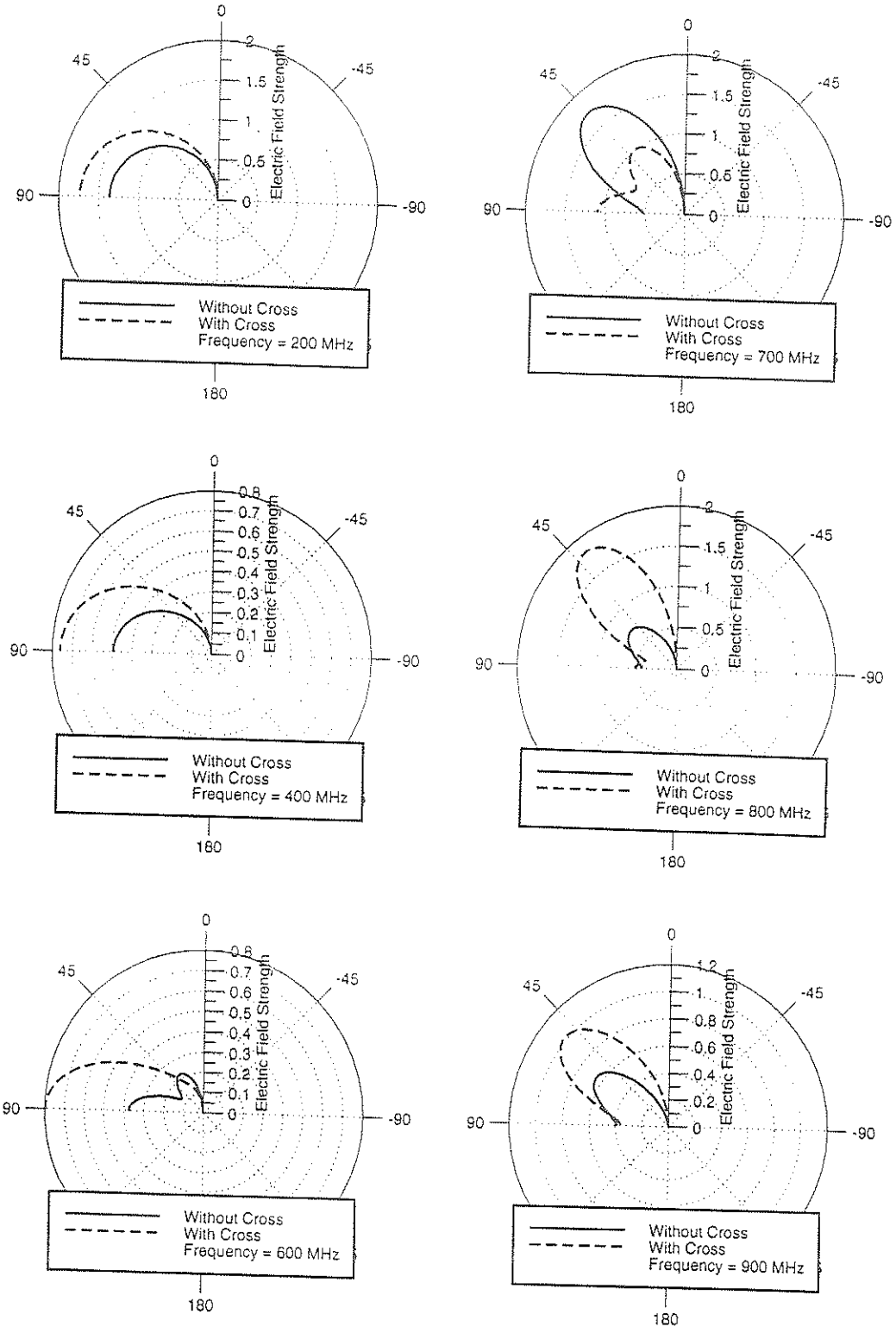

Figure 4.2 Far Electric Field (E_θ) Patterns of a BWC Antenna with θ_f=60° and θ_h=120° as a Function of Zenith Angle θ for Various Frequencies and ϕ=90°.

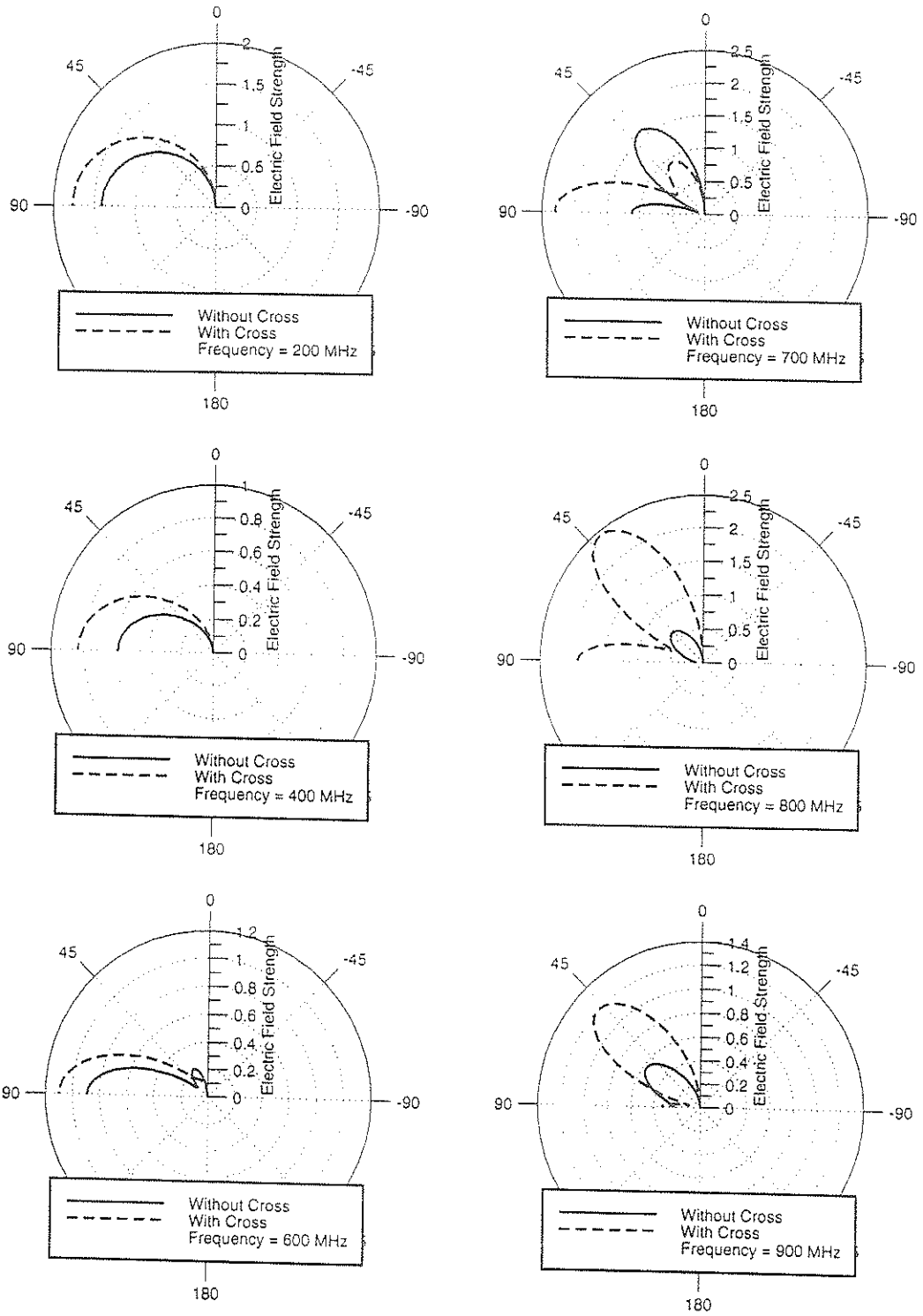

Figure 4.3 Far Electric Field (E_θ) Patterns of a BWC Antenna with θ_f=60° and θ_h=120° as a Function of Zenith Angle θ for Various Frequencies and ϕ=0°.

frequencies, respectively. It is observed that the added segments cause a change in pattern especially at intermediate frequencies.

The impedance characteristics of the BWC antenna are shown in Figure 4.4. From the figure, we can see that the variation in impedance has decreased, and a better match to the source is obtained. With a better match, the mismatch factor of the antenna is improved as shown in Figure 4.5. The discontinuity in the impedance curve at around 750 MHz is caused by the current reflected from the center junction of the antenna which forms a standing wave. This situation can be remedied by loading the junction with resistive loadings as suggested in the next section.

Optimization can be seen in Figure 4.5 where the power gain and the mismatch factor of the BWC antenna are compared with the original planar bicone. The change in power gain is quite significant considered the temperate change that we have incorporated. As aforementioned, the BWC antenna matches better to the source and hence caused lower mismatch losses than the original bowtie antenna. The change in power gain and mismatch factor decreases the antenna factor of the BWC antenna as shown in Figure 4.6. It is noted that the antenna factor of the BWC antenna is significantly better than the original antenna especially in the high frequency end.

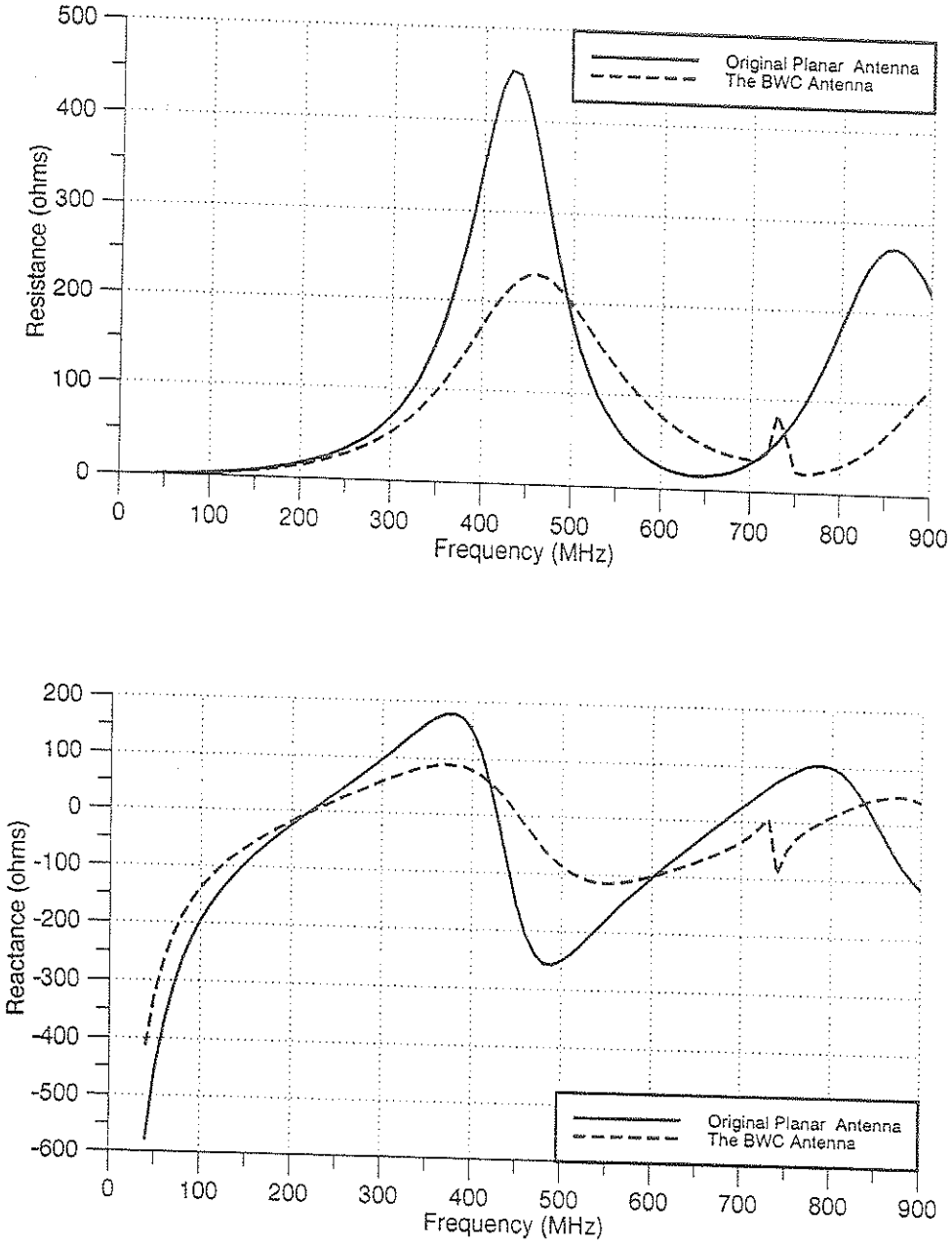

Figure 4.4 Input Impedance Curves of a BWC Antenna with θ_f=60° and θ_h=120° Compared with those of the Original Bowtie Antenna.

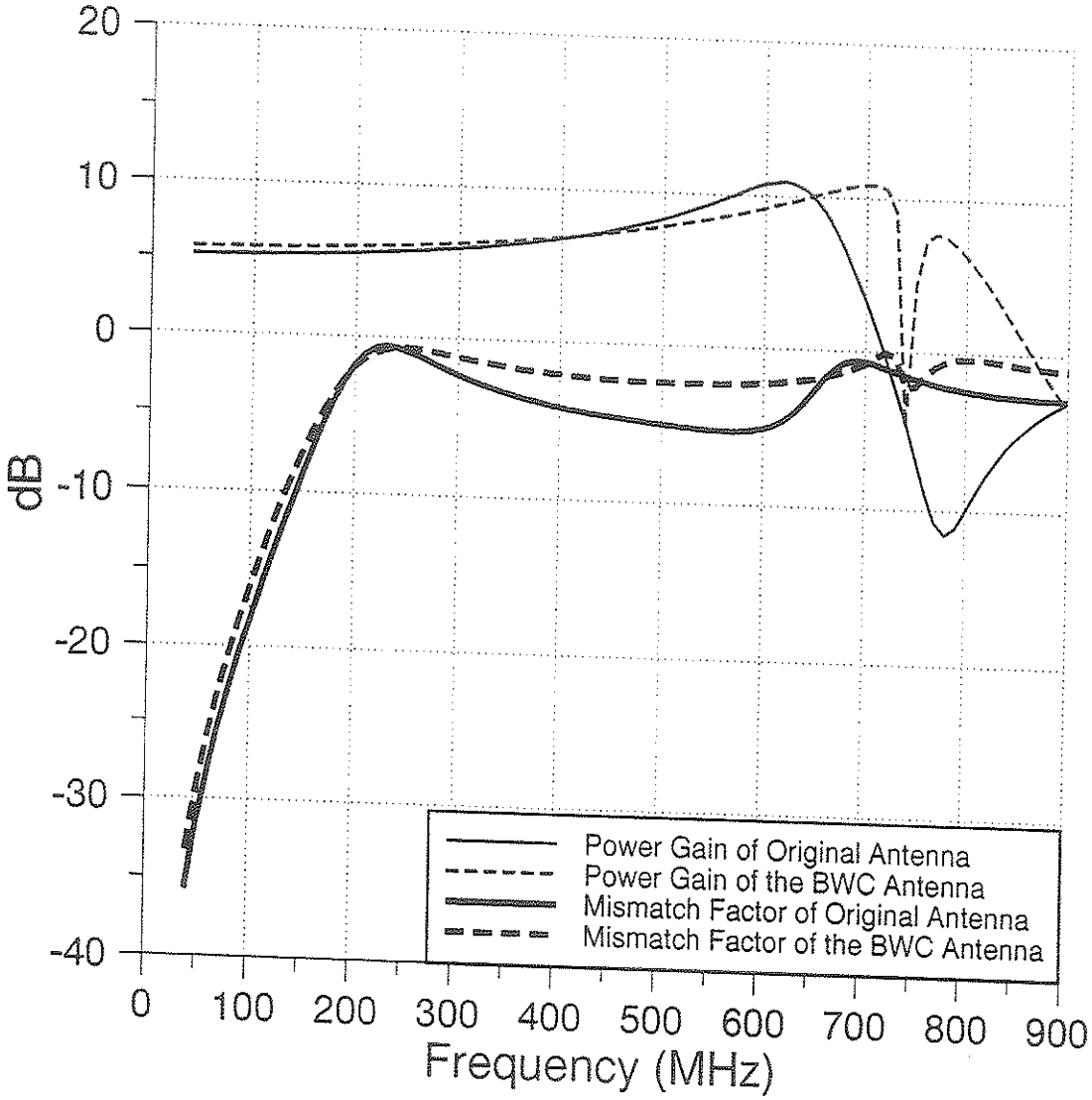

Figure 4.5 Power Gain and Mismatch Factor Curves of a BWC Antenna with θ_f=60° and θ_h=120° Compared with those of the Original Bowtie Antenna.

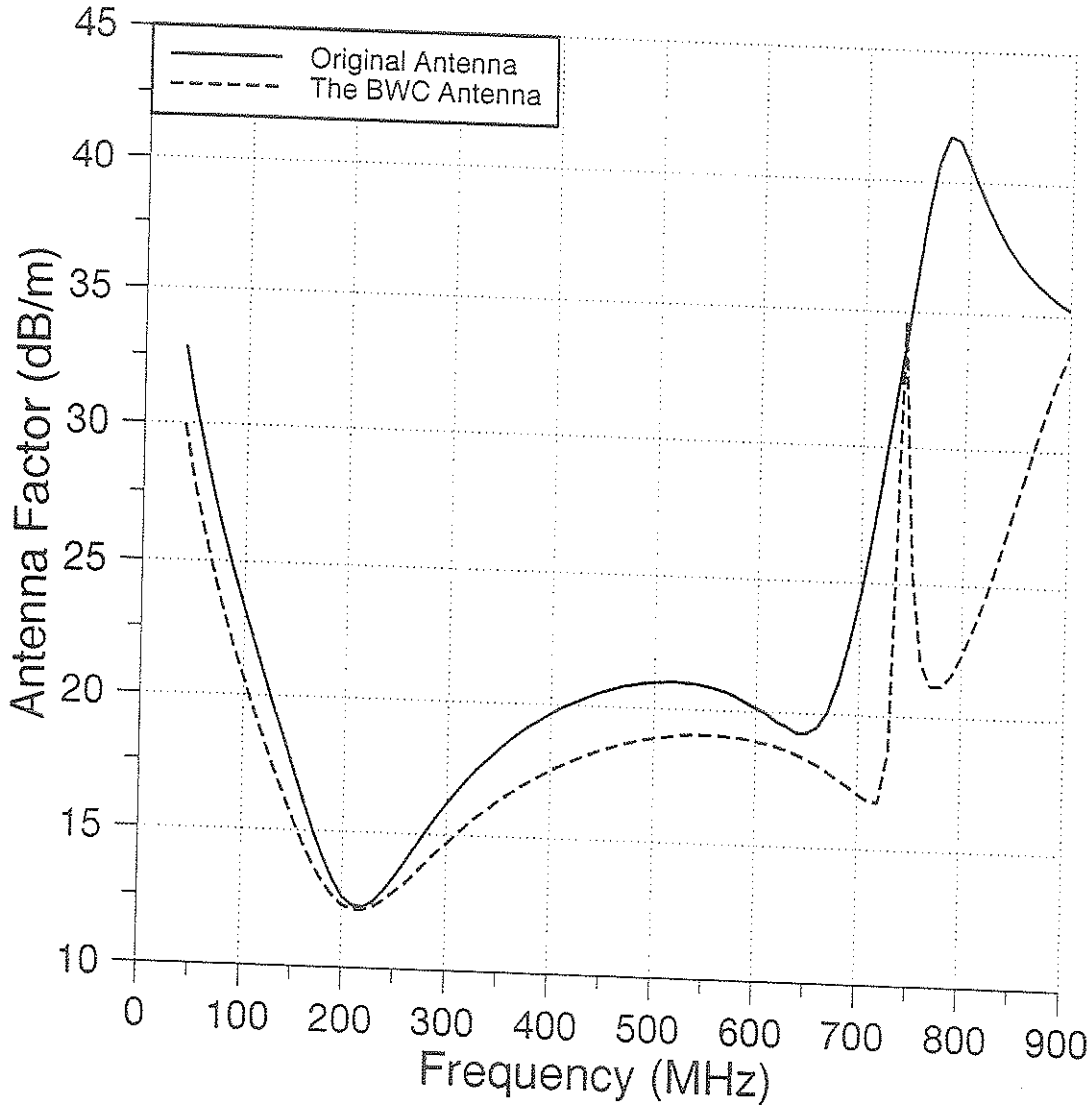

Figure 4.6 Antenna Factor Curve of a BWC Antenna with θ_f=60° and θ_h=120° Compared with that of the Original Bowtie Antenna.

4.2.2 Biconical Antenna with Cross and Resistive Loadings

The performance of the BWC antenna in section 4.2.1 can be further improved by adding impedance loadings to the middle junction (see Figure 4.7). The loading is added to modify the current distribution of the antenna in such a way that reflections from the junction can be lessened. With the decrease in reflections, the discontinuities in the characteristics of the antenna will hopefully be reduced. Generally, there are four loading schemes for wire antennas (see Table 4.1). Each of the four loading schemes has its own success story in term of optimization [15]. In this study, the series concentrated (or lumped) loading scheme is adapted, and among the choices of resistive, inductive, capacitive, or hybrid loadings, purely resistive loadings are used because of their frequency-independent nature.

The far field radiation patterns, as a function of zenith angle θ, of a BWC antenna with resistive loadings valued at 25 Ω, 50 Ω, and 75 Ω for the $\phi = 90^\circ$ and $\phi = 0^\circ$ planes are shown in Figure 4.8 and 4.9 respectively. From the figure, we can see that the patterns are relatively constant at low frequencies. At frequencies above 700 MHz, however, the patterns change with the value of loadings. The change in power gain at $\theta=90^\circ$, and $\phi=0^\circ$ is shown in Figure 4.10. The power gain of the loaded antenna decreases as the value of the resistive loadings is increased.

The impedance characteristics of the loaded structure are shown in Figure 4.11 in comparison with those of the unloaded BWC antenna. The figure shows that the discontinuity at around 750 MHz shrinks as the value

of the loadings at the junction is increased. Without the discontinuity, the impedance of the antenna is better matched to the 50 Ω source and the mismatch factor of the antenna improves as shown in Figure 4.12.

The effects of varying the value of the resistive loadings on the BWC antenna is summed up in Figure 4.13 where the antenna factors of the loaded antennas are shown. It is found that the addition of loadings improves the antenna factor of the BWC antenna at around 750 MHz. However, there is no remarkable change in the overall performance of the antenna. Also, since the addition of resistive loadings reduces the efficiency of the antenna, this particular method of optimization is not always justifiable.

Table 4.1 Loading Schemes for Wire Antennas.

Loading Scheme	Current Distribution	Example
Series Distributed Loading	The current in wire segments is associated with a continuous distribution of (locally) axial electric field which is a function of the current intensity at the point of the segment considered.	An antenna made from a resistive rod.
Series Concentrated, or Lumped Loading	The voltage between two close points along a segment is a function of the current between these two points and remains finite if (theoretically) the two points become infinitely close.	An electrically small coil inserted betweem two antenna segments.
Shunt Distributed Loading	Distributed current exists along the segment perpendicular to the local segment axis and is a function of the local radial electric field.	An antenna with a thin protective dielectric coating over the wire.
Concentrated (Lumped) Shunt Loading	The above effects is localised to a very small part of a segment, but results in a finite radial current.	An antenna with a thin metallic disc mounted on the wire perpendicular to its axis.

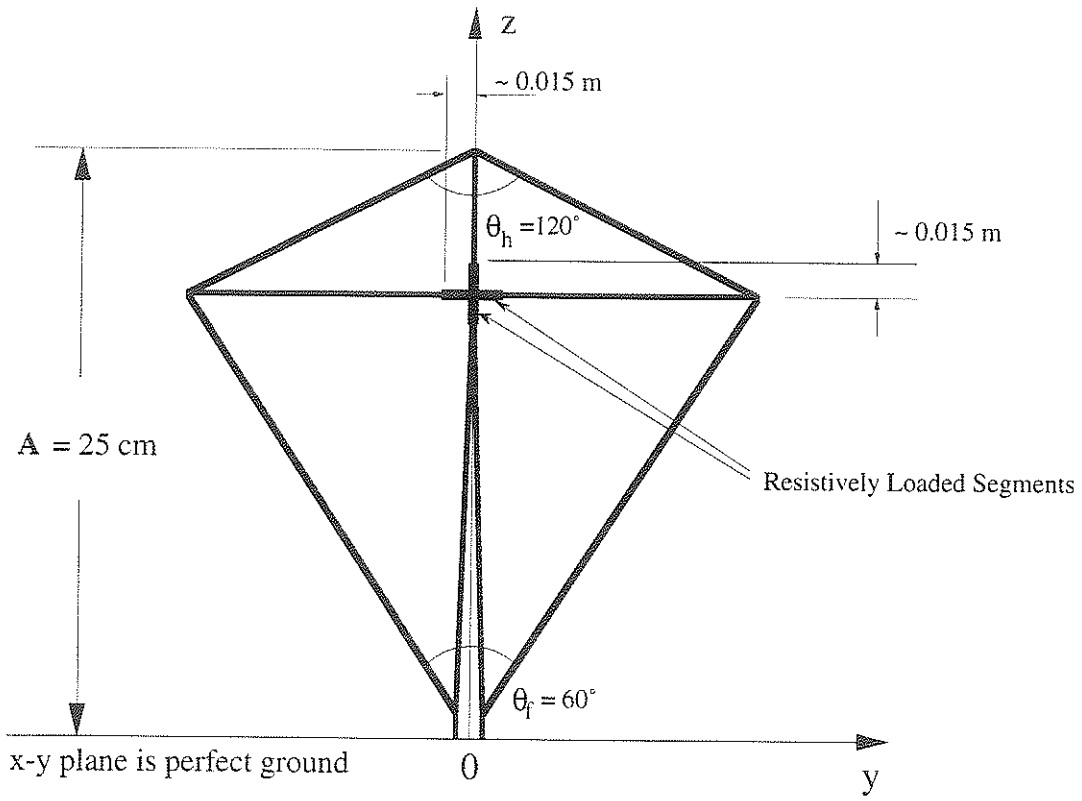

Figure 4.7 Loading Scheme of a BWC Antenna with θ_f=60° and θ_h=120°.

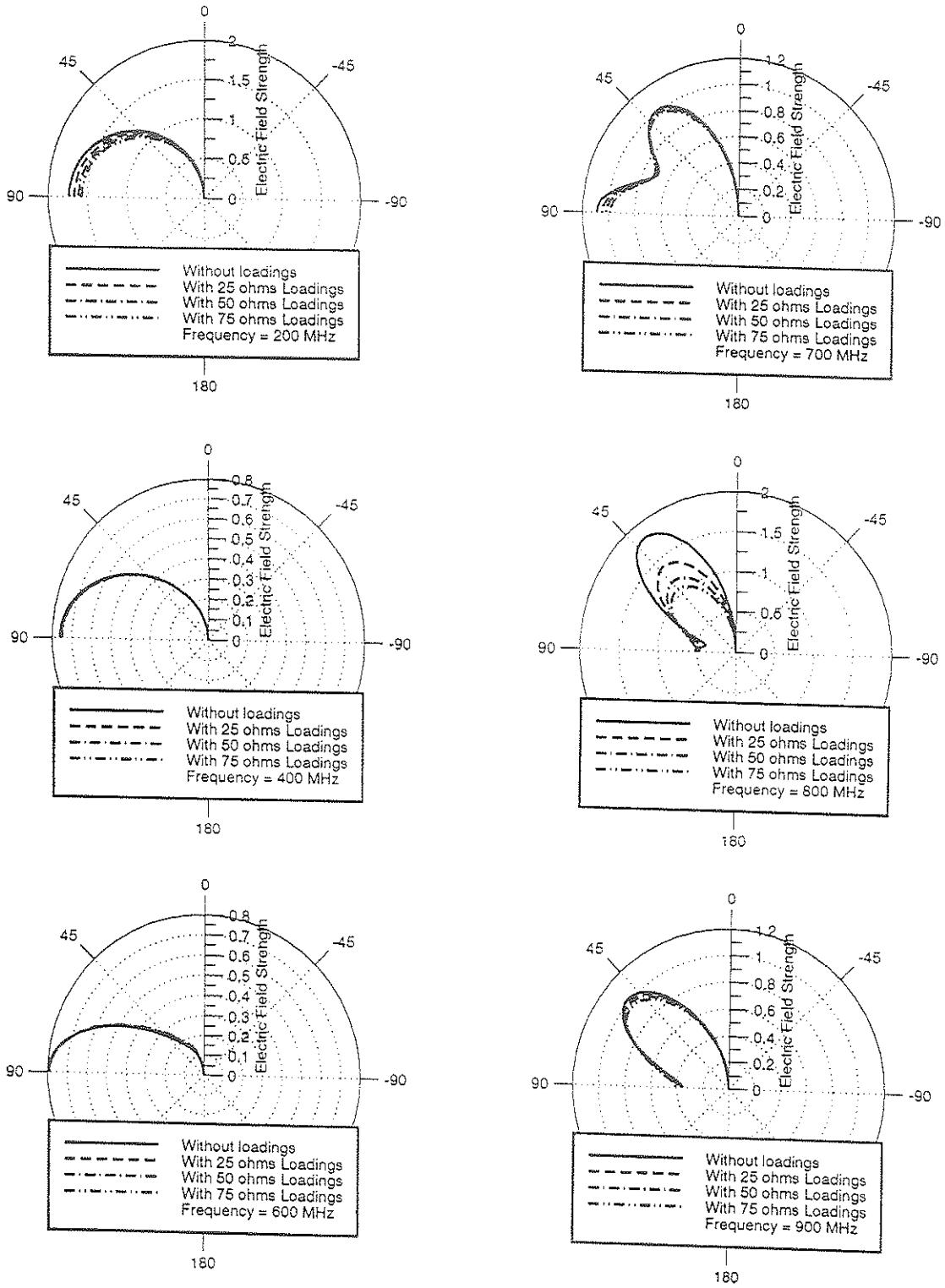

Figure 4.8 Far Electric Field (E_θ) Patterns of a BWC Antenna with Resistive Loadings Valued at 25 Ω, 50 Ω, and 75 Ω as a Function of Zenith Angle θ and $\phi = 90^\circ$.

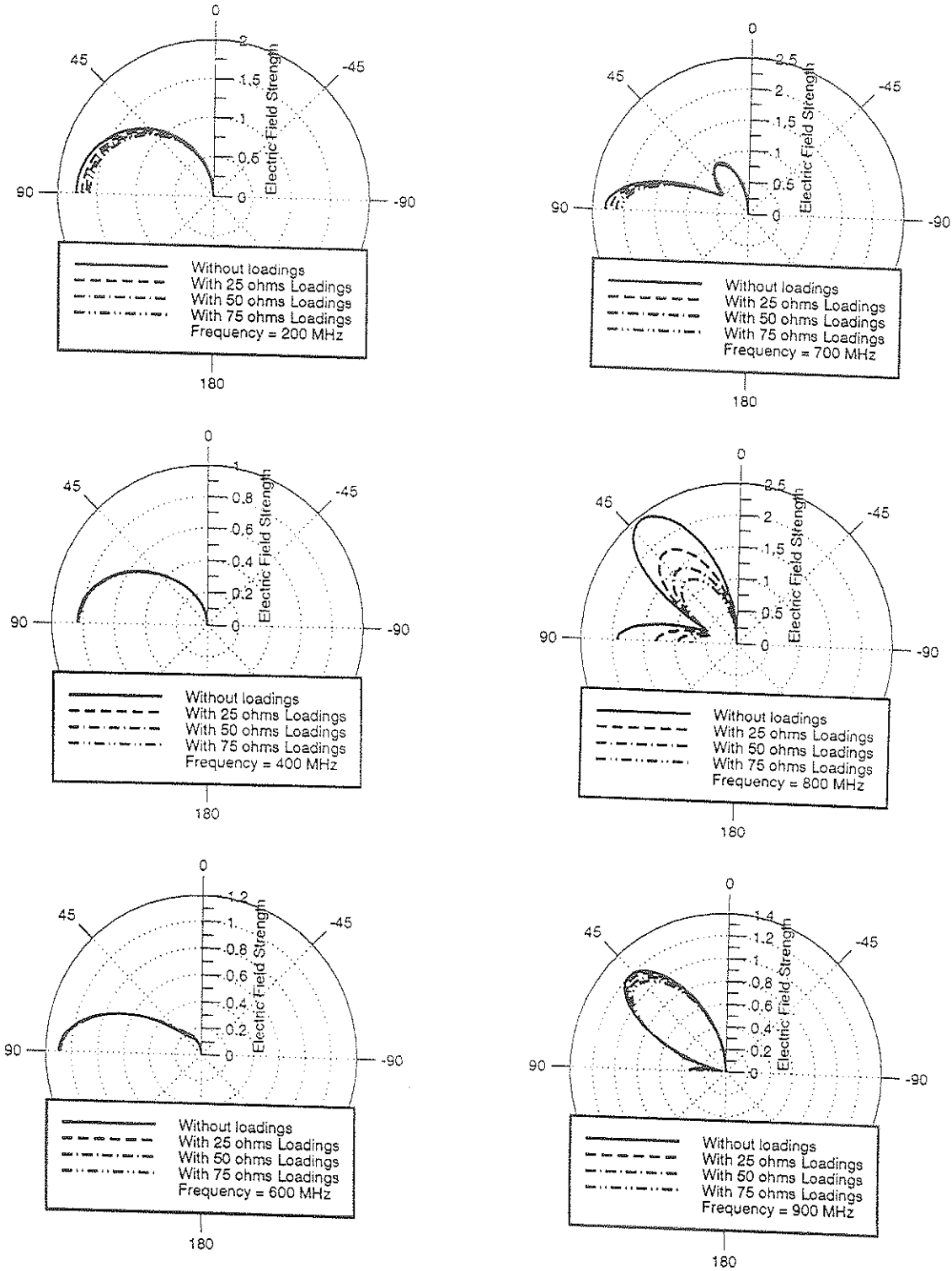

Figure 4.9 Far Electric Field (E_θ) Patterns of a BWC Antenna with Resistive Loadings Valued at 25 Ω, 50 Ω, and 75 Ω as a Function of Zenith Angle θ and $\phi = 0^\circ$.

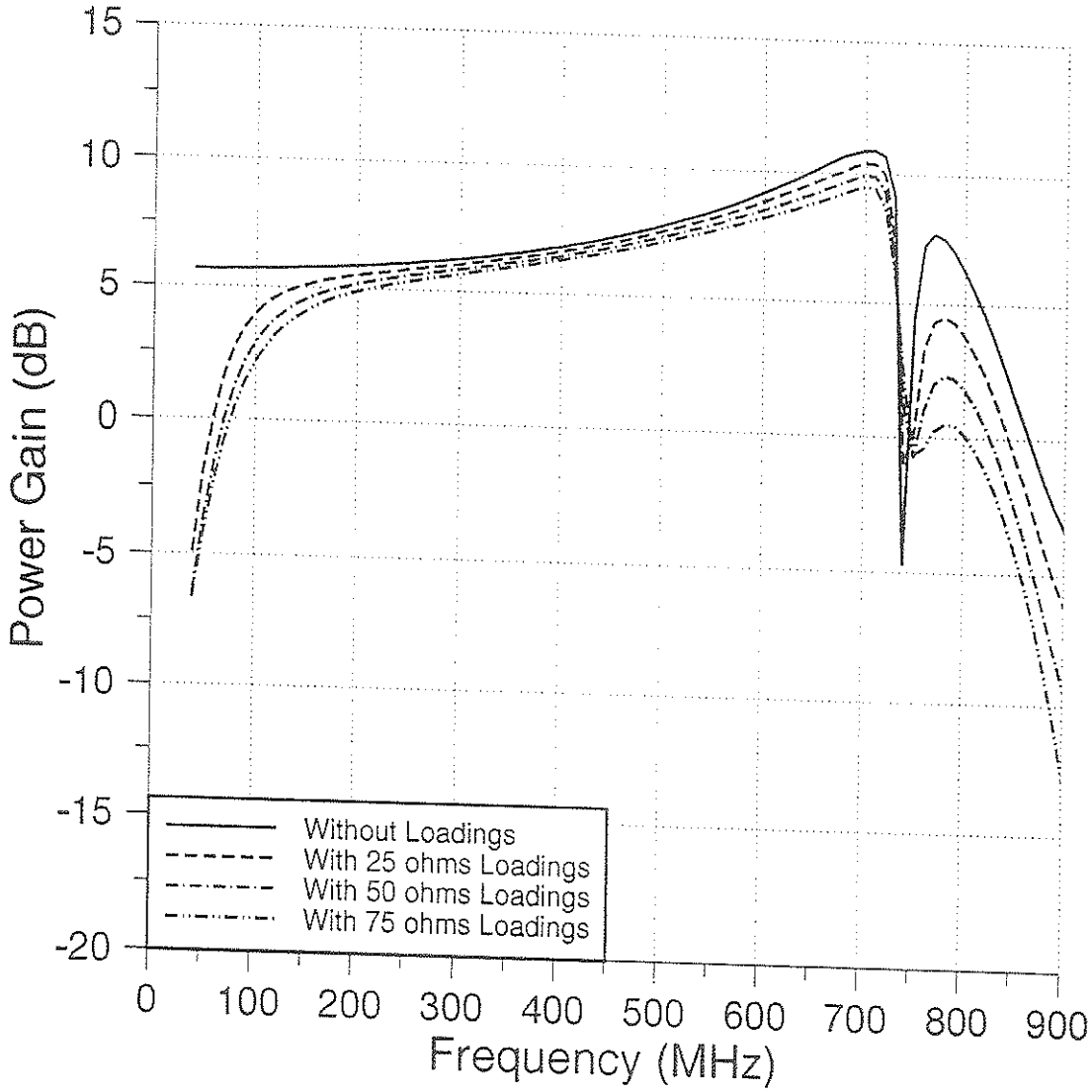

Figure 4.10 Power Gain Curves of a BWC Antenna with Resistive Loadings Valued at 25 Ω, 50 Ω, and 75 Ω for $\theta = 90^\circ$ and $\phi=0^\circ$.

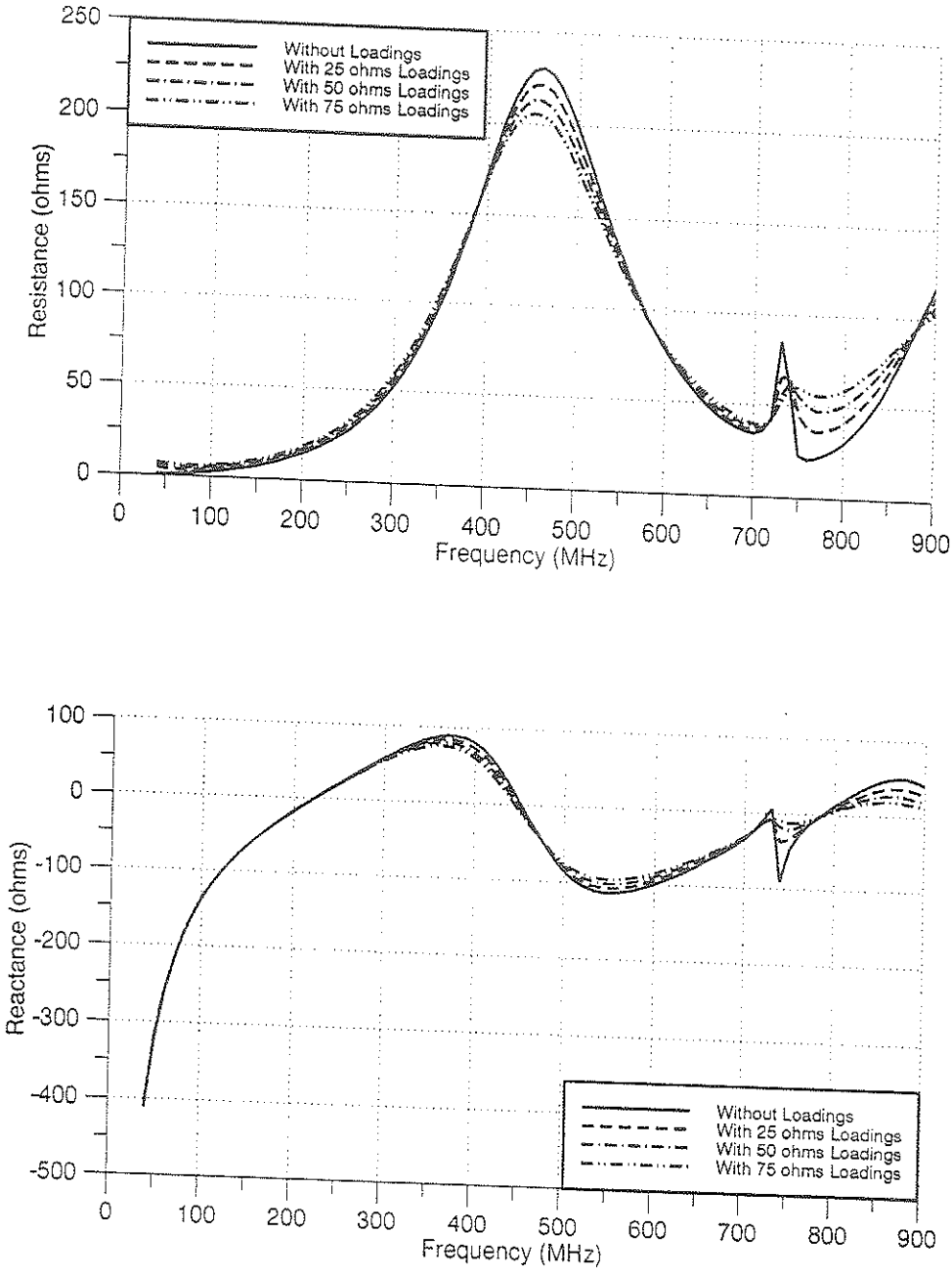

Figure 4.11 Input Impedance Curves of a BWC Antenna with Resistive Loadings Valued at 25 Ω, 50 Ω, and 75 Ω.

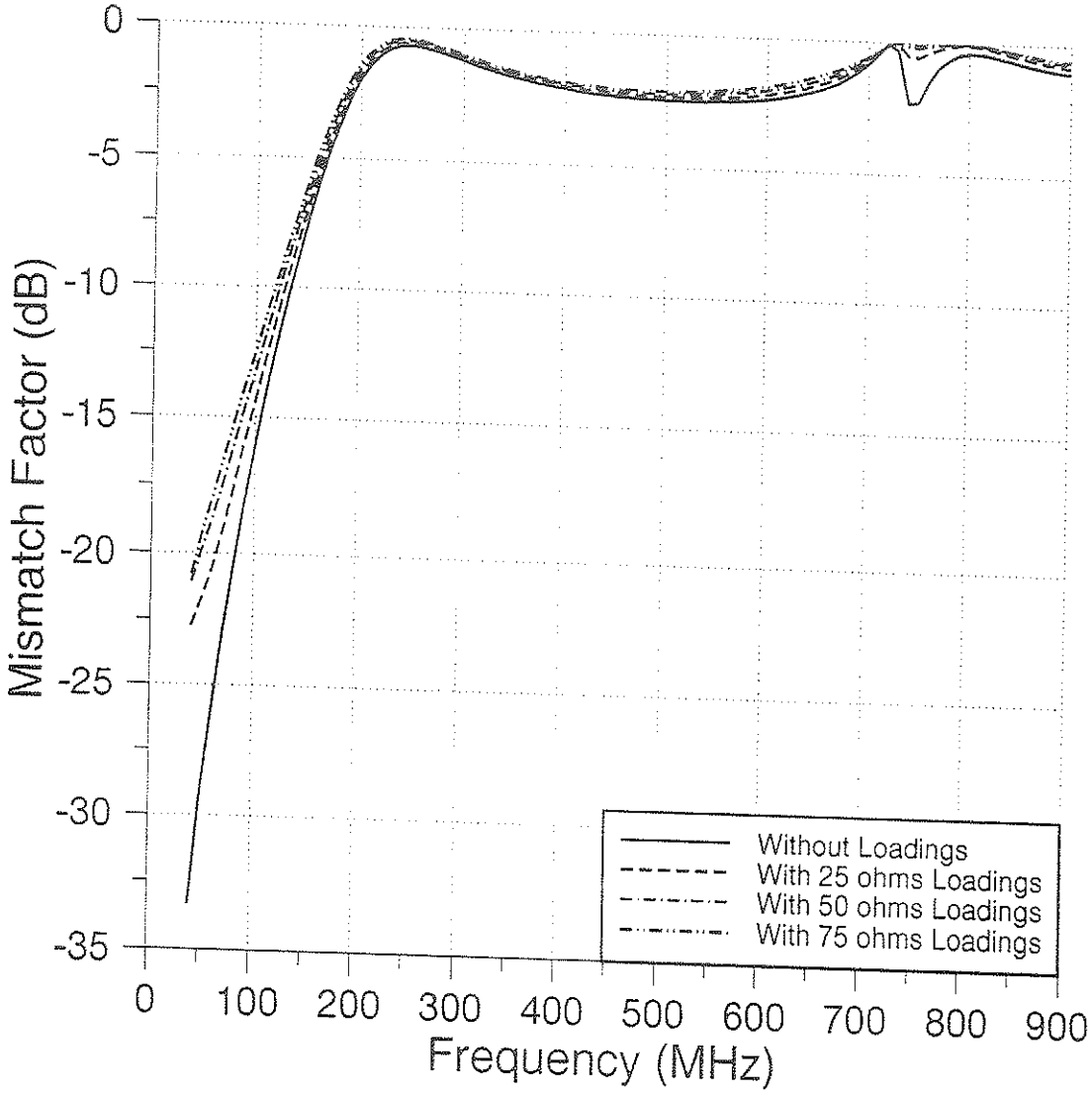

Figure 4.12 Mismatch Factor Curves of a BWC Antenna with Resistive Loadings Valued at 25 Ω, 50 Ω, and 75 Ω.

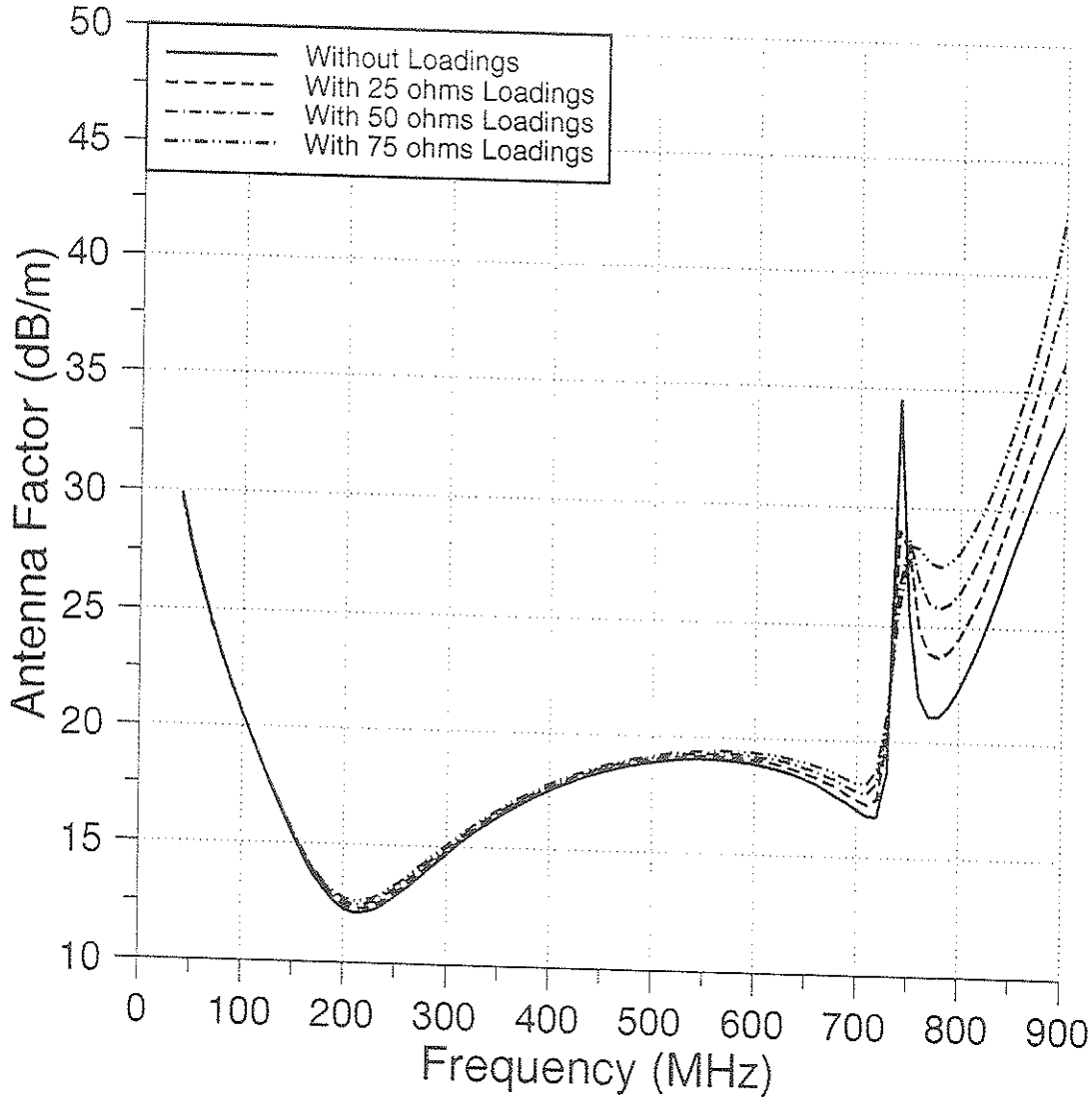

Figure 4.13 Antenna Factor Curves of a BWC Antenna with Resistive Loadings Valued at 25 Ω, 50 Ω, and 75 Ω.

4.3 OPTIMIZATION BY MODIFICATION OF ANTENNA SHAPE

4.3.1 Double-Biconical Antenna

The double-biconical antenna shown in Figure 4.14 can be thought of as a bowtie antenna with offset feed. By feeding the planar biconical antenna at a location other than its base, an extra freedom is created. When the source is elevated, the bottom portion of the antenna is made into an inverted biconical structure with the same flare angle as the top portion (hence the name "double-biconical antenna"). The change in feed location would change the current distribution which would in turn change the electrical properties of the antenna. In this study, the analysis of double-biconical antennas with source height from 0.025 to 0.150 m in 0.025 m increments, θ_f=60°, and θ_h=180° is done using the NEC2. It should be noted that the size, flare and hat angle of the antenna remains constant for different source heights.

If the source segments are elevated, the change in radiation patterns can be observed in Figures 4.15 and 4.16 where the far electric field (E_θ) patterns, at both the ϕ=90° and ϕ=0° plane, of double-biconical antennas with flare and hat angle of 60° and 180° is compared with that of the original bowtie. The change in pattern is especially obvious at higher frequencies. This change in pattern affects the power gain of the antenna in a way as shown in Figure 4.17 where the power gain of double-biconical antennas with different source heights are compared with that of the original bowtie. From the figure, it can be seen that the drop in power gain happens at higher frequencies for double-biconical antennas. As the

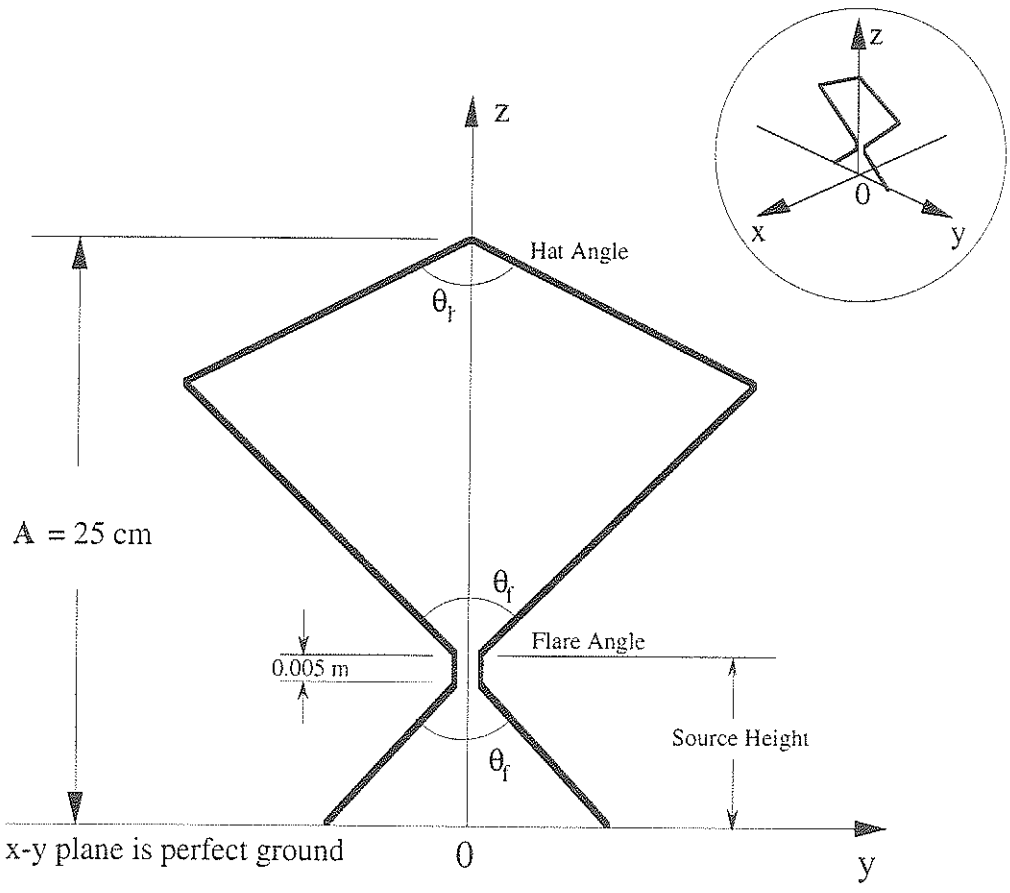

Figure 4.14 Configuration of a Double-Biconical Antenna.

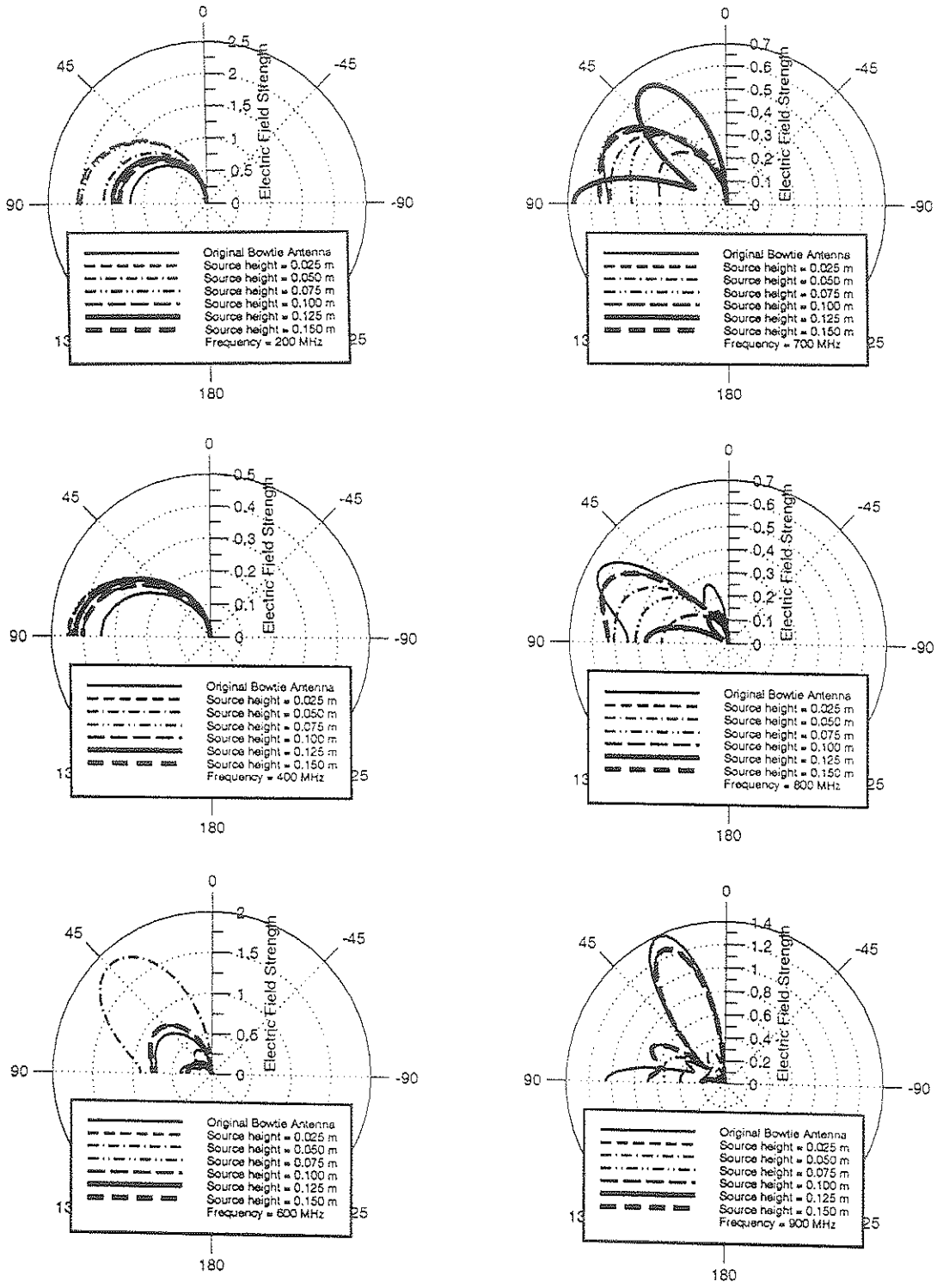

Figure 4.15 Far Electric Field (E_θ) Patterns of a Double-Biconical Antenna with θ_f=60°, θ_h=180°, and Different Source Heights as a Function of Zenith Angle θ and ϕ = 90°.

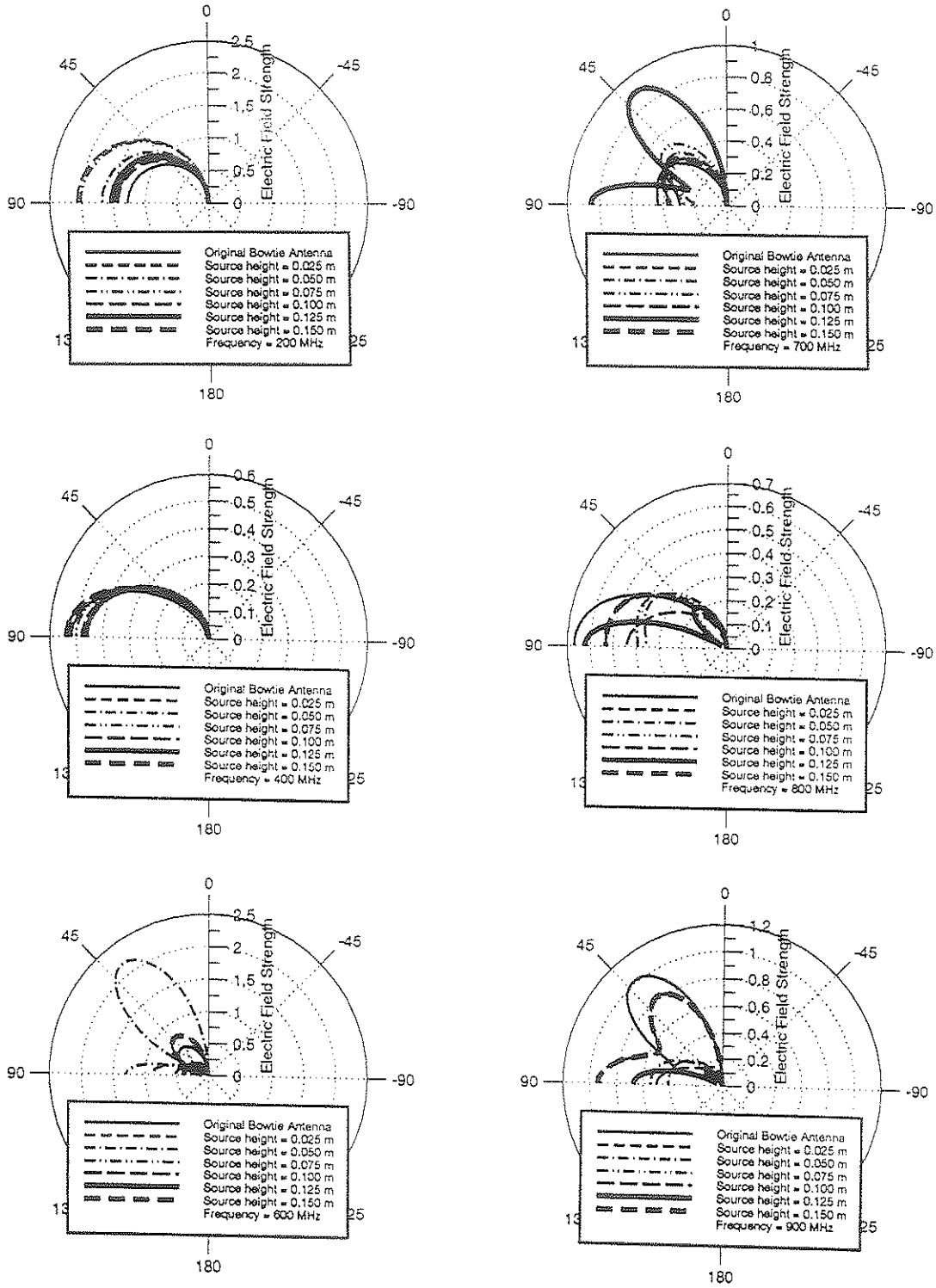

Figure 4.16 Far Electric Field (E_θ) Patterns of a Double-Biconical Antenna with θ_f=60°, θ_h=180°, and Different Source Heights as a Function of Zenith Angle θ and ϕ = 0°.

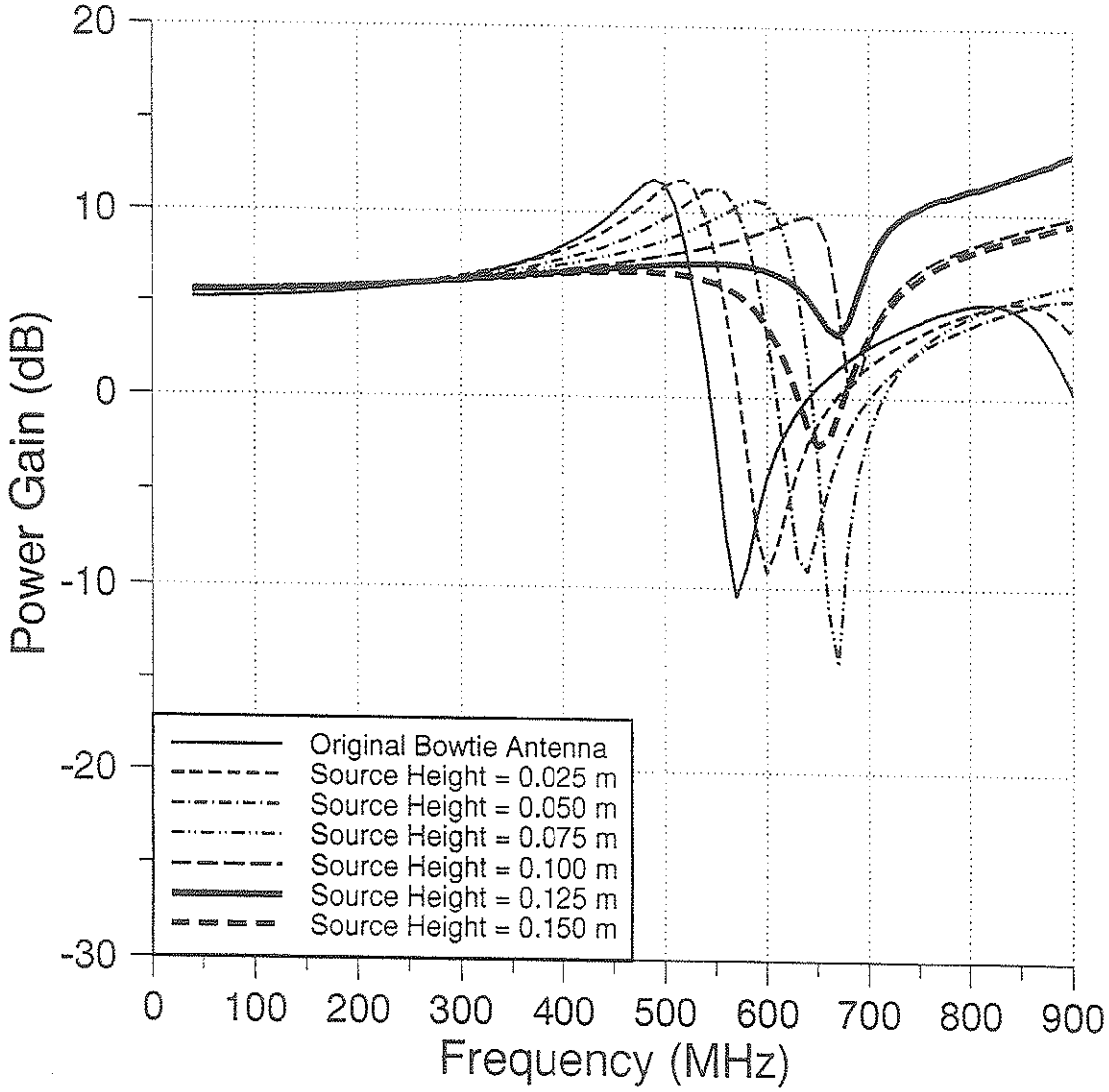

Figure 4.17 Power Gain Curves of Double-Biconical Antennas with θ_f=60°, θ_h=180°, and Different Source Heights.

height of the source segments is increased, the frequency at which the drop occurs increases. After 0.125m, however, an increase in source height would cause the drop in power gain to occur at a lower frequency.

The impedance characteristics of double-biconical antennas with flare and hat angle of 60° and 180° and various source heights are compared with that of the original bowtie in Figure 4.18. The shift in antiresonant frequencies are gradual and towards the high frequency end for source height of up to 0.125 m. Raising the source segments beyond 0.125 m would cause the antiresonant frequencies to shift in the opposite direction. We can see the effects the feed position has on the mismatch factor from Figure 4.19, where the mismatch factors of double-biconical antennas with various source heights are compared with that of the original bowtie.

The antenna factor curves of double-biconical antennas with different source heights are shown in Figure 4.20 where the antenna factor of the original bowtie antenna is also shown for comparison. As the height of the source segments is increased, so does the bandwidth of the antenna factor. This phenomenon continues until the source segments are elevated towards the mid-point of the wire structure. At this point, raising the source any higher would cause the antenna factor curve to deteriorate and hence dampens the overall performance of the antenna.

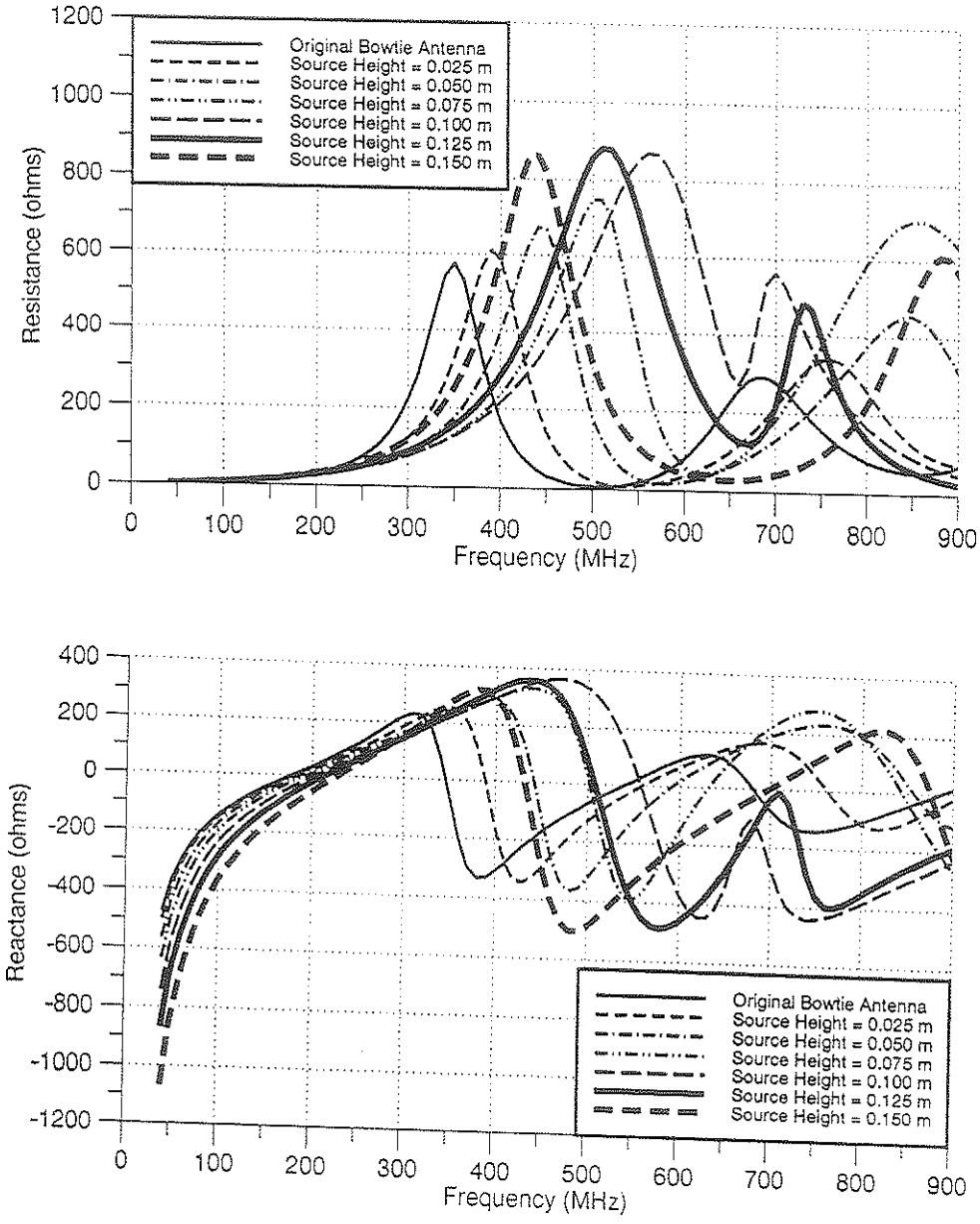

Figure 4.18 Input Impedance Curves of Double-Biconical Antennas with θ_f=60°, θ_h=180°, and Different Source Heights.

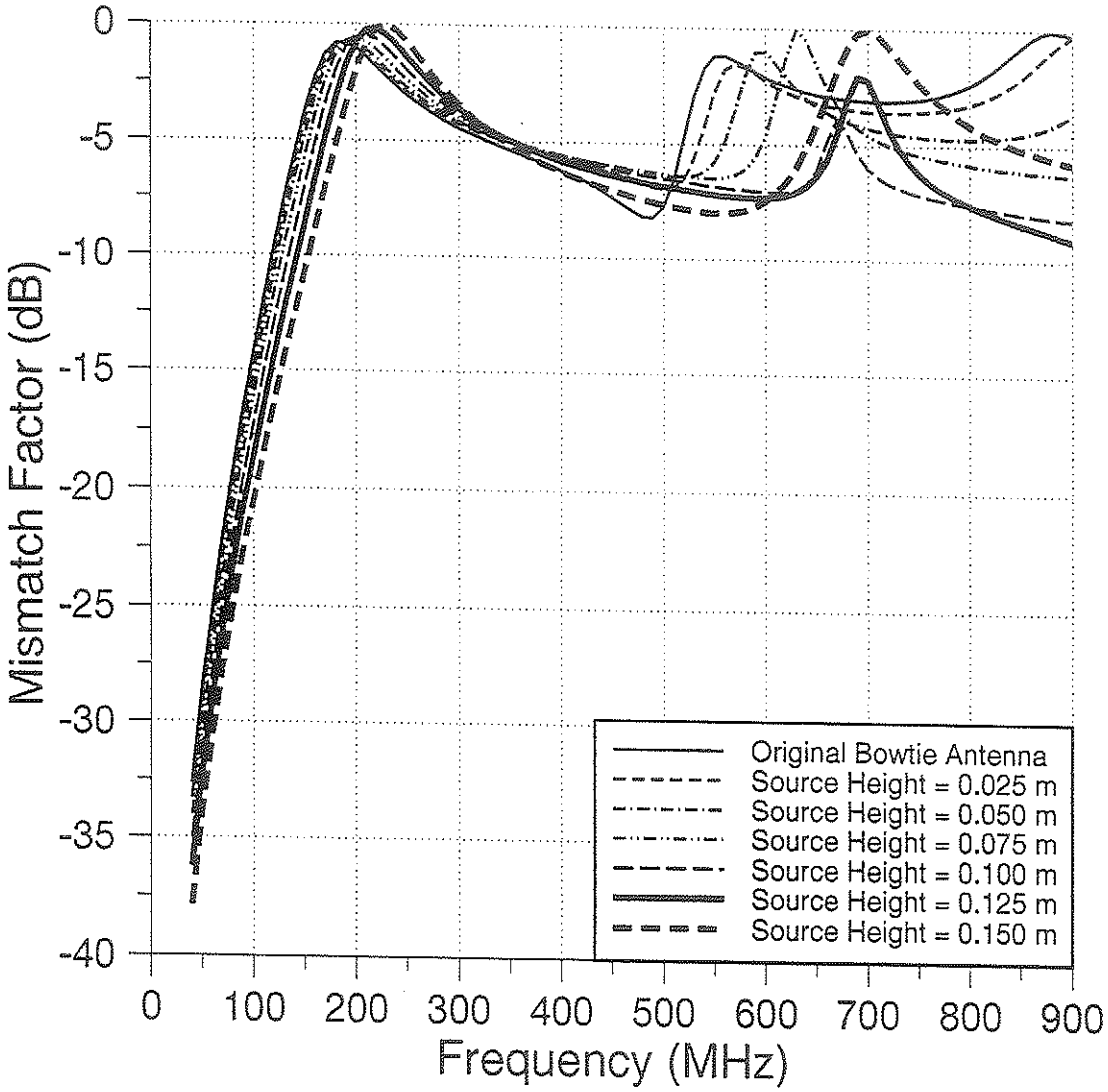

Figure 4.19 Mismatch Factor Curves of Double-Biconical Antennas with θ_f=60°, θ_h=180°, and Different Source Heights.

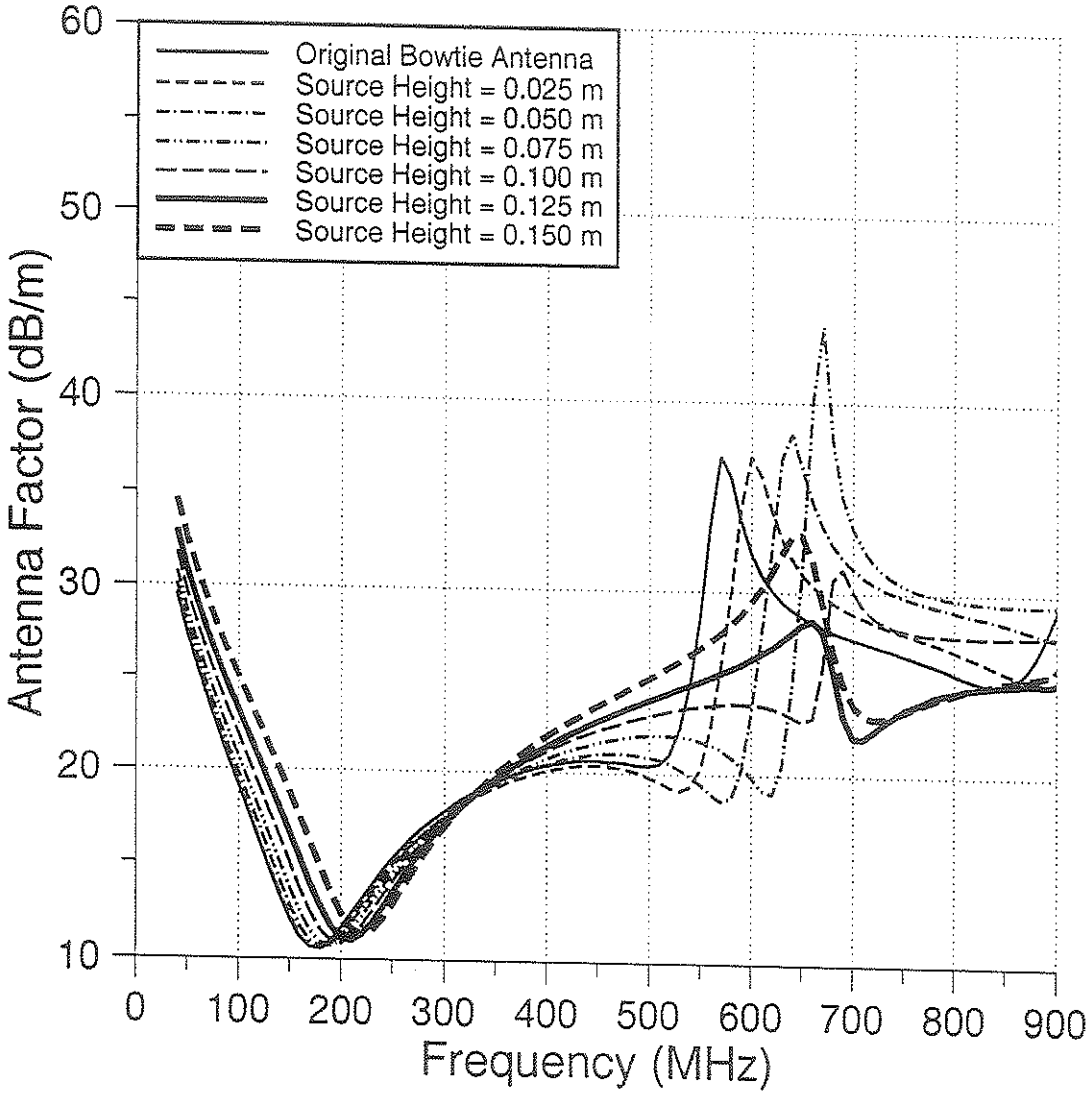

Figure 4.20 Antenna Factor Curves of Double-Biconical Antennas with θ_f=60°, θ_h=180°, and Different Source Heights.

4.3.2 Biconical Antenna with Parasitic Elements

Parasitic elements are very useful in situations where, for example, an antenna is needed to match its feed at two or more arbitrary, relatively close frequencies. Popovic et al [15] have, in fact, studied the use of parasitic elements on saguaro-cactus like antennas with two and three branches using the length of the elements as the antenna's optimization parameter. In this study, the effect of superimposing parasitic elements on a planar wire biconical antenna is examined using the model shown in Figure 4.21. Besides the length of the parasitic elements, the angle which they made with the horizontal plane is also used as a parameter. The parasitic elements on both sides of the antenna is symmetrical in construction to preserve the symmetrical nature of the antenna in the y-z plane. Both the length of the parasitic element and the angle they made with the horizontal plane are varied to examine their influence on the electrical properties of the planar antenna.

The study begins with the length of the parasitic elements fixed at about 0.14 m. The planar wire biconical antenna used has a flare and hat angle of 60° and 180°, respectively. The angle α is then varied from 0° (i.e., with the parasitic elements parallel to the ground plane) to 20° in 5° increments. In the second part of the study, the same biconical antenna is used but with the angle α fixed at 10° and the length of the parasitic elements varied from 0.10 m to 0.18 m in 0.02 m increments. The change in antenna factor characteristics is tabulated in Figure 4.22 and 4.23 for the two cases respectively. From the figures, it can be concluded that, for the selected parameters, the addition of parasitic elements in the form shown in

Figure 4.21 does not contributed to the improvement of the antenna factor's bandwidth performance.

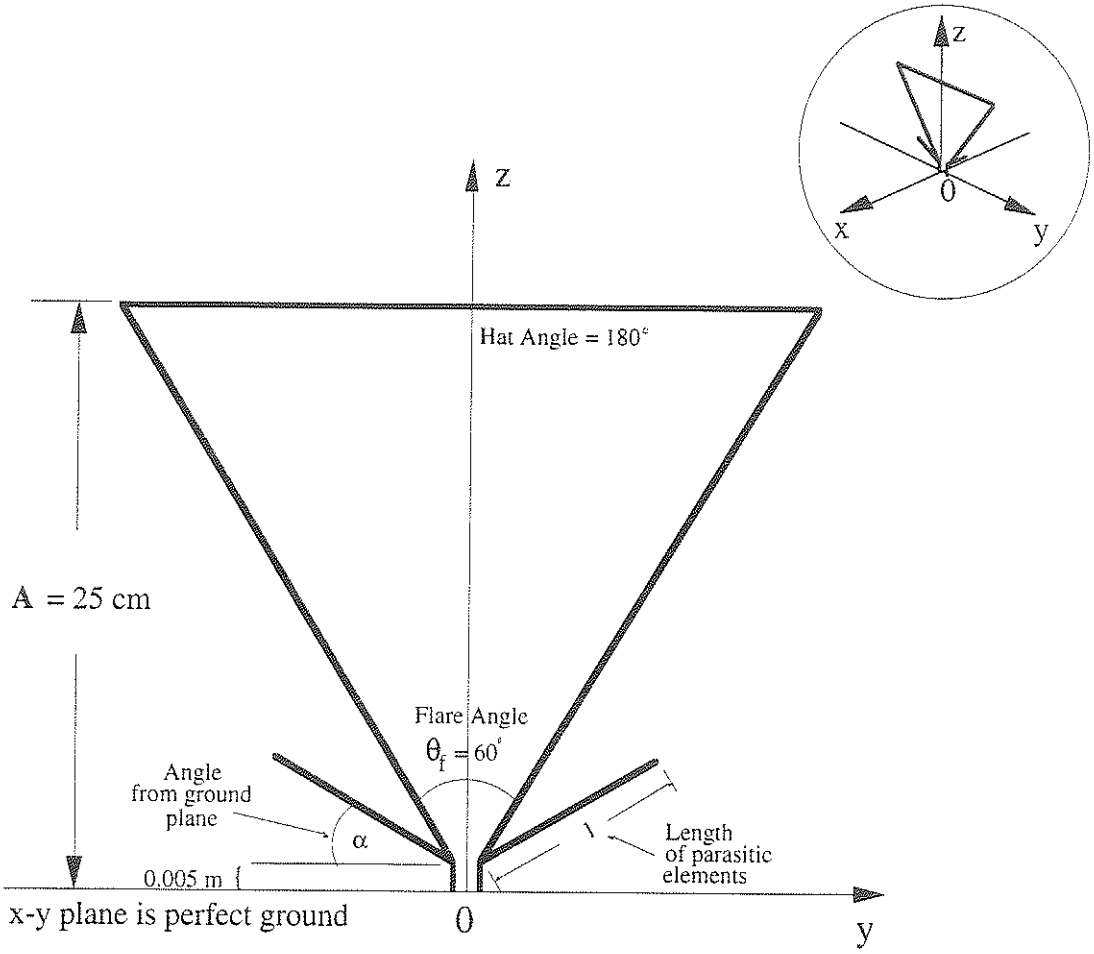

Figure 4.21 Configuration of a Planar Wire Biconical Antenna with Parasitic Elements.

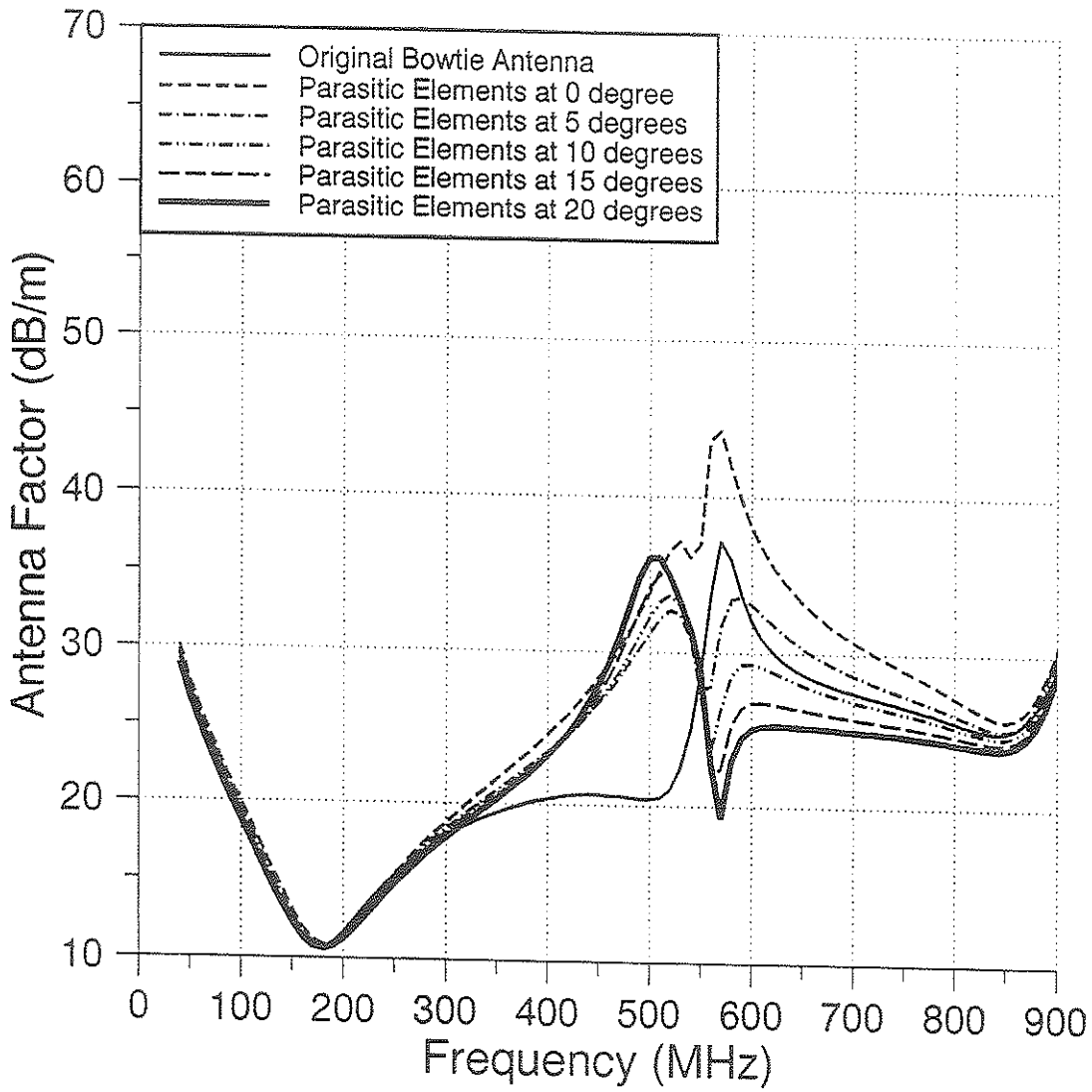

Figure 4.22 Antenna Factor Curves of a Planar Wire Biconical Antenna with Parasitic Elements at Different Angles.

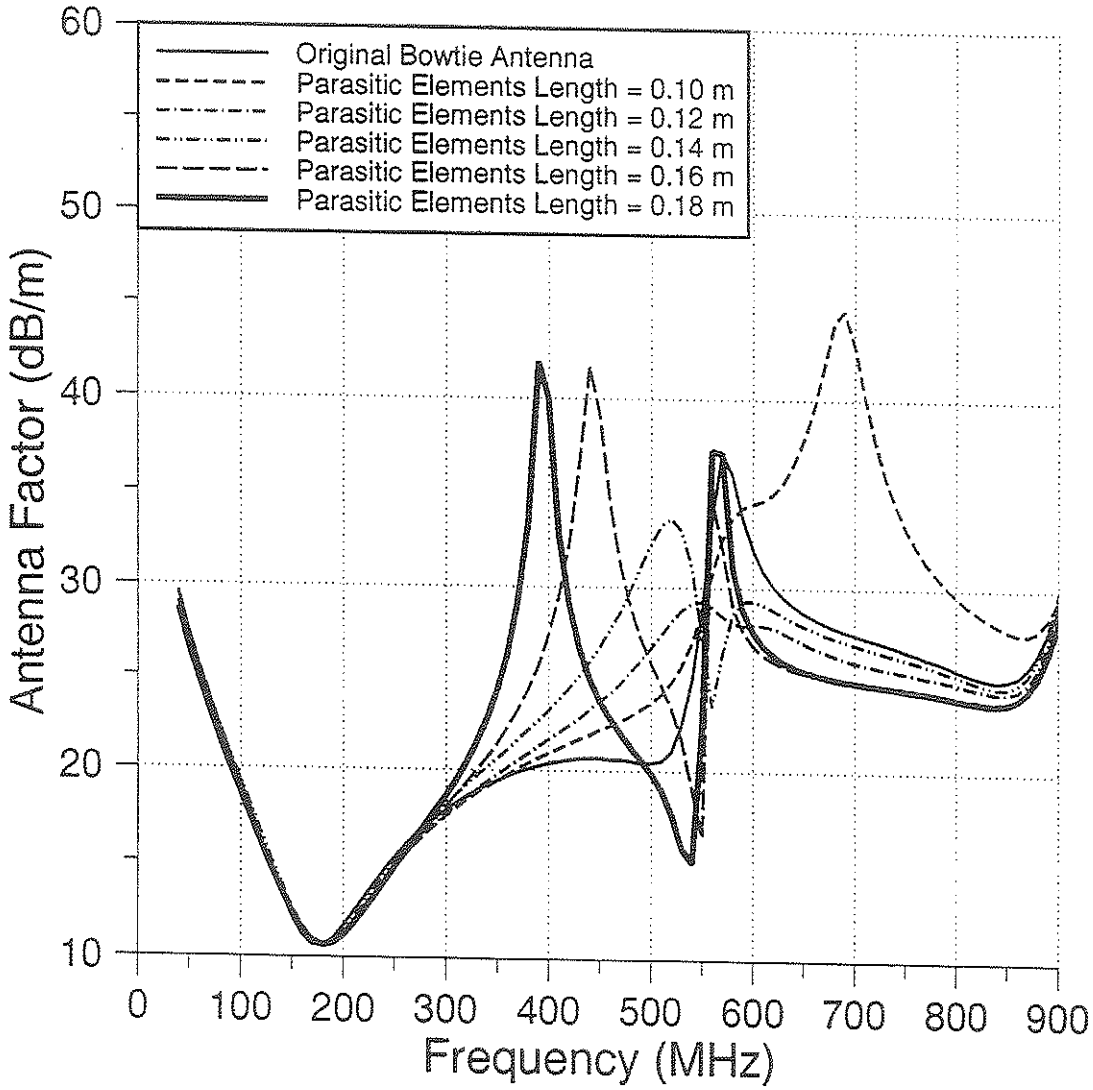

Figure 4.23 Antenna Factor Curves of a Planar Wire Biconical Antenna with Parasitic Elements of Different Lengths.

4.4 BICONICAL ANTENNA WITH SLEEVE

The idea in section 4.3.2 is modified to form the antenna with sleeve setup in Figure 4.24.

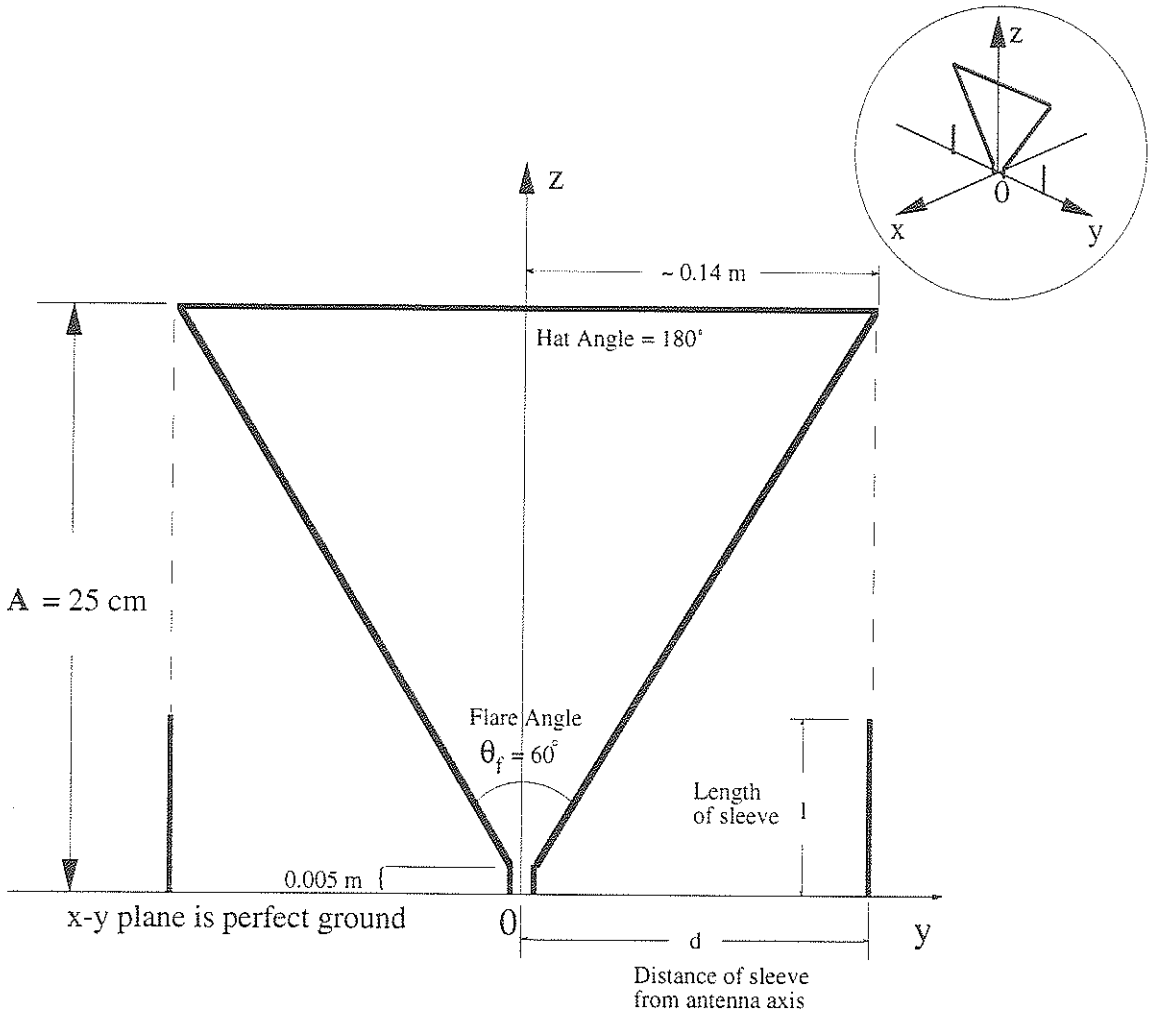

Figure 4.24 Planar Wire Biconical Antenna with Sleeve.

The addition of two parasitic elements at a small distance from and parallel to a cylindrical monopole antenna near resonance has been known to produce a relatively good broadband antenna. The same setup has not, however, been considered for wire biconical antennas. Referring to the power gain curve in Figure 4.25, it is observed that the drop in power gain for a bowtie antenna with θ_f=60° is quite severe at 570 MHz where the antenna factor is seen to peak accordingly. The drop in power gain is caused by the "break-up" of the major lobe in the radiation pattern into minor lobes. This phenomenon is also responsible for the deterioration of the antenna factor around the "break-up" frequency. If the addition of parasitic elements corresponding to that particular frequency could channel enough power to, at the very least, "delay" the "break-up" of the major lobe, then the bandwidth of the antenna would be increased. The optimization parameters in this case are the length of the parasitic elements (i.e., the sleeve) and their distance from the antenna axis.

In the first part of the study, the length of the sleeve is varied from 0.11 to 0.15 m in 0.01 m steps. Figure 4.26 and 4.27 shows the radiation patterns of the bowtie antenna in Figure 4.24 with different sleeve lengths for the ϕ=90° and 0° planes, respectively. The effect on the power gain of the antenna is shown in Figure 4.28. From the figure, it can be seen that the drop in power gain is less severe for the antenna with sleeve configuration. The impedance characteristics of the antenna with different sleeve lengths is shown in Figure 4.29. Under such impedance values, the match to a 50Ω transmission line is shown in Figure 4.30. The performance of the antennas are compared in Figure 4.31 where the antenna factor of the antenna with sleeve configuration is plotted along-side

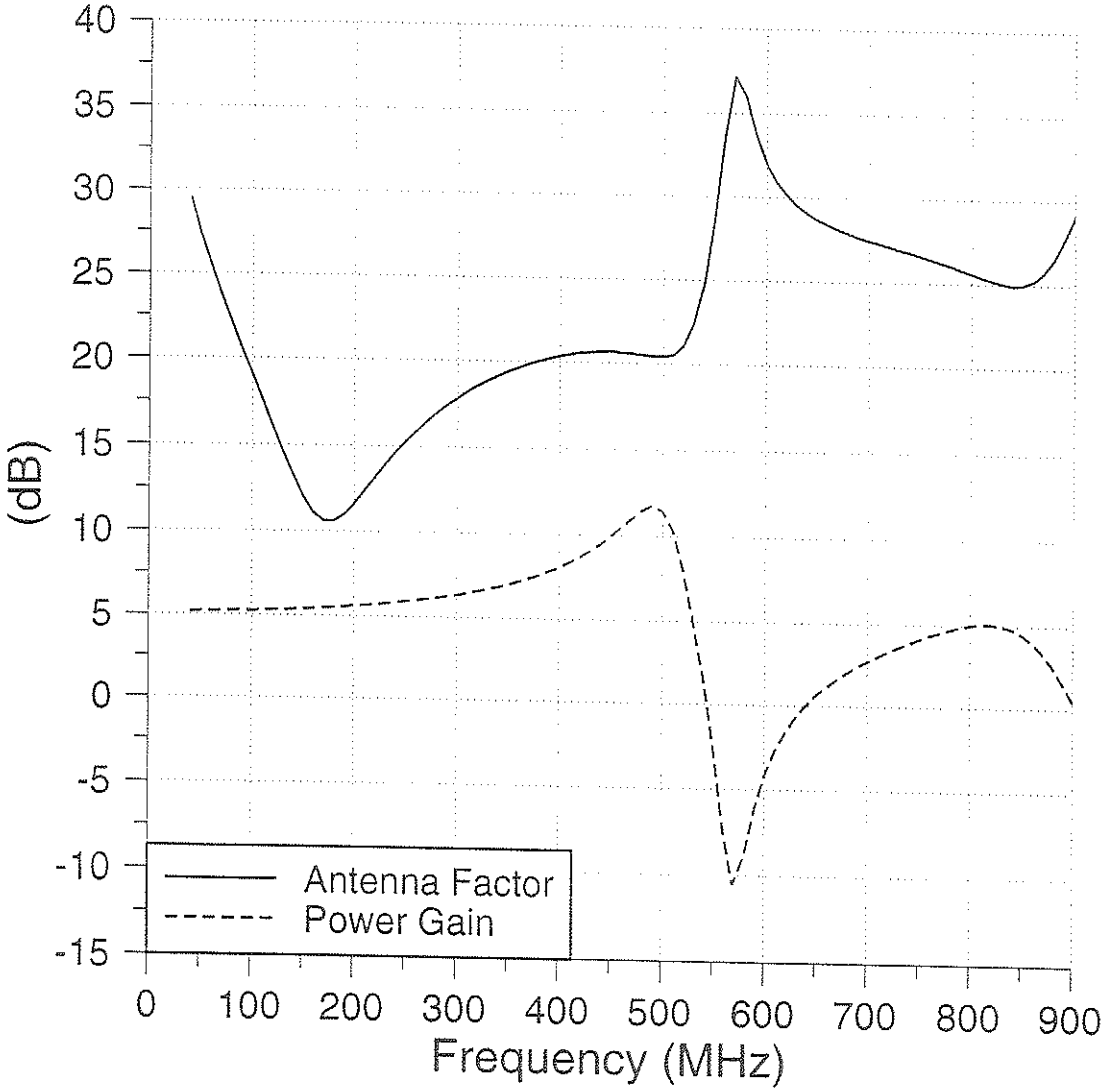

Figure 4.25 Characteristics of a Bowtie Antenna with θ_f=60°.

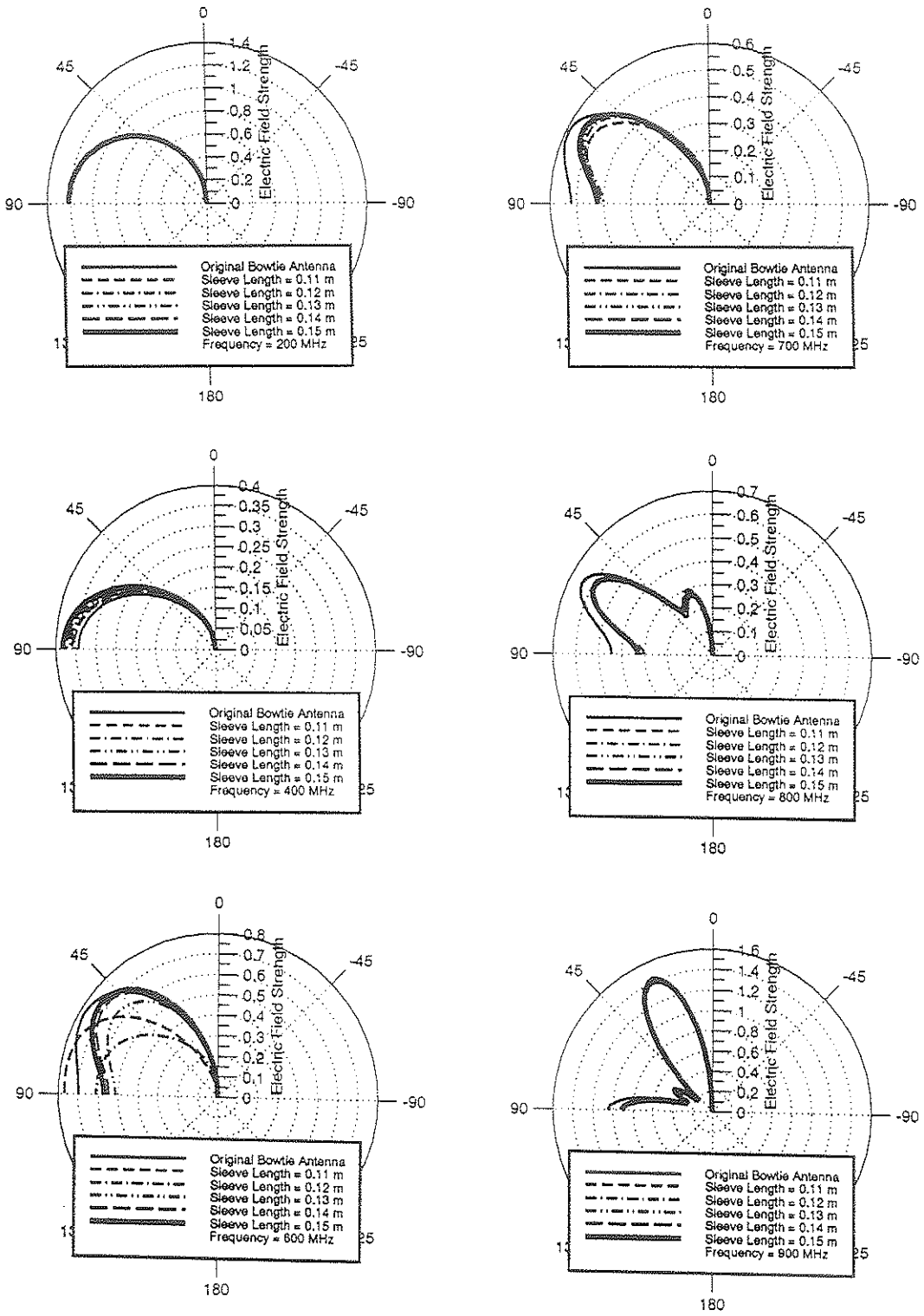

Figure 4.26 Far Electric (E_θ) Field Patterns of a Bowtie Antenna with Sleeve of Different Lengths as Function of Zenith Angle θ and ϕ=90°.

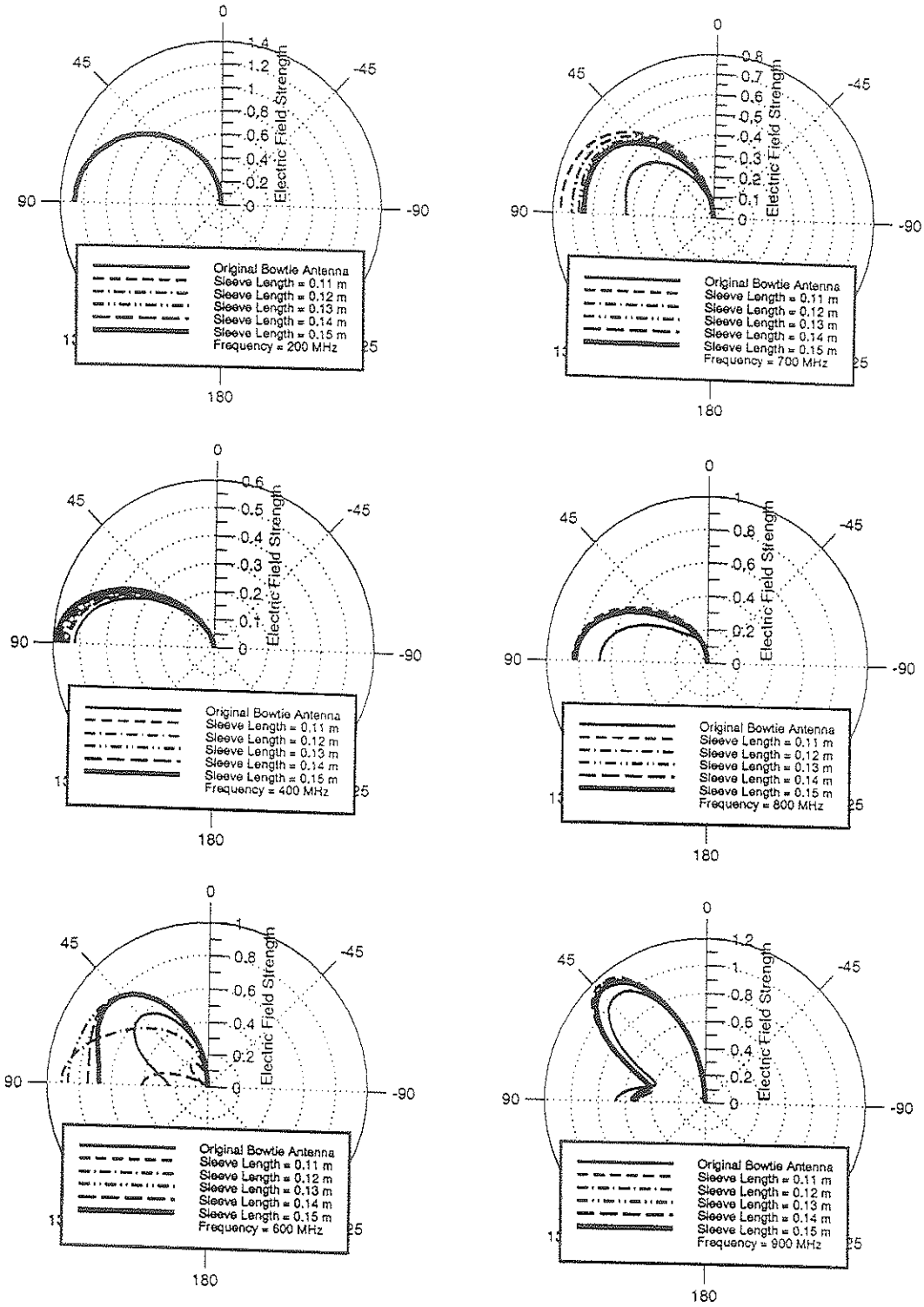

Figure 4.27 Far Electric (E_θ) Field Patterns of a Bowtie Antenna with Sleeve of Different Lengths as Function of Zenith Angle θ and ϕ=0°.

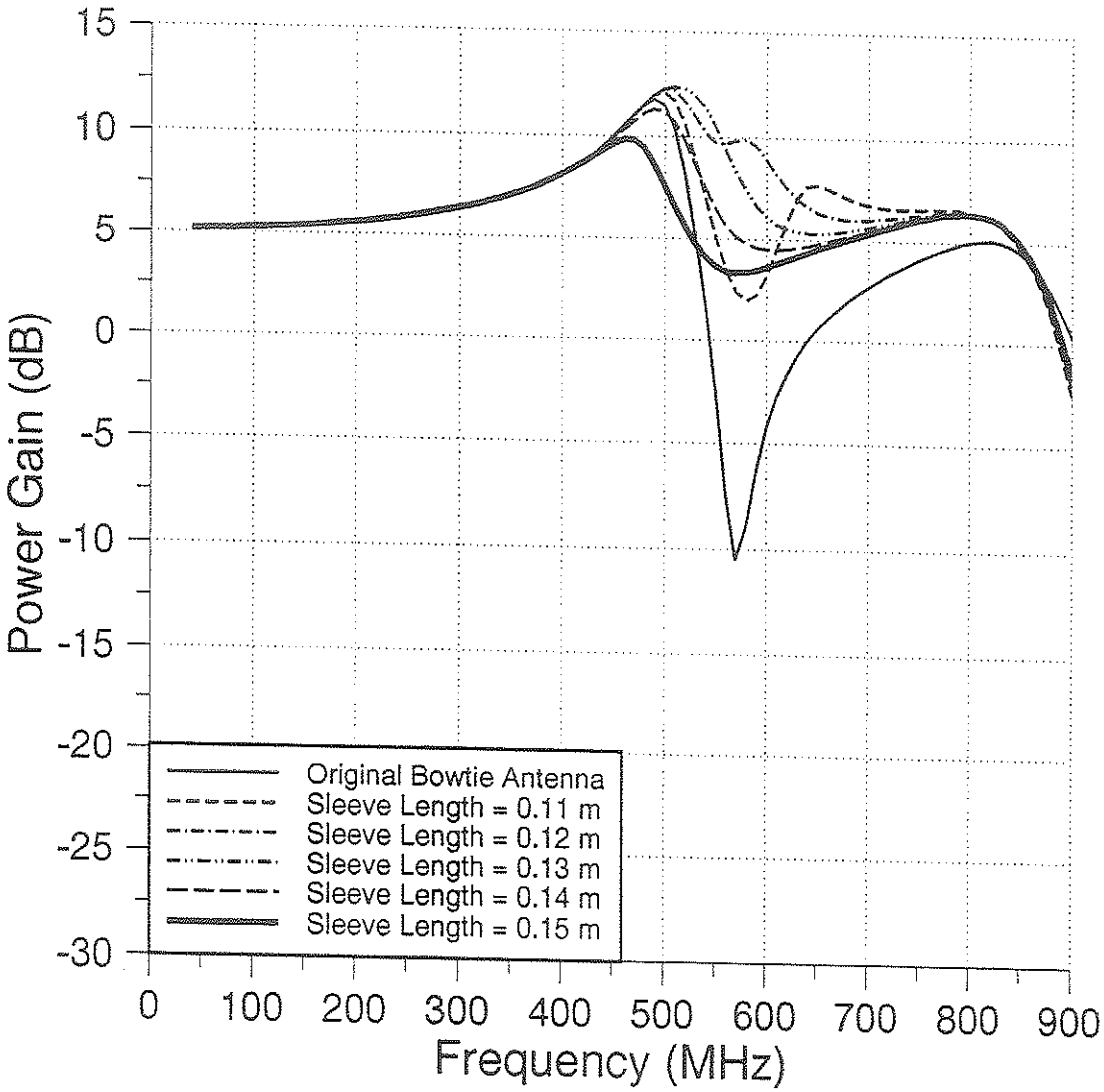

Figure 4.28 Power Gain Curves of a Bowtie Antenna with Sleeve of Different Lengths.

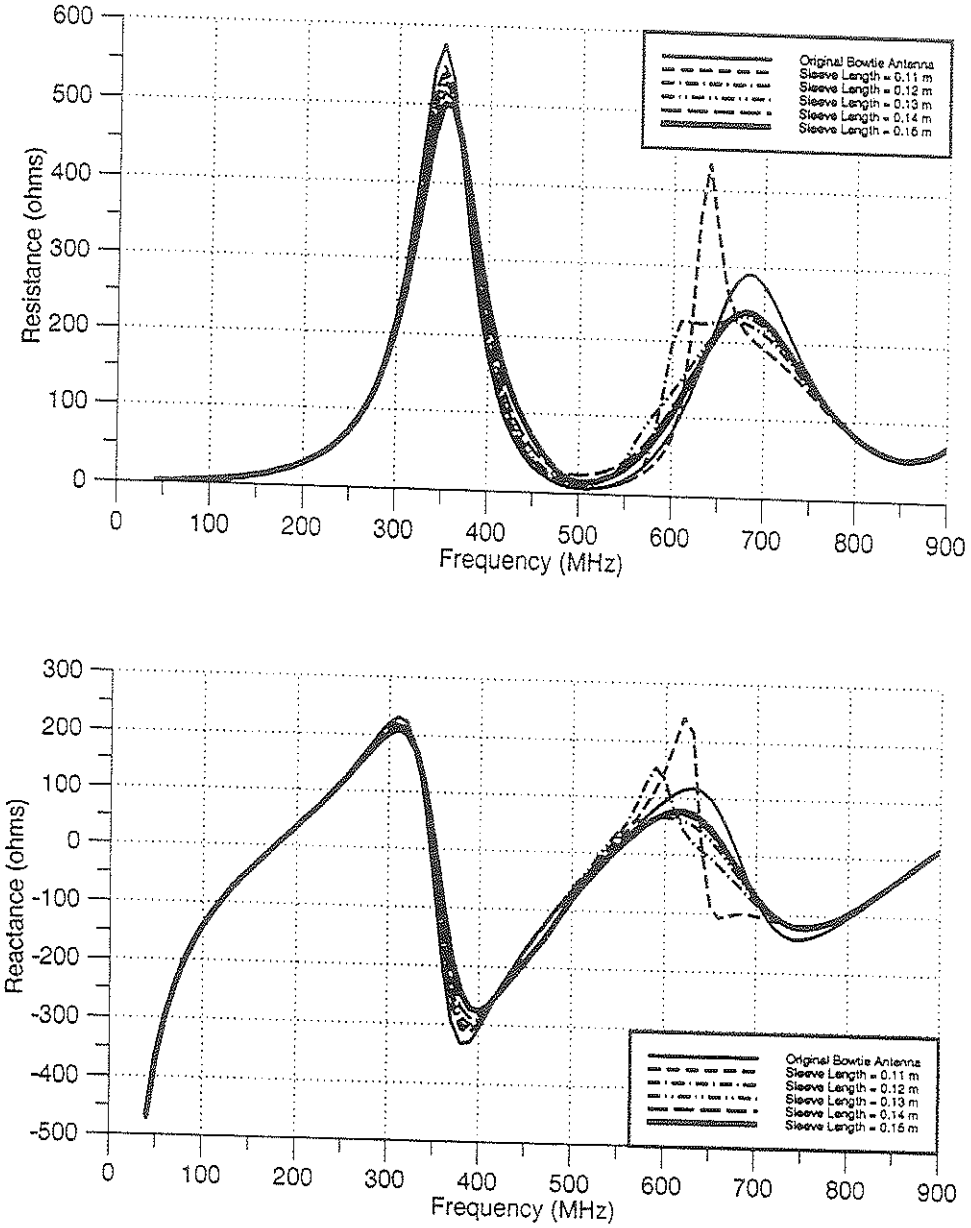

Figure 4.29 Input Impedance Curves of a Bowtie Antenna with Sleeve of Different Lengths.

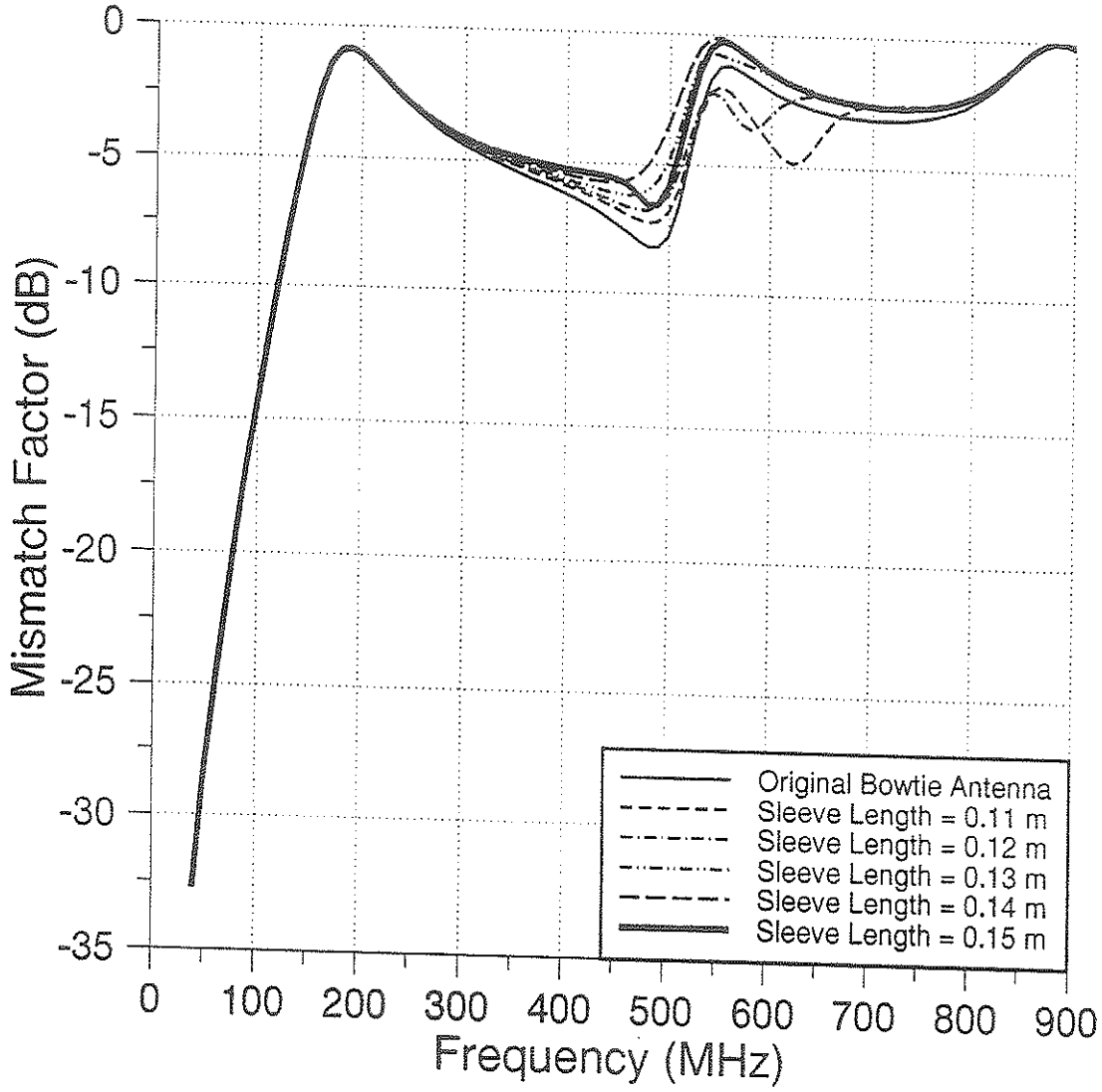

Figure 4.30 Mismatch Factor Curves of a Bowtie Antenna with Sleeve of Different Lengths.

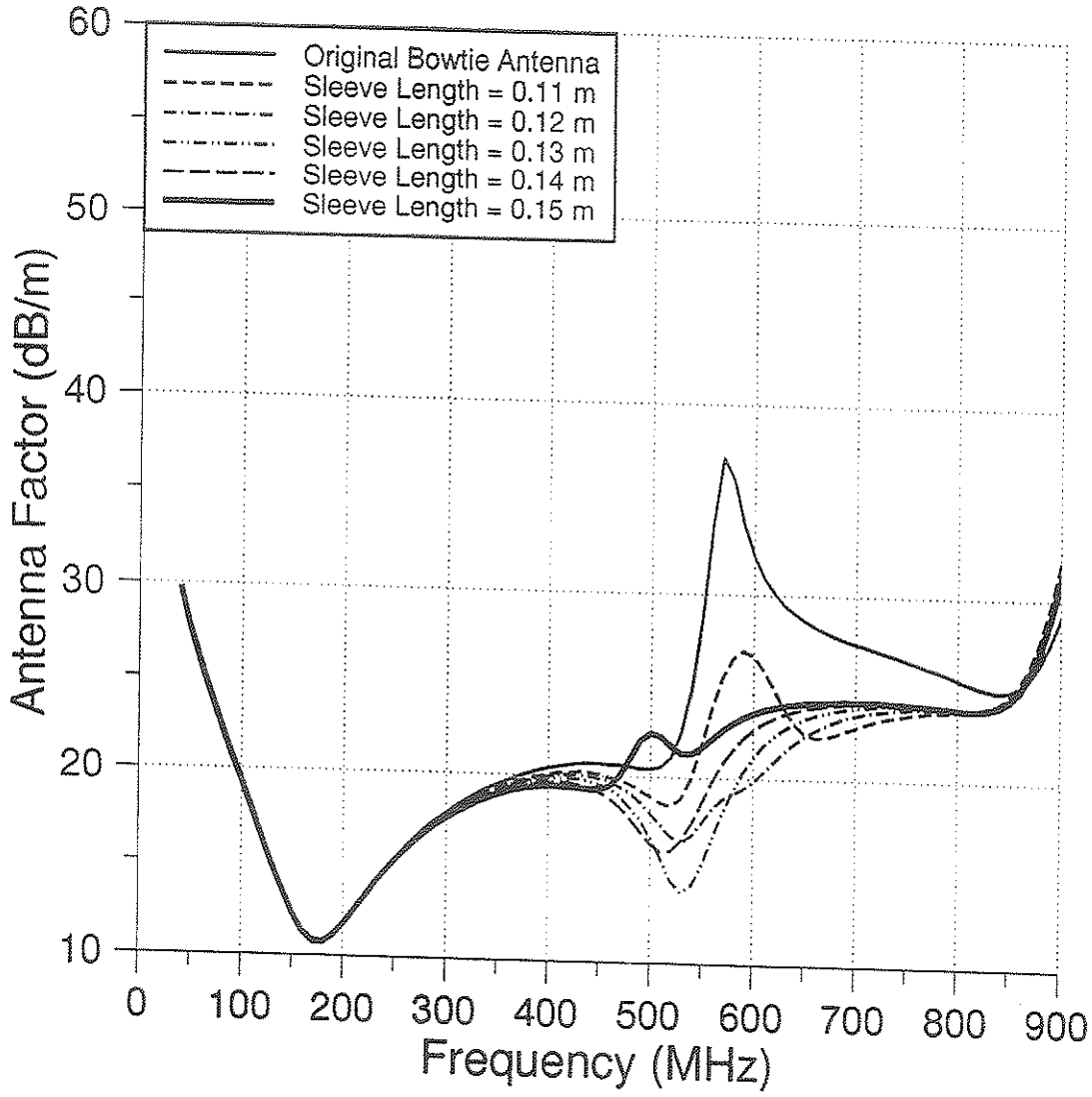

Figure 4.31 Antenna Factor Curves of a Bowtie Antenna with Sleeve of Different Lengths.

that of the original antenna. It is observed that the optimal length of the sleeve is about 0.13 m which is slightly larger than half the length of the biconical wire structure.

The second part of the study examines the correlation between the distance of the sleeve from the antenna axis and the overall characteristics of the antenna. In this part of the study, the sleeve is moved in 0.05 m steps from 0.10 m to 0.25 m away from the antenna axis. The change in far field patterns can be observed in Figure 4.32 and 4.33 where the far electric (E_θ) field patterns of antennas with various sleeve locations are compared with those of the bowtie antenna for both the ϕ=90° and 0° planes. Similar to the previous results, the drop in power gain reduces with the addition of the sleeve and when the sleeve is moved away from the antenna axis, the change in power gain is shown in Figure 4.34. The impedance characteristics of the antenna with sleeve is shown in Figure 4.35 for different sleeve distances. From the impedance characteristics, the mismatch factor of the antenna can be calculated as shown in Figure 4.36. At this point, the change in antenna factor for all the various sleeve locations is tabulated and shown in Figure 4.37. It was observed that optimal distance within which the sleeve should be placed is about 0.15 m from the antenna axis.

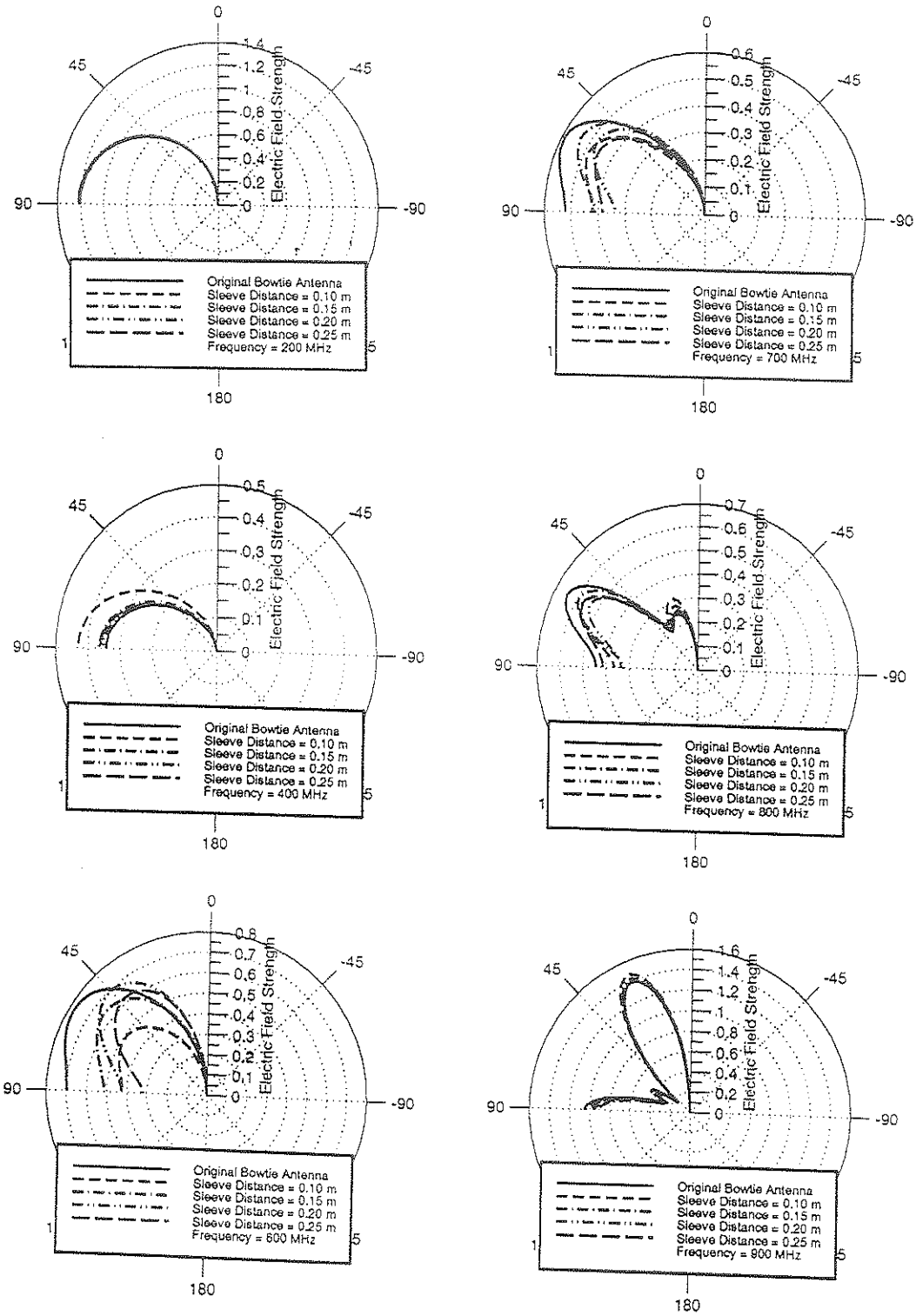

Figure 4.32 Far Electric Field (E_θ) Patterns of a Bowtie Antenna with Sleeve at Different Distances from the Antenna Axis as a Function of Zenith Angle θ and ϕ=90°.

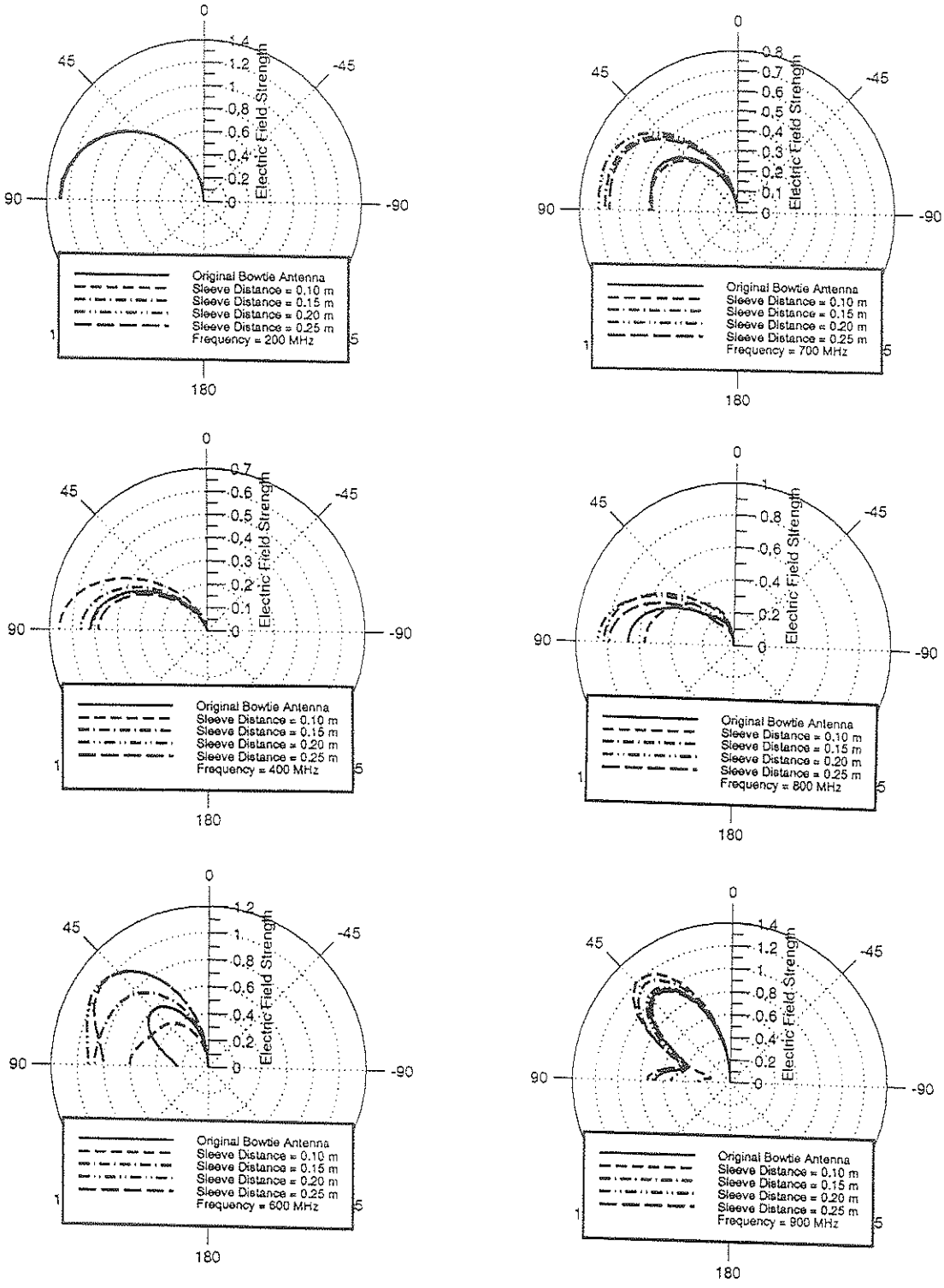

Figure 4.33 Far Electric Field (E_θ) Patterns of a Bowtie Antenna with Sleeve at Different Distances from the Antenna Axis as a Function of Zenith Angle θ and ϕ=0°.

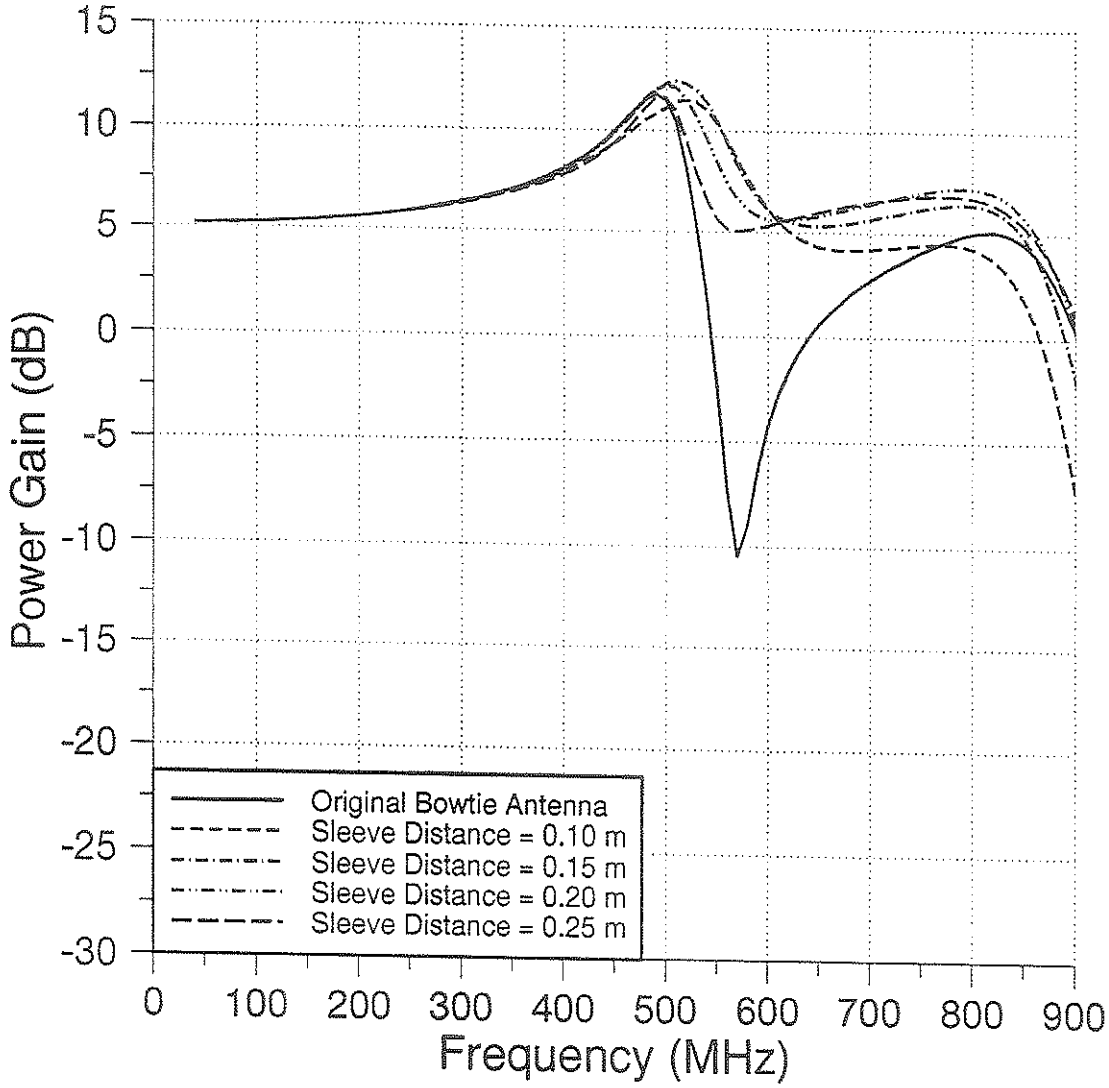

Figure 4.34 Power Gain Curves of a Bowtie Antenna with Sleeve at Different Distances from the Antenna Axis.

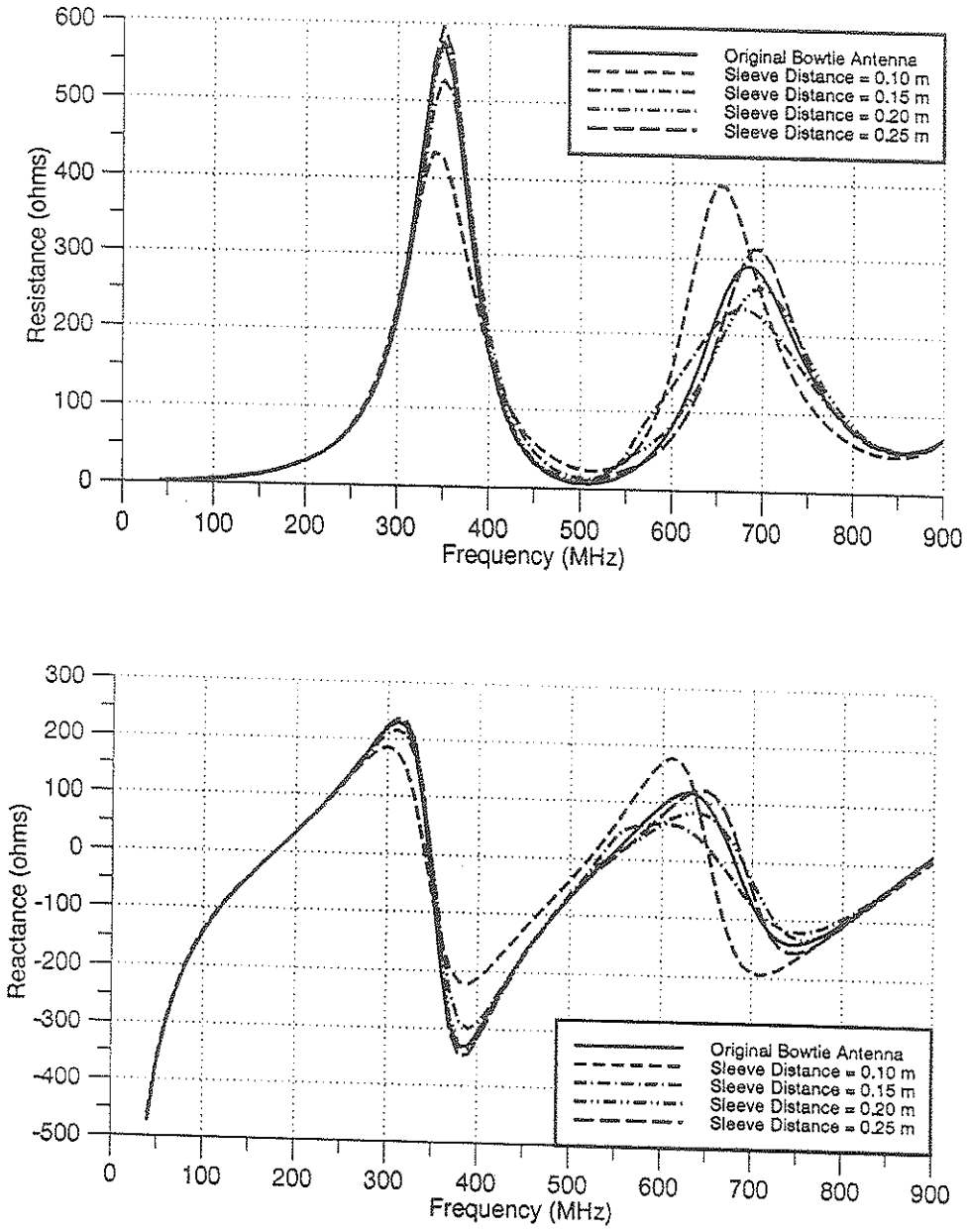

Figure 4.35 Input Impedance Curves of a Bowtie Antenna with Sleeve at Different Distances from the Antenna Axis.

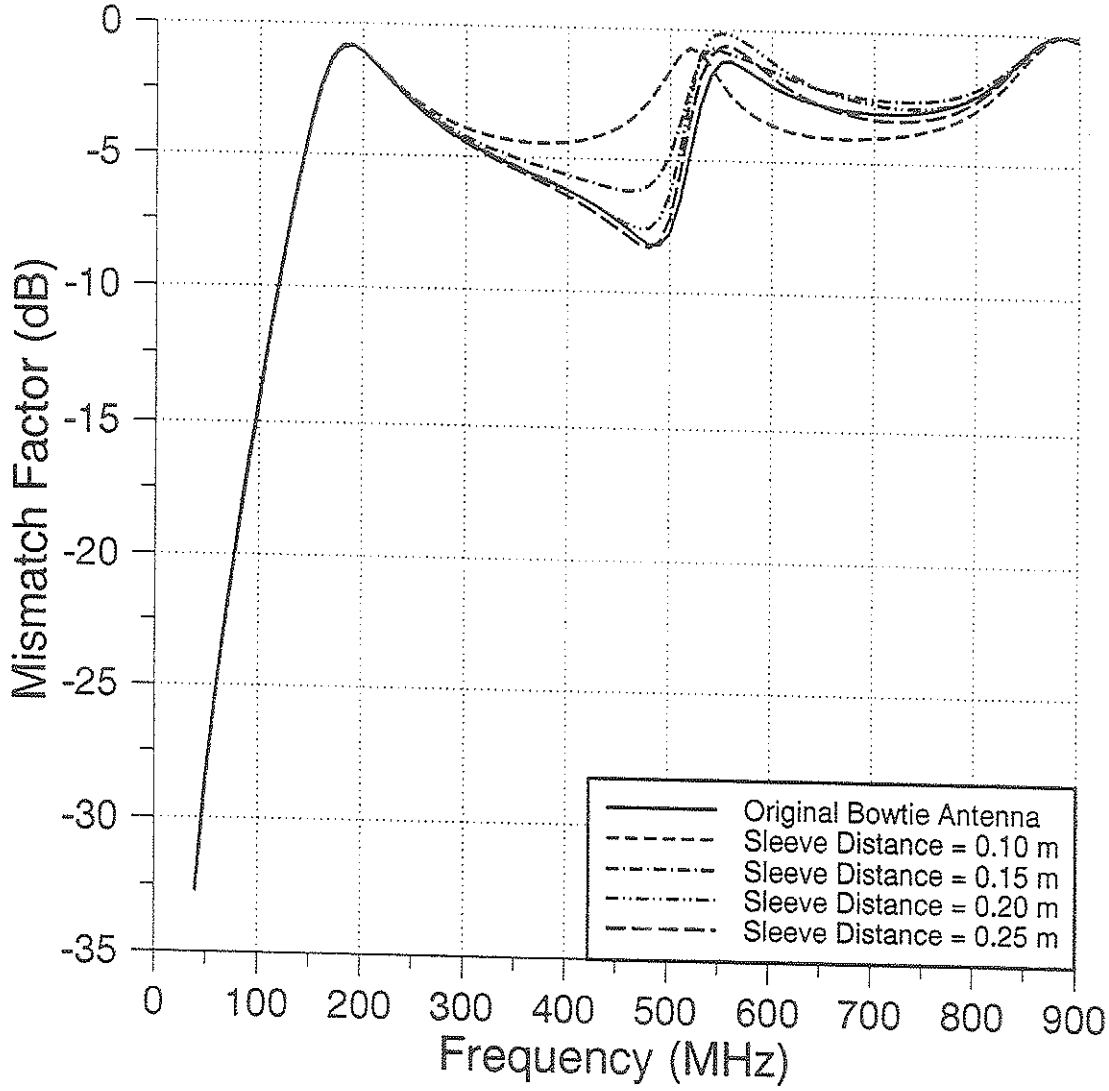

Figure 4.36 Mismatch Factor Curves of a Bowtie Antenna with Sleeve at Different Distances from the Antenna Axis.

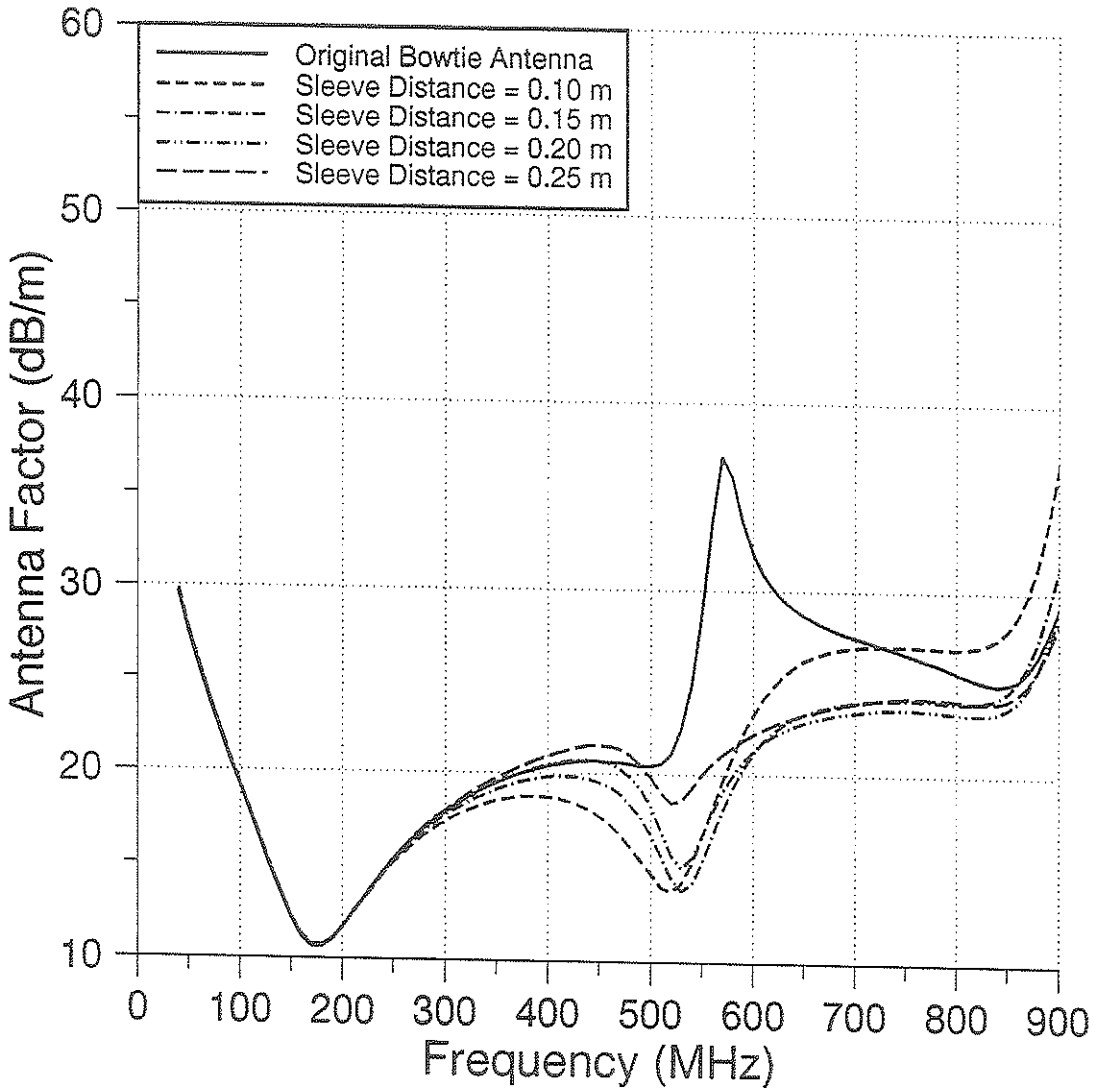

Figure 4.37 Antenna Factor Curves of a Bowtie Antenna with Sleeve at Different Distances from the Antenna Axis.

CHAPTER V

CONCLUSIONS

The performance and optimization of wire biconical antennas at low frequencies has been examined using the NEC2. The need for wire biconical antennas arises in cases where the solid or shell biconical antennas are too massive to be used in practical applications. In the NEC2, the current on a wire antenna is obtained through the EFIE and the use of the method of moments. By establishing an appropriate antenna model for the numerical analysis, the information that characterizes the frequency response of a wire biconical antenna can be accurately predicted. A comparison with the published results of other researches has made to demonstrate the validity of the antenna models used in the study. The performance of a simple wire biconical structure is examined for different hat and flare angles. The results indicated that while the electrical properties of the body-of-revolution wire biconical model approximate those of the shell or solid structure, the planar wire model's frequency characteristics are not as admirable. Hence, efforts have been made to optimize the performance of the planar wire biconical antennas.

In the NEC2, the current on a thin wire structure of small or

vanishing conductor volume is formulated in terms of the EFIE. The formulation is derived for the surface current $\mathbf{J}_s$ with the observation point $\mathbf{R}$ restricted to be off the surface S, so that $\mathbf{R}\neq\mathbf{R}'$. The EFIE is then solved numerically in the NEC2 by a form of the method of moments. The choice of basis and weighting functions are different with the weighting functions being chosen as a set of delta functions and the basis functions being represented by the sum of a constant, a sine term , and a cosine term. The current and the electric field on each segment is then calculated and the matrix equation is eventually solved by Gauss elimination method. With the knowledge of the unknown currents on a wire biconical antenna, the usual parameters, such as input impedance, gain, and radiation patterns can be obtained. Besides these parameters, the AF is also used to evaluate the performance of the antenna under examination. Mathematically, the AF of a receiving antenna is defined as a ratio between the incident field strength at the antenna, and the voltage at the input of the measuring receiver. Before using the NEC2 to study wire biconical antennas, a validation exercise is carried out to ensure the accuracy of the numerical results. It is shown that the computed input impedance and radiation patterns of both a planar wire biconical antenna with a=0.5 mm, θ_f=60°, and θ_h=180°, and a 3D wire biconical antenna with N=8, a=0.5 mm, θ_f=60°, and θ_h=180° are in good agreement with the measured values in [2].

The effect of hat and flare angle changes on the characteristics of wire biconical antennas have been investigated. This is achieved by computing and comparing the radiation patterns, input impedances, and antenna factors of wire biconical antennas with various flare and hat angles. Based on the extensive numerical data presented in Chapter III, it

is concluded that the antenna factor bandwidth of the planar biconical antenna decreases with an increase in flare angle and increases with an increase in hat angle. The usable frequency for the planar antenna is also found to be quite limited. For the 3D wire biconical models, a change in either the flare or hat angles has little effect in the antenna factor characteristics. The characteristics of a wire biconical antenna with corner reflector causes the input impedance of the wire biconical antenna to peak at about 400 MHz but otherwise is not adversive to the antenna factor's bandwidth performance.

Concepts focusing on the optimization of planar wire biconical antennas are introduced and tested in Chapter IV. It is shown that while significant bandwidth optimization can be obtained by adding wire fragments in the form of a cross to a planar wire biconical antenna, loading the added fragments with purely resistive loadings in the middle junction does not improve the bandwidth performance any further. Optimization is also achieved by offset feeding a planar wire antenna. When the source is elevated from the base of the antenna to about half the wire structure's length, the antenna factor bandwidth increases with an increase in source height. After the source reaches half the wire structure's length, however, the increase in source height would have an adverse effect on the antenna factor bandwidth. The use of parasitic elements, which are attached to the planar wire antenna for optimization purposes, has also been studied. Parasitic elements are very useful in cases where an impedance match is imperative at a certain frequency of operation. In the optimization of the antenna factor bandwidth, unfortunately, parasitic elements which are attached to the antenna structure, are shown to be ineffective. On the other

hand, parasitic elements which are detached and placed symmetrically on both sides of the planar antenna are shown to be of significant value to the optimization of the antenna factor bandwidth. The parasitic elements are referred to as sleeve, and the two antenna optimization parameters considered are the length of the sleeve and its distance from the antenna axis. It is found that the sleeve length and the antenna factor bandwidth is directly related for sleeve lengths of up to about half the wire model's length. The antenna factor bandwidth of the planar wire biconical antenna increases as the length of the sleeve is increased. However, if the length of the sleeve is increased beyond half the structure's length, then bandwidth decreases as the length is increased. The optimal distance between the parasitic elements and the antenna axis is found to be about half the length of the wire model. Moving the sleeve closer to or further away from the this distance would cause the antenna factor of the antenna to rise and hence decrease its antenna factor bandwidth.

Finally, despite the seemingly inferior characteristics of wire biconical antennas as compared to their shell or solid counterparts, in application where low-mass antenna is required, wire antennas are indispensable. Optimization of wire biconical antennas can be achieved in many ways. The methods used in this study can only be regarded as partial examples. Further investigation on the subject should be pursued to ensure the competitiveness of wire biconical antennas.

REFERENCES

[1] J.O. Prewiett, C.E. Smith, and C.M. Butler, "The Bow-Tie Antenna," 1974 IEEE Region III Proceeding of Southeastern, Orlando, Florida, pp. 59 - 62, April 29 - May 1, 1974.

[2] C.E. Smith , C.M. Butler, and K.R. Umashanka, "Characteristics of a Wire Biconical Antenna," Microwave J., pp. 37 - 40, Sept. 1979.

[3] G.H. Brown and O.M. Woodward, "Experimentally Determined Radiation Characteristics of Conical and Triangular Antenna," RCA Review, vol. 13, no. 4, pp. 425 - 453, Dec. 1952.

[4] B.A. Austin and A.P.C. Fourie, "Characteristics of the Wire Biconical Antenna Used for EMC Measurements," IEEE Trans. Electromagn. Compat., vol. 33, no. 3, pp. 179 - 187, August 1991.

[5] G.J. Burke and A.J. Poggio, "Numerical Electromagnetics Code - Method of Moments," NOSC Tech. Document 116, Lawrence Livermore Nat. Lab., Livermore, CA, 1981.

[6] A.J. Poggio and E.K. Miller, "Intergral Equation Solutions of Three-Dimensional Scattering Problems," Chapt. IV in Computer Techniques for Electromagnetics, edited by R. Mittra, Pergamon Press, New York, 1973.

[7] Chen-To Tai, *Dyadic Green's Functionns in Electromagnetic Theory*. Scranton: Intext Educational Publishers, 1971.

[8] Y.S. Yeh and K.K. Mei, "Theory of Conical Equiangular Spiral Antennas," Part I - Numerical Techniques, IEEE Trans. Ant. and Prop., AP-15, p. 634, 1967.

[9] TT.Wu and R.W.P King, "The Tapered Antenna and Its Application to the Junction Problem for Thin Wires," IEEE Trans. Ant. and Prop., AP-14, no. 1, pp. 42 - 45, January 1976.

[10] A.J. Poggio, "Integral Representation for Fields Due to Sources on Open Surface with Applications to End Caps," UCRL - 51723, Lawrence Livermore Laboratory, CA, Dec. 16, 1974.

[11] A.J. Poggio and R.W. Adams, "Approximations for Terms Related to the Kernel in Thin-Wire Integral Equations," UCRL - 51985, Lawrence Livermore Laboratory, CA, Dec. 19, 1975.

[12] F. Jay, Ed., *IEEE Standard Dictionary of Electrical and Electronics Terms*. New York: IEEE Press, p. 27, 1977.

[13] A.A. Smith, Jr., "Standard-Site Method for Determining Antenna Factors," IEEE Trans. Electromagn. Compat., vol. EMC-24, no. 3, pp. 316 - 322, August 1982.

[14] F.M. Green and M. Solour, "Development of Very-High-Frequency Field-Intensity Standards," J. Res. National Bureau Standards, vol. 44, pp. 527 - 547, May 1950.

[15] B.D. Popovic et al, *Analysis and Synthesis of Wire Antennas*. Hertfordshire: Research Studies Press Ltd., 1982.

[16] H.E. Taggart and J.L. Workman, "Calibration Principles and Procedures for Field Strength Meters (30 Hz to 1 GHz)," U.S. Dept. of Commerce, NBS Tech. Note 370.

[17] C.H. Papas and R.King, "Radiation From Wide-Angle Conical Antennas Fed by a Coaxial Line," Proc. IRE, vol. 39, p. 1269, November 1949.

[18] C.A. Balanis, *Antenna Theory: Analysis and Design*. New York: Harper & Row, 1982.

[19] W. Cheung and L. Shafai, "Performance of Biconical Antennas at Low Frequencies," ANTEM Conference Proceedings, pp. 233-238, August 1992.

[20] J.D. Kraus, *Antennas*. New York: McGraw-Hill Book Company, 1950.

[21] F.M. Landstorfer and R.R. Sacher, *Optimisation of Wire Antennas*. Hertfordshire: Research Studies Press Ltd., 1985.

Appendix A
General Properties of Dyadic Green's Function

A dyadic function, denoted by $\overline{\overline{D}}$, is formed by two vector functions. It is defined by

$$\overline{\overline{D}} = \mathbf{AB} \tag{A-1}$$

The vector function $\mathbf{A}$ is called the anterior element of $\overline{\overline{D}}$ and $\mathbf{B}$ the posterior element. A dyadic function by itself does not have any physical interpretation such as a vector function. However, when it acts upon another vector function the results may become more meaningful [7]. The anterior scalar product is defined by

$$\mathbf{C}\cdot\overline{\overline{D}} = (\mathbf{C}\cdot\mathbf{A})\mathbf{B} = \mathbf{B}(\mathbf{C}\cdot\mathbf{A}) = \mathbf{B}(\mathbf{A}\cdot\mathbf{C}) \tag{A-2}$$

and the posterior scalar product is defined by

$$\overline{\overline{D}}\cdot\mathbf{C} = \mathbf{A}(\mathbf{B}\cdot\mathbf{C}) = (\mathbf{B}\cdot\mathbf{C})\mathbf{A} = (\mathbf{C}\cdot\mathbf{B})\mathbf{A} \tag{A-3}$$

The vector product between a dyadic function and a vector function is also separated into interior vector product which is defined as

$$\overline{\overline{D}}\times\mathbf{C} = \mathbf{A}(\mathbf{B}\times\mathbf{C}) \tag{A-4}$$

and the posterior vector product which is defined as

$$\mathbf{C}\times\overline{\overline{D}} = (\mathbf{C}\times\mathbf{A})\mathbf{B} \tag{A-5}$$

If the vectors $\mathbf{A}$ and $\mathbf{B}$ in the above equations are decomposed into the component form in the rectangular coordinate system, (A-1) can be written in the form

$$\overline{\overline{D}} = \begin{pmatrix} A_xB_x\hat{x}\hat{x} + A_yB_y\hat{x}\hat{y} + A_xB_z\hat{x}\hat{z} \\ + A_yB_x\hat{y}\hat{x} + A_yB_y\hat{y}\hat{y} + A_yB_z\hat{y}\hat{z} \\ + A_zB_x\hat{z}\hat{x} + A_zB_y\hat{z}\hat{y} + A_zB_z\hat{z}\hat{z} \end{pmatrix} \qquad \text{(A-6)}$$

where all nine components of the dyadic function is distinct. One unique dyad, called the idem factor or unit dyad, is defined by

$$\overline{\overline{I}} = \hat{x}\hat{x} + \hat{y}\hat{y} + \hat{z}\hat{z} \qquad \text{(A-7)}$$

The characteristic feature of the idem factor can be demonstrated in the following identities:

$$\mathbf{A}\cdot\overline{\overline{I}} = \overline{\overline{I}}\cdot\mathbf{A} = \mathbf{A} \qquad \text{(A-8)}$$

$$\nabla\cdot(\overline{\overline{I}}\psi) = \nabla\psi \qquad \text{(A-9)}$$

where ψ represents a scalar function of position.

Appendix B
Vector Green's Theorem

Gauss' theorem states that for any vector function of position A with continuous first derivatives throughout a volume V and over the enclosing surface S [7],

$$\int_V \int \int \nabla \cdot \mathbf{A} \, dV = \int_S \int \mathbf{A} \cdot d\mathbf{S} \tag{B-1}$$

If we define

$$\mathbf{A} = \mathbf{Q} \times \nabla \times \mathbf{P} - \mathbf{P} \times \nabla \times \mathbf{Q} \tag{B-2}$$

and using the vector identity

$$\nabla \times (\mathbf{A} \times \mathbf{B}) = \mathbf{B} \cdot \nabla \times \mathbf{A} - \mathbf{A} \cdot \nabla \times \mathbf{B} \tag{B-3}$$

equation (B-2) can be written as

$$\nabla \cdot \mathbf{A} = \mathbf{P} \cdot \nabla \times \nabla \times \mathbf{Q} - \mathbf{Q} \cdot \nabla \times \nabla \times \mathbf{P} \tag{B-4}$$

Upon substitution of (B-4) into (B-1), we obtain

$$\int_V \int \int (\mathbf{P} \cdot \nabla \times \nabla \times \mathbf{Q} - \mathbf{Q} \cdot \nabla \times \nabla \times \mathbf{P}) \, dV = \int_S \int (\mathbf{Q} \times \nabla \times \mathbf{P} - \mathbf{P} \times \nabla \times \mathbf{Q}) \cdot d\mathbf{S} \tag{B-5}$$

which is known as the vector Green's identity.

Appendix C
Three-Dimensional Far Electric (E_θ) Field Patterns

For most practical applications, three-dimensional far field patterns are represented by a few two-dimensional plots as a function of θ for some particular values of ϕ, together with a few plots as a function of ϕ for some particular values of θ. While the two-dimensional plots give most of the useful and needed information, mentally visualizing the three-dimensional patterns from two-dimensional plots is not always easy. The following pages display, in a continuous three-dimensional format, far field patterns of wire biconical antennas with and without corner reflector as discussed in section 3.4. These figures are made to compliment the two-dimensional figures in the study and to provide additional information on the far field patterns.

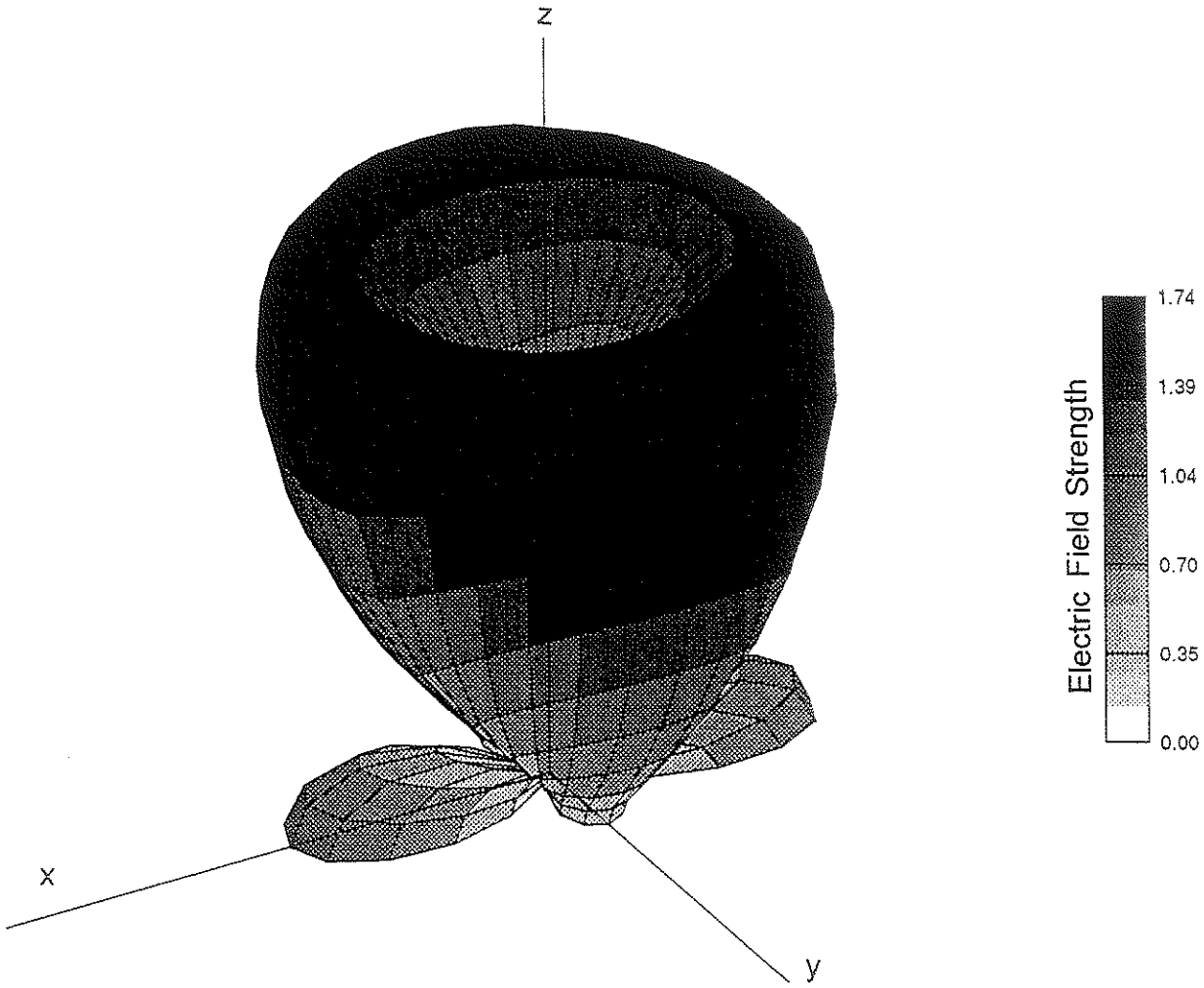

Figure C-1 Far Electric Field (E_θ) Pattern of a Planar Wire Biconical Antenna with θ_f=60° and θ_h=120°.

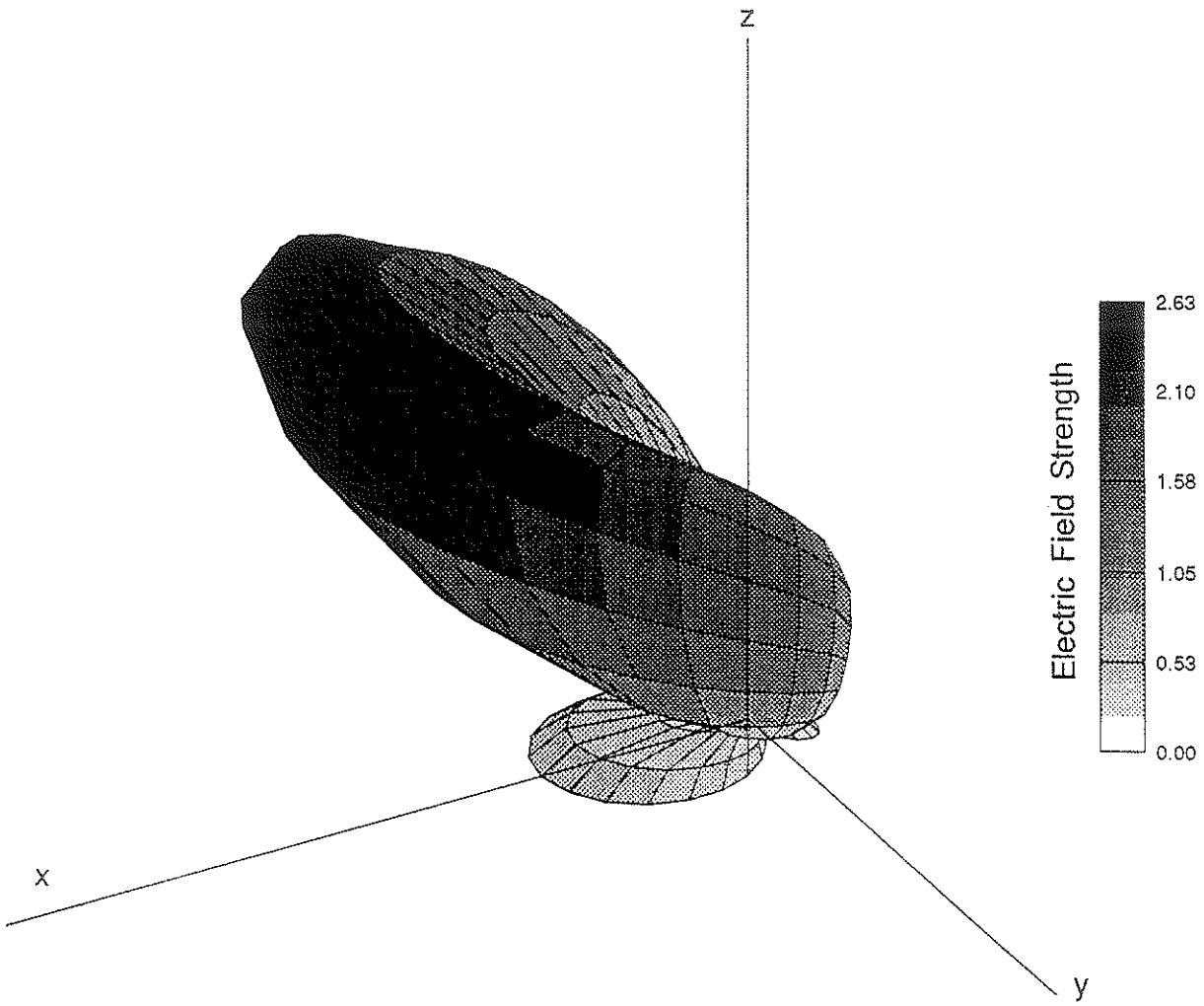

Figure C-2 Far Electric Field (E_θ) Pattern of a Planar Wire Biconical Antenna with θ_f=60°, θ_h=120°, and Corner Reflector.

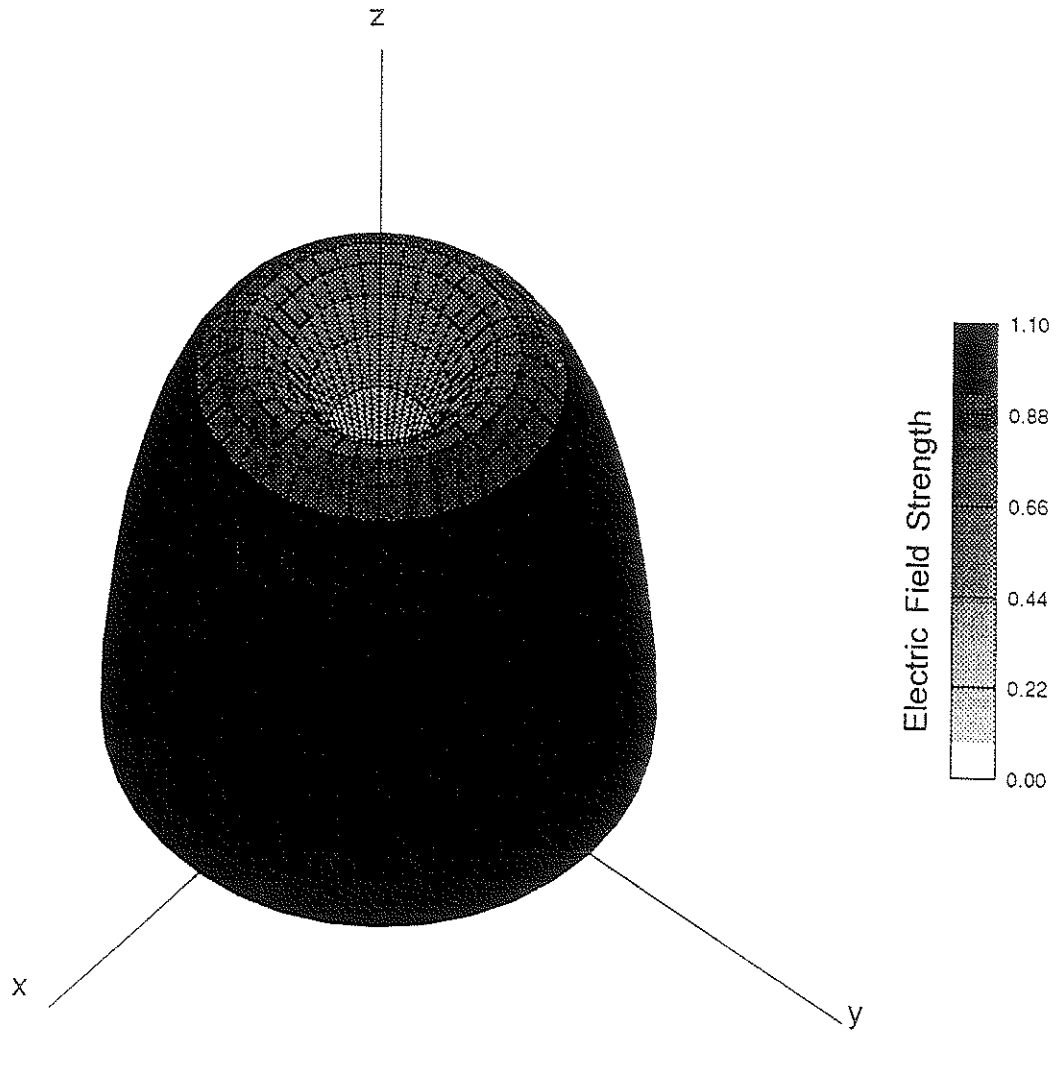

Figure C-3 Far Electric Field (E_θ) Pattern of a Body-of-Revolution Wire Biconical Antenna with θ_f=60° and θ_h=120°.

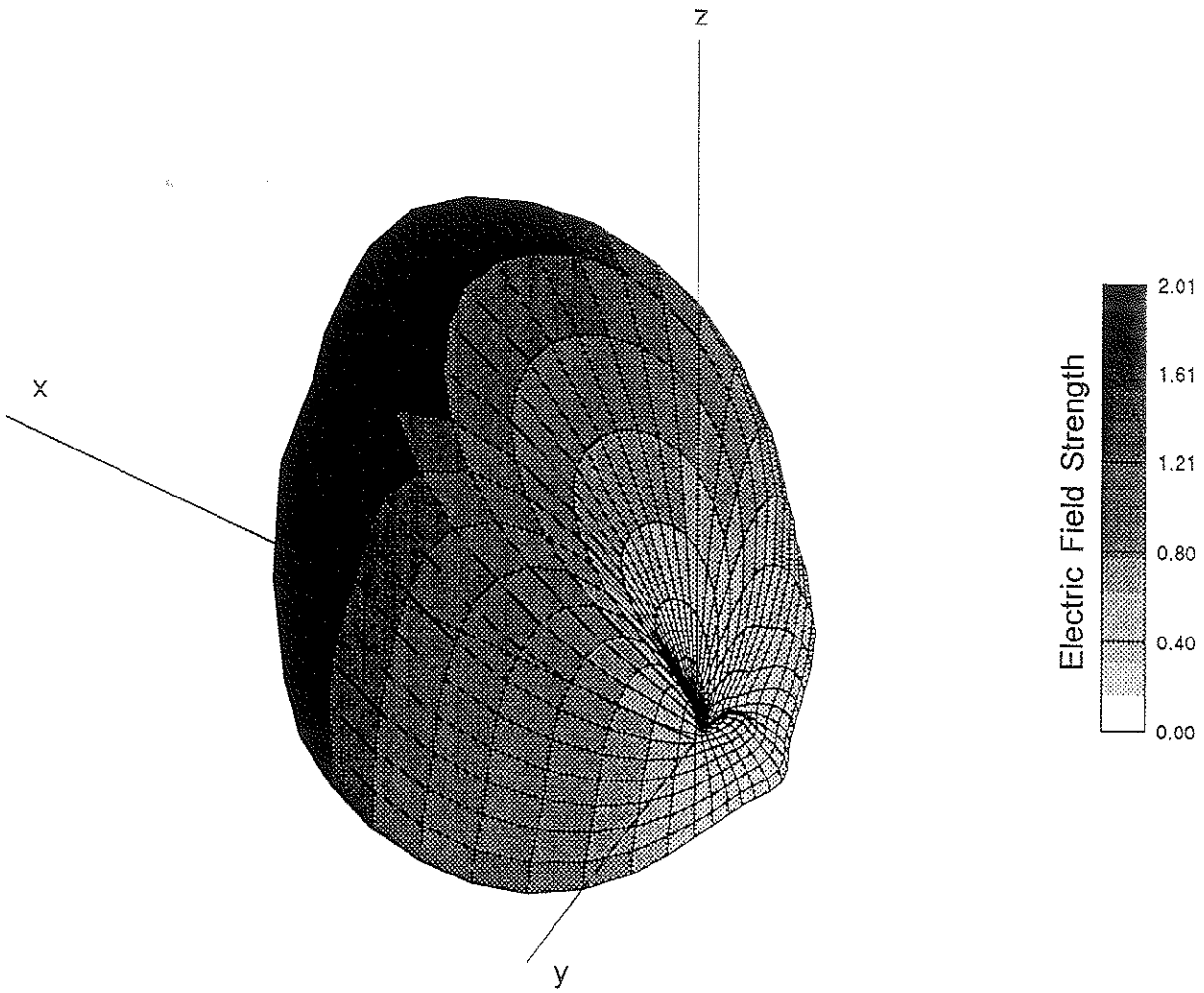

Figure C-4 Far Electric Field (E_θ) Pattern of a Body-of-Revolution Wire Biconical Antenna with θ_f=60°, θ_h=120°, and Corner Reflector.